IMPERIAL COLLEGE OF SCIENCE, TECHNOLOGY AND MEDICINE

UNIVERSITY OF LONDON

ROYAL SCHOOL OF MINES

DEPARTMENT OF EARTH SCIENCE
AND ENGINEERING

CENTRE FOR PETROLEUM STUDIES

ESTIMATING THE PERMEABILITY OF RESERVOIR SANDSTONES USING IMAGE ANALYSIS OF PORE STRUCTURE

by

Peter Lock

A thesis submitted in fulfilment of the requirements for
the degree of Doctor of Philosophy of the University of London
and the Diploma of Imperial College

November 2001

ABSTRACT

In this thesis, a method is developed for predicting the permeabilities of a core using only a small number of SEM images, without resorting to computationally intensive procedures. The pore structure is idealised as consisting of a cubic network of pore tubes having an arbitrary distribution of cross-sectional areas and shapes. The areas and perimeters of the individual pores are estimated from image analysis of scanning electron micrographs of thin sections, with appropriate stereological corrections introduced to infer the true cross sections of the pores.

Effective medium theory is used to find the effective single-tube conductance, based on the measured distribution of individual conductances, thereby allowing a prediction of the permeability. The methodology has been applied to several reservoir sandstones from the North Sea, and also an outcrop sample from Cumbria, UK, yielding predictions that fall within a factor of two of the laboratory measurements in most cases.

The procedure, although based on Kirkpatrick's intrinsically isotropic effective-medium approximation, is not only capable of yielding reasonably accurate estimates of the permeabilities, but also gives a qualitatively correct indication of the anisotropy ratio. It also found that the use of an Bernasconi's anisotropic effective-medium approximation does not lead to a systematic improvement in the results, perhaps because the samples used in this study were insufficiently anisotropic for the approaches to yield different results.

The validity of the effective medium approximation was also tested against exact pore network calculations. For the rocks examined in this study, with pore conductance distributions having log-variances less than 3, the effective medium approximation was found to be accurate to within a few percent.

CONTENTS

LIST OF FIGURES

LIST OF TABLES

ACKNOWLEDGEMENTS

I would like to sincerely express the deepest gratitude to my supervisors Dr. Robert W. Zimmerman and Dr. Xudong Jing for their guidance, knowledge, advice and support during the course of this work.

Special gratitude should be given to Adam Moss, Carlos Grattoni and Rodney Coleman of Imperial College, for their advice, support, and guidance, and also Dr. Ernie Hailwood of Core Magnetics for providing the St. Bees sample.

I would also like to thank Applied Reservoir Technologies for assisting with the image analysis section of this work, David Bowen of Heriot-Watt University for the core-permeability measurements, Graham Nash and John Dennis of Imperial College for their encouragement and technical assistance in core preparation, Mark Thomas and Elizabeth Morris for sample preparation, Richard Giddens, Graham Briers and Nick Royall for support in the acquisition of SEM data, and both Steven Bedley and Carl Jurczuk for their photographic and copying services.

Gratitudes go out to Enterprise Oil for their financial support, and very special thanks are given to Peter Whattler, Martin Kennedy and Jenny Garnham of Enterprise Oil, for valuable discussions.

The library staff at the Imperial College have been an invaluable source of assistance and also friendship over the past few years and a heartfelt thanks go out to Jason, Laura, Rachel and Sarah at the Earth Resources and Engineering Library.

Special thanks must go out to my peers, including, Said Al-Harthy, Rifaat Al-Mjeni, Azzan Al-Yaarubi, Widad Al-Wardy, David Benavente, Saifon Daungkaew, Jose Finol, Lamia Goual, Catherine Greenfield, Friederike Günzel, Florian Hollaender, Dustin Lister, Hing Man, John Matthews, Mohammed Piri, Carlos Romero, Sourith Sisavath and Canghu Yang, for their friendship and help over the past three years. Extra thanks to Sourith for making the initial simplifications to the NETSIM code.

Thanks are due to my friends outside of Imperial College, especially Hubert, Renata, John, Alicja, Kamilla (Kropnicka), Nick, Doug and Ritchie for their encouragement. Finally, I wish to express my gratitude to my wife Eulalia and all her family for their love and support over the past few years, and also Mum, Dad and Steve, without whose encouragement the completion of this thesis would not have been possible.

1 INTRODUCTION

Relating the transport properties of rocks to their pore structure has been a long-term goal of great interest to petroleum engineers, hydrologists and other earth scientists. This problem can be addressed at various levels of detail, with the resulting models requiring varying amounts of microstructural data. At one extreme, empirical permeability models such as Kozeny-Carman predict values of the permeability using knowledge only of porosity and a mean pore diameter or mean grain size. The Kozeny-Carman approach therefore requires some means of estimating the specific surface, which can be problematic (*Berryman and Blair,* 1986), and it is also known that this model, although fairly accurate for unconsolidated sands, tends to become unreliable for consolidated sandstones.

At the other extreme of complexity lie those models that attempt to reconstruct the pore space of a rock, and then numerically solve the Navier-Stokes equations in the pore space. *Adler et al.* (1990) reconstructed the pore space of Fontainebleau sandstones from thin sections and then solved the Navier-Stokes equations using a finite-difference scheme to yield the permeability. *Ferréol and Rothman* (1995) created a virtual microstructure using X-ray microtomography combined with a high-intensity image synchrotron radiation source, and then solved the flow equations using the lattice-Boltzmann method (*Rothman and Zaleski,* 1997). Such approaches are capable of reasonable accuracy, but at the expense of extensive data collection and computation.

Means of generating a virtual porous medium that do not require imaging techniques also exist. *Bentz and Martys* (1994) constructed the pore space of a simulated three-dimensional medium from two-dimensional slices selected at random, and solved the flow equations again using a finite-difference scheme to predict the permeability. Other examples of this type of approach include the simulation of artificial porous granular materials using sedimentation algorithms (*Pilotti,* 1998, *Øren and Bakke,* 2000), which can then be used as the input for a numerical solution of the Navier-Stokes equations. These approaches can provide insight into the relation between permeability and pore space, but do not directly address the question of predicting the permeability of a specific rock.

The goal of this project has been to develop a method for predicting directionally-dependent single-phase permeabilities of sedimentary rocks, using only a small number of SEM images, with a minimum of computational effort. The present scheme is a refinement of that developed by *Schlueter* (1995) for isotropic rocks, and applies image analysis to SEM photographs of sandstone pores. The hydraulic radius approximation is used to compute the individual conductivities of the pores. Stereological correction factors are applied to determine the true cross-sectional shapes from the images, and to determine the true number density of pores per unit area. A constriction factor accounts for the effect of the variation of the cross-sectional area along the tube length. The effective medium approximation of *Kirkpatrick* (1973), and its anisotropic extension by *Bernasconi* (1974) are used to determine an effective pore conductance from the measured distribution of conductances.

This procedure is applied to several consolidated North Sea sandstones, and also a St. Bees sample from Cumbria, UK, with permeabilities ranging over 10-1000 mD. As a test, exact network calculations are also performed using the network simulation code NETSIM (*Jing*, 1990). The permeabilities predicted using the inherently isotropic Kirkpatrick effective medium approximation are typically within a factor of two of the measured values, with an absolute average error of only 48%. Using the inherently anisotropic (but more computationally demanding) effective-medium approximation of Bernasconi fails to make a noticeable improvement to the predictions. The procedure outlined in this thesis seems to be the first method available that yields reasonably accurate estimates of permeability, with a minimum of computation.

2 LITERATURE REVIEW

2.1 Darcy's Law and the Permeability Concept

The theory of laminar flow through homogeneous porous media is based on an experiment performed by Darcy in 1856, who studied the vertical filtration of water and derived the relation

$$\frac{Q}{A} = q = K\frac{(h_2 - h_1)}{\zeta} \tag{2.1.1}$$

for vertical flow through a homogeneous filter bed of height ζ, bounded by horizontal planes of cross sectional area A, where Q is the total volume of fluid percolating through the medium in unit time, and $(h_2 - h_1)/\zeta$ represents the manometric gradient. The ratio Q/A is known as the filtration velocity, q, and arises when the entire measured cross-section is considered to be open to the flow.

This relationship, known as Darcy's law, is rather restricted in this form, its lack of utility being readily attributable to the amalgamation of several physical parameters into a single constant of proportionality. *Hubbert* (1956) gave a deeper interpretation of the physical significance of K, showing that it contained the fluid density ρ and viscosity η. It follows then that one would like to separate the influence of the porous medium from that of the fluid. *Nutting* (1930) suggested using $K' = k/\eta$, with k denoting the specific permeability of the medium and η denoting the viscosity. The dimensions of specific permeability are L^2, that is, the same as surface area. The specific permeability is defined only on a macroscopic scale and relates to the porous medium, irrespective of the fluid characteristics. A commonly used unit for the specific permeability is the Darcy, defined by

$$1 \text{ Darcy} = 9.87 \times 10^{-13} \text{ m}^2. \tag{2.1.2}$$

Darcy's law can also be expressed in terms of the pressure and the gravitational potential, as follows. We start with the static or piezometric head,

$$h = \frac{p}{\rho g} + z, \tag{2.1.3}$$

where z refers to the vertical direction, considered positive upwards. Taking the derivative of h along the flow direction gives

$$\frac{dh}{d\zeta} = \frac{d}{d\zeta}\left(\frac{p+\rho gz}{\rho g}\right) = \frac{1}{\rho g}\frac{d}{d\zeta}(p+\rho gz) = \frac{1}{\rho g}\left\{\frac{dp}{d\zeta} + \rho g\frac{dz}{d\zeta}\right\}, \qquad (2.1.4)$$

where we assume that ρ is constant and independent of pressure. For horizontal flow $dz/d\zeta$ is zero, and so

$$\frac{dh}{d\zeta} = \frac{1}{\rho g}\frac{dp}{d\zeta}, \qquad (2.1.5)$$

which shows that K in equation (2.1.1) is given by

$$K = \frac{k\rho g}{\eta}. \qquad (2.1.6)$$

The parameter K is therefore a composite parameter containing terms that account for the properties of the fluid and of the porous medium, and has dimensions LT^{-1}, where L and T are length and time, respectively. We may rewrite (2.1.1) in three-dimensional form as follows

$$\mathbf{q} = -\mathbf{K}\nabla h = -\frac{\mathbf{k}}{\eta}[\nabla p + \rho g\nabla z]. \qquad (2.1.7)$$

where $\mathbf{k}$ is the permeability tensor, which is possibly anisotropic (see section 2.3). The minus sign indicates that fluid flows towards the region of lower potential. In the remainder of this dicussion we will neglect the $\rho g\nabla z$ term, for simplicity of notation only, in which case (2.1.7) may be written as

$$q = -\frac{k}{\eta}\nabla p. \qquad (2.1.8)$$

The concept of permeability has within it the influences of the properties of the porous medium. Many attempts at establishing empirical relationships between porosity and rock permeability have been documented (*Scheidegger*, 1963). Generally speaking, however, no simple correlation between porosity and permeability exists; a correlation that might be sought is between *pore structure* and permeability. One may consider pore structure to imply a pore size distribution (PSD), and ideally then obtain PSD-ϕ correlations directly from capillary pressure curves derived from mercury intrusion methods and so forth.

A commonly accepted hypothesis that connects the microscopic pore velocity and the filter velocity is the *Dupuit–Forchheimer* assumption, which considers the flow through

a porous medium to take place along channels with a local (pore) velocity denoted v_p, leading to the relationship

$$v_p = \frac{q}{\phi}, \tag{2.1.9}$$

where q is the volumetric flow rate per unit area. The *Dupuit–Forchheimer* assumption thus states that the pore velocity will be larger than the filter velocity, owing to the reduced space available for the fluid to flow in comparison with the bulk volume of the porous medium (with regard to which the filter velocity is calculated). It should be noted that the actual pore velocity of the fluid will fluctuate widely from channel to channel, and so equation (2.1.9) actually defines an average pore velocity.

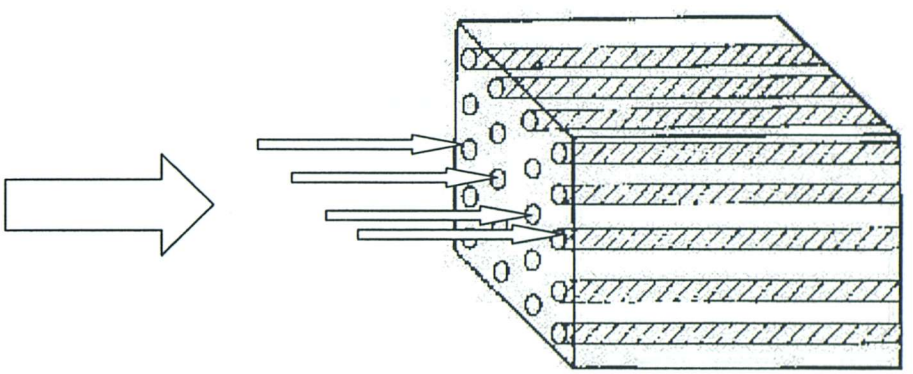

Figure 2.1.1 Illustration of the Dupuit-Forchheimer assumption. The total cross sectional area of the conduits open to the flow in the incoming direction is less than the total area of the side of the cube (adapted from *Scheidegger,* 1963).

Darcy's law is known to be valid at low flow rates (creeping flows). Nevertheless, non-Darcian flow effects may well become significant in porous media at sufficently high filtration velocities, usually characterised by Reynolds numbers greater than one. The Reynolds number (*Re*) is a ratio of inertial to viscous forces. For slightly higher values of *Re*, it may be possible to express Darcy's law as a perturbation expansion in q to account for the nonlinearity in the relationship between the applied pressure gradient and the filter velocity vector. The most familiar form of such an expansion is known as Forchheimer's equation (*Scheidegger,* 1963):

$$-\frac{dp}{d\zeta} = \frac{\eta q}{k} + \beta \rho q^2, \tag{2.1.10}$$

where β is the so-called "non-Darcy" flow coefficient. Regardless of whether the flow is in the Darcy or Forchheimer regime, the permeability coefficent, k, is an important parameter.

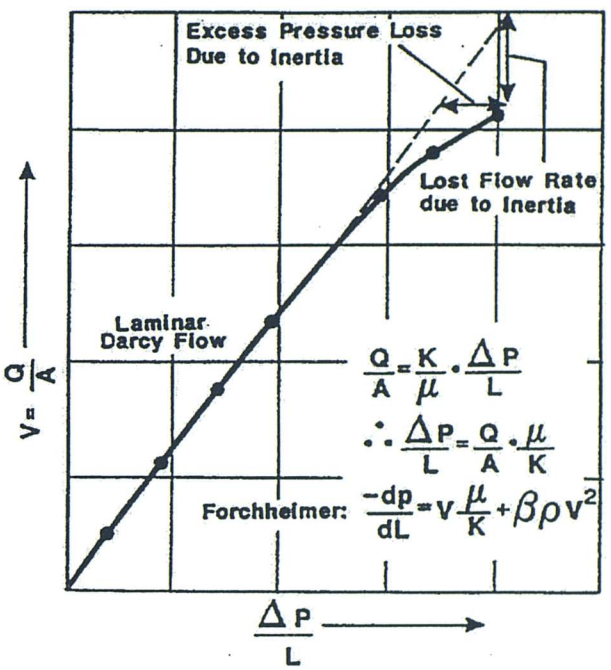

Figure 2.1.2 Darcy velocity versus pressure drop per unit length illustrating Darcy (linear, laminar) flow region and the Forchheimer (non-linear, laminar) flow region (after *Boyle et al.*, 2000).

The fundamental equation governing fluid motion on the pore-scale is that of Navier-Stokes. For incompressible, Newtonian fluids these equations take the form (*de Marsily,* 1986)

$$\frac{\partial p}{\partial x_i} - \frac{\eta}{3}\frac{\partial}{\partial x_i}(\nabla \cdot \mathbf{v}) - \eta \nabla^2 u^i = \rho\left(F_i - \frac{Dv^i}{Dt}\right), \tag{2.1.11}$$

where η is the coefficient of dynamic viscosity, F_i are the components of the body force vector per unit mass, and Dv^i/Dt is the material derivative. There are three Navier-Stokes equations, one for each direction in space. The boundary condition used is that $\mathbf{v} = 0$ at the pore walls. The Navier-Stokes equations must be supplemented by an equation that expresses the principle of conservation of mass:

$$\nabla \cdot (\rho \mathbf{v}) + \frac{\partial \rho}{\partial t} = 0\,. \tag{2.1.12}$$

If the flow is steady, then the time rate of change of density is zero, and the continuity equation takes the form

$$\nabla \cdot (\rho \mathbf{v}) = 0. \tag{2.1.13}$$

Furthermore, if the fluid is incompressible, then the density ρ is constant, and so equation (2.1.12) reduces to

$$\nabla \cdot \mathbf{v} = 0. \tag{2.1.14}$$

2.2 Tube-Bundle Models and the Kozeny-Carman Relation

2.2.1 Introduction

The Navier Stokes equations may be solved exactly for a straight circular tube. The resulting equation expresses the flow rate Q through a tube of radius r, length ζ and pressure drop Δp defined to be *negative* across the length of the tube. The result is known as the Hagen-Poiseuille equation, and leads to the simplest permeability model that incorporates some description of the structure of a porous medium (*Bear,* 1972):

$$Q = \frac{\Delta p \pi r^4}{8\eta\zeta}. \tag{2.2.1.1}$$

If we have n such pores within a region of cross-sectional area A, then

$$\phi = \frac{n\pi r^2}{A}. \tag{2.2.1.2}$$

where ϕ is the porosity. The total flow through the bed, $Q_{TOTAL} = nQ$, is given by

$$Q_{TOTAL} = A\frac{\phi r^2}{8\eta}\frac{\Delta p}{\zeta}. \tag{2.2.1.3}$$

Setting equations (2.1.8) and (2.2.1.3) equal to each other establishes a relationship between the permeability and the number and size of tubes in the medium:

$$k = \frac{\phi r^2}{8}. \tag{2.2.1.4}$$

Equation (2.2.1.4) is usually modified by the inclusion of a tortuosity coefficient τ, which is sometimes interpreted as introducing an average pathlength parameter into the transport model. In the context of a three-dimensional parallel tube model, only one third of the pore tubes are aligned in any given direction, in which case we must decrease the permeability given by equation (2.2.1.4) by a factor of $\tau = 3$:

$$k = \frac{\phi r^2}{8\tau} = \frac{\phi r^2}{24} = \frac{\phi}{96} d^2, \tag{2.2.1.5}$$

where the result is finally expressed in terms of pore diameter, *d*.

Equations that have included a specific surface area term are known as Kozeny-type equations. In the Kozeny-Carman theory (*Dullien,* 1992), the porous medium is taken as a closed channel of highly irregular shape, but on average having a constant cross sectional area. The inclusion of geometrical properties into an empirical model then provide an extension of tube-like models (*Purcell,* 1949; *Scheidegger,* 1963) towards more elaborate descriptions of the influence of the pore shape *and* orientation on permeability (*Sullivan,* 1942; *Haring and Greenkorn,* 1970).

The Kozeny-Carman generalisation of the tube model assumes that resistance to flow arises from viscous drag along the pore walls, and so permeability should show an inverse correlation with the amount of surface area per unit volume. If we define specific surface as the internal surface area per unit bulk volume,

$$S = \frac{A_{PORE}}{V_{BULK}}, \tag{2.2.1.6}$$

and write porosity as

$$\phi = \frac{V_{PORE}}{V_{BULK}} = \frac{n\pi r^2 L}{V_{BULK}}, \tag{2.2.1.7}$$

then

$$S = \frac{2n\pi rL\phi}{n\pi r^2 L} = \frac{2\phi}{r}. \tag{2.2.1.8}$$

Inserting this expression into (2.2.1.5) provides a Kozeny-Carman equation in the form

$$k = \frac{\phi^3}{2\tau S^2}. \tag{2.2.1.9}$$

2.2.2 The Hydraulic Radius Approximation

The basic form of Kozeny's equation, despite having been modified on numerous occasions, remains dependent on the correlation of the permeability with the square of some characteristic length scale, and thus attempts to correlate permeability with some characteristic pore size. This is already implicit in the definition of specific surface, where the representative pore structure parameter arises in the form of the hydraulic radius approximation and may be defined for a group of irregularly shaped but cylindrical type pores as

$$r_h = 2\frac{A_p}{\Gamma_p}. \tag{2.2.2.1}$$

where A_p is the pore area and Γ_p is the pore perimeter. The factor of 2 renders the expression exact for a circle, since

$$r_h = 2\frac{\pi r^2}{2\pi r} = r. \tag{2.2.2.2}$$

(It should be noted that many authors omit the factor of 2 in their definition of the hydraulic radius). Using these definitions however, we can rewrite the specific surface in terms of the internal surface area per unit of pore volume, and so in terms of the *hydraulic radius*, as

$$S = \frac{2\phi}{r_h}. \tag{2.2.2.3}$$

We have thus established a connection between the hydraulic radius for a single representative pore and the Kozeny-Carman relation. Equation (2.2.1.9) may be then written in the more general form

$$k = \frac{r_h^2}{cf(\phi)}, \tag{2.2.2.4}$$

where 'c' represents a combined shape-tortuosity factor, known as Kozeny's constant, (*Wyllie and Spangler,* 1952). In this equation, however, a porosity function $f(\phi)$ is introduced to further reflect the effect of pore shape (*Rumpf and Gupte*, 1971).

If the pores have a well-defined shape, then the relationship between r_h and the mean pore radius, r_p is quite straightforward. This is the case for a group of nonintersecting, cylindrical capillaries For a parallel-sided slit-shaped pore, r_h is given as half the slit

width. A list of comparative values that test the utility of the hydraulic radius approximation for different cross sections has been gathered by *Carman* (1941).

Schlueter (1995) reformulated permeability in terms of the hydraulic radius as

$$k = \frac{r^2}{8} = \frac{1}{8}\left(\frac{2A}{\Gamma}\right)^2 = \frac{1}{2}\left(\frac{A}{\Gamma}\right)^2 = \frac{1}{2}r_h^2, \qquad (2.2.2.5)$$

(where the factor of 2 in equation (2.2.1) has been omitted) and the equivalence of the calculated permeabilities was tested for various pore shapes using known analytic solutions (Table 2.2.1).

Table 2.2.1 Accuracy of the hydraulic radius approximation (after *Schlueter,* 1995).

Cross section		k^{EXACT}	k^{HR}	Error (%)
Circle, radius a		$a^2/8$	$a^2/8$	0
Equilateral Triangle, side a		$a^2/80$	$a^2/96$	-20
Square, side a		$a^2/28$	$a^2/32$	-11
Slit, thickness h		$h^2/12$	$h^2/8$	50
Ellipse	a:b = 2:1	$a^2/68$	$a^2/88$	14
	a:b = 10:1	$a^2/403$	$a^2/324$	21

Rewriting equation (2.2.1.1) in terms of the pressure gradient, we obtain, for *one pore,*

$$Q = -\frac{\pi r^4}{8\eta}\nabla p. \qquad (2.2.2.6)$$

Thus, we can write a generalised Hagen-Poiseuille equation in terms of (2.2.2.2) as

$$Q = -\frac{Ar_h^2}{8\eta}\nabla p = -\frac{A^3}{2\Gamma^2\eta}\nabla p. \qquad (2.2.2.7)$$

We then define hydraulic conductance as

$$C_h = \frac{A^3}{2\Gamma^2}, \qquad (2.2.2.8)$$

and (2.2.2.6) may be written as

$$Q = -\frac{C_h}{\eta}\nabla p. \qquad (2.2.2.9)$$

Sisavath et al. (2000) tested the hydraulic radius approximation against the boundary element method for sets of pores from SEM images of Berea and Massilon sandstone. The overall error introduced by the hydraulic radius approximation was found to be in the range of 1-15%, indicating that, to some extent, the errors cancel out.

2.2.3 Electrical Parameters in the Tube-Bundle Models

Walsh and Brace (1984) emphasized the similarities between the flow of an electrical current and the flow of a fluid, since in both cases the flow characteristics are controlled by the pore geometry. In the former case, this is a direct consequence of the fact that most minerals are insulating, and so the conductivity will then arise from the current flowing through the natural electrolytes present in the connected void space. The influence of the pore geometry on the electrical resistance may be considered to be composed of two separate quantities, the cross–section available for conduction, and the topology of the pore space (*Dullien,* 1992). The ratio of the electrical conductance of an electrolyte, σ_{el}, to the conductance of a rock saturated with the same fluid σ_{ro}, is known as the Electrical Formation Factor,

$$F = \frac{\sigma_{el}}{\sigma_{ro}} > 1. \qquad (2.2.3.1)$$

Ohm's law may be considered to be the electrical equivalent of Darcy's law, with electrical conduction along a straight wire analogous to the Hagen–Poiseuelle equation through a uniform cylinder of constant cross–sectional area. Ohm's law states that for a cylindrical pore,

$$j^e = g^e(r)\Delta V \qquad (2.2.3.2)$$

where j^e is the current, ΔV is the potential difference across the length of the pore ζ, and g^e is the electrical conductivity. If we then consider the conductance of the saturating solution σ_{el}, we may write $g^e(r)$ as

$$g^e(r) = \frac{\pi r^2 \sigma_{el}}{\zeta}. \qquad (2.2.3.3)$$

Analogously, we can consider the water discharge j^h:

$$j^h = g^h(r)\Delta p\,, \tag{2.2.3.4}$$

and also a hydraulic conductivity g^h of a single pore relating to a pressure drop Δp which we obtain from (2.2.2.3) as

$$g^h(r) = \frac{\pi r^4}{8\eta\zeta} \equiv \frac{C_h}{\eta\zeta}. \tag{2.2.3.5}$$

2.2.4 The Model of Walsh and Brace

Walsh and Brace (1984) derived a relationship between electrical formation factor and porosity, with the inclusion of a tortuosity factor on the basis that the pathlength would similarly control both the flow of current and the flow of fluid. If we take equation (2.2.3.2) as representing the current through each tube, then we can write for N identical tubes of constant cross-sectional area:

$$j^e_{TOTAL} = -ng^e(r)\Delta V\,. \tag{2.2.4.1}$$

We then insert expression (2.2.1.2) for the porosity into this equation, to obtain

$$j^e_{TOTAL} = -\phi A\sigma_{el}\nabla V\,. \tag{2.2.4.2}$$

Therefore, the conductivity of the rock/fluid system becomes, from equations (2.2.3.1) and (2.2.4.2),

$$\sigma_{ro} = \phi\sigma_{el}\,, \tag{2.2.4.3}$$

and thus the parallel tube model predicts

$$F = \frac{\sigma_{el}}{\phi\sigma_{el}} = \frac{1}{\phi}. \tag{2.2.4.4}$$

If we now consider that the conductivity, g^e will be affected by the path length for the current, we modify (2.2.4.4) as follows:

$$F = \frac{\tau}{\phi}. \tag{2.2.4.5}$$

We can extend the electrical analogy to modelling fluid transport in non-circular channels by weighting F by some predetermined shape factor, b, that will assume different values for different conduit geometries. This factor takes on the values of b = 0.5 for a circle and 0.562, 0.597, 0.667 for a square, an equilateral triangle, and a strip, respectively (*Bear*, 1972). *Walsh and Brace* (1984) adopted the shape factor, and furthermore related k to the formation factor F and also the specific surface area term, S, by combining (2.2.1.9) with b = 0.5 and (2.2.4.5) to yield

$$k = \frac{1}{2}\frac{\phi^2}{FS^2}. \tag{2.2.4.6}$$

If we now recall our definition of hydraulic radius (equation 2.2.2.3), we can write

$$r_h = 2\frac{\phi V_{BULK}}{A_{PORE}} = 2\frac{\phi}{S}, \tag{2.2.4.7}$$

in which case (2.2.4.6) becomes

$$k = \frac{b^3 r_h^2}{F}. \tag{2.2.4.8}$$

Thus, we have eliminated tortuosity to arrive at an expression for the mean hydraulic radius in terms of the electrical formation factor as

$$r_h = \sqrt{\frac{kF}{b^3}}. \tag{2.2.4.9}$$

2.2.5 The Model of Katz and Thompson

Further models, based on the electrical conductivity of saturated rock, attempt to define a more general representative length scale than the hydraulic radius. *Katz and Thompson* (1986) proposed the relationship

$$k = \frac{Al^2}{F}, \tag{2.2.5.1}$$

where the term l refers to the characteristic length scale used to quantify the pore space and the parameter A is again some form of implicit shape-tortuosity factor. The characteristic length is obtained from mercury injection experiments. This information comes from the location of the inflection point in the mercury intrusion curve as this

feature signals the onset of the formation of a spanning network of connected pores. Hence, fluid transport through porous media becomes a percolation problem to which we must then assign a threshold conductance. This threshold parameter then defines l, and as such simultaneously defines a threshold in both the hydraulic and electrical conductivity problems. The characteristic length in this case is then a critical radius r_c, derived from the Washburn equation, and so we define a lower bound l for the connected cluster as (*Sahimi*, 1995):

$$l = r_c = \frac{-4\gamma\cos\theta}{P_i}, \tag{2.2.5.2}$$

where P_i is the pressure at the inflexion point, γ is the surface tension between mercury and the vacuum, and θ is the angle of contact between the mercury and the pore surface. From this percolation treatment emerges an analysis of the behaviour of conducting systems carrying a very broad distribution of conductances, from which we find

$$k = \frac{Ar_c^2}{F}. \tag{2.2.5.3}$$

Equation (2.2.5.3), then resembles (2.2.2.4), and if rewritten in terms of r_c becomes analogous to (2.2.4.9):

$$r_c = \sqrt{\frac{kF}{A}}. \tag{2.2.5.4}$$

Similarly, *Dullien* (1992) correlated permeability with breakthrough pressure and porosity. The physical basis of Dullien's model is that the permeability of a tube with step changes in diameter, having a given length and volume, can be matched by the permeability of a bundle of n uniform tubes of diameter D_x of the same length and same total volume. For sandstone samples, Dullien found that $D_x=D_b/3.5$, where D_b is the "breakthrough diameter". The calculated value, k_c is provided as a plot against the experimental value k_{exp}, in Figure 2.2.1. Other correlations of a similar nature have been made. *Macmullin and Muccini* (1956) presented a correlation among the breakthrough pressure, formation factor and permeability, with a probable error in a single observation of about 18%. *Chatzis* (1980) tested this correlation for a variety of sandstones and found a $\pm$ 60% scatter.

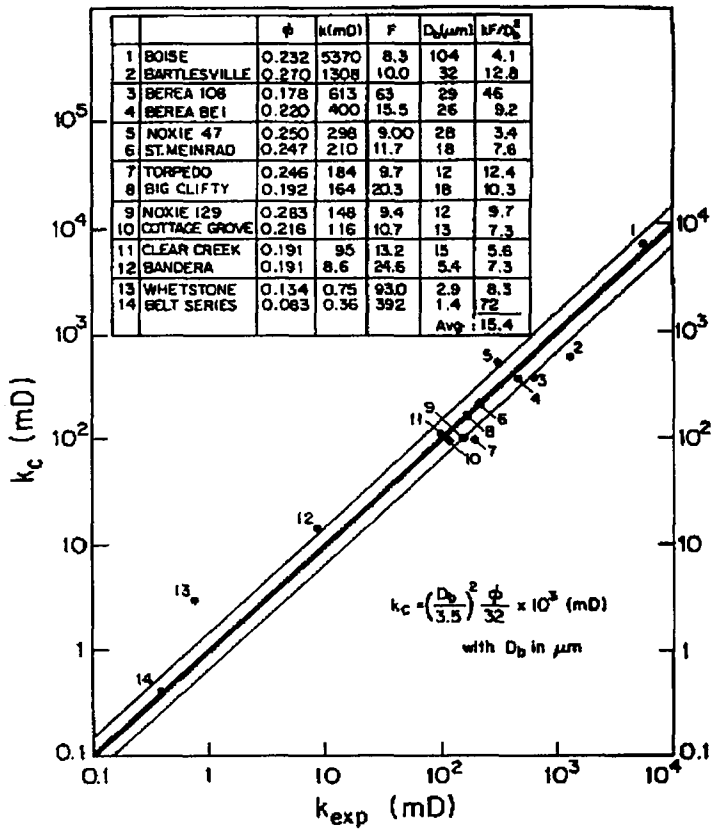

Figure 2.2.1 Empirical permeability correlation for sandstones (after *Dullien,* 1992).

The interpretation of a pore-size distribution curve ultimately depends on the validity of the geometrical and other assumptions involved. For example, the entry diameter, D_e is to be regarded as the size of a uniform cylindrical pore which would fill at a given pressure, rather than the true pore dimension. Consequently, this method fails to account for capillary hysteresis, and thus the drainage curve on the pre-emptying cycle of the intrusion experiment. A value for $\gamma \cos\theta$ must also be assumed, and as we are dealing with a relatively non-wetting fluid, we ignore Schultze's assumption of zero contact angle (*Dullien*, 1992), and take $\theta = 141^\circ$ for mercury intrusion experiments. Most importantly, the presumption that the pores are invaded in decreasing order of size may be invalidated by network effects (*Dullien and Dhawan,* 1975), implying that the sequential mode of pore filling is dictated primarily by their interconnectedness (that is, their co-ordination number). In spite of this, many pore-size distribution measurements are actually based on the premise that they model bundles of capillaries, or parallel tube

models, with a complete neglect for the interconnections that, in reality, constitute a network.

Theoretical analyses of mercury intrusion curves have been reviewed by *Dullien* (1992) and much of this work is attributable to *Meyer* (1953) and *Mayer and Stowe* (1965, 1966), who made several attempts to account for the capillary filling and drainage curves using computational methods which relied on a probabilistic approach. However, they failed to determine the sizes of the larger pores entered via smaller pore throats. In addition, the problem of capillary hysteresis was tackled directly by *Kruyer* (1958), in his analysis of the retraction of mercury from a bed of glass spheres.

The implementation of pore-size distribution data, acquired from "real" porous beds can be achieved by taking a volume-based pore size density $v_p(D)$. Assuming a tortuosity factor of 1/3, (2.2.1.9) becomes

$$k = \frac{\phi}{96} \frac{\int_0^\infty D^2 v_P(D) dD}{\int_0^\infty v_P(D) dD}. \qquad (2.2.5.5)$$

The expression above thus reflects an extension of the parallel tube models to the realm of "realistic" permeability modeling. However, the inherent drawback remains that the conduits are all assumed to connect the boundary faces of the matrix, perpendicular to the flow. In contrast to this, we may assume that the pore space is serially aligned, and in doing so consider a serial type model of fluid transport whereby a single conduit is assumed to be comprised of segments of different diameter. It is therefore reasonable to assume a transport model that lies somewhere between these two extremes, and consider a pore space consisting of multiple conduits with some intermediate tortuosity value to arrive at a model representing bundles of periodically constricted tubes (*Dullien,* 1992).

2.2.6 The Model of Johnson and Sen

A further model based on the electrical conductivity of saturated rock was that of *Johnson and Sen* (1988), where the characteristic length scale and electrical formation factor was related to a *dynamic* permeability. The electrical conductivity through a porous medium can be attributed to a "bulk" interstitial flux and also the ionic transport that occurs through the electrical double layer system that rests between the pore wall

and fluid interface. Consequently, we may exclude pores below a certain radius, namely when the radius approaches the double-layer thickness. The analogy between electrical conductivity and fluid mass-transport in the potential flow regime can be expected to hold when we fully exclude such boundary layer effects. Along with the definition of a dynamic permeability comes another characteristic length scale, Λ, which provides an estimate of the effective radius *available* for bulk transport. The electrical parameter Λ is then a characteristic length that correlates approximately with the connected pore-space in a way which the hydraulic radius is unable to do. In place of the hydraulic radius we could then rewrite the Kozeny-Carman relation as

$$k = \frac{b\Lambda^2}{F}. \tag{2.2.6.1}$$

2.2.7 Image Processing Methods in Estimating the Kozeny-Carman Parameters

Image processing methods have been extended to estimating the Kozeny–Carman parameters (*Berryman and Blair,* 1986, 1987). These methods, however, introduce approximations in the estimation of specific surface that arise from resolution constraints dictated by the image digitisation. *Berryman and Blair* (1987) showed that specific surface estimation could be derived from the tangent of the two-point correlation function at the origin, $S_2(r = 0)$. However, in order to extract meaningful information from image digitisation, a suitably prescribed magnification limit had to be imposed such that resolution constraints would not intrude into the analysis. The two-point correlation function represents the probability that two points a distance r apart are both in the same phase or material. For statistically isotropic materials, S_n becomes independent of direction and will only exhibit a dependency on the absolute value of the distances between the n points. If we then take the two point correlation function under the condition $r = |r|$, we note the following properties (*Berryman and Blair,* 1987):

$$S_2(0) = \phi, \tag{2.2.7.1}$$

$$\lim_{r\to\infty} S_2(r) = \phi^2, \tag{2.2.7.2}$$

$$\frac{dS_2(0)}{dr} = \frac{-S}{4}. \tag{2.2.7.3}$$

The derivative of the two-point correlation function at the origin is related to the specific surface area by (2.2.7.3). This relationship was originally found by *Debye et al.* (1957) in their studies of isotropic media. This result was subsequently generalised to anisotropic media by noting that the angular average of the anisotropic two-point spatial correlation function has the same relationship to the specific surface area (*Berryman*, 1987). It was concluded that an ideal correlation length estimate for a thin section would be approximately 100 times larger than the size of an image segment, and so the measurement of specific surface area (as a pore structure parameter) will become acceptable at a given pixel size. *Berryman and Blair* (1987) proposed that the pixel size, h, be approximately 1% of the size of an average pore radius, such that

$$h \cong r_c / 100 . \tag{2.2.7.4}$$

The above criterion restricts the measurement error in the average pore radius due to surface roughness and pixel quantization to be of the order of 1%. The magnification cannot be increased to the point where an average pore diameter is larger than the width of the digitised image. Consequently, we may conclude that there is little advantage in increasing the image magnification past the point where h violates these limits.

The effects of roughness on the validity of (2.2.1.4) were assessed by *Berryman and Blair* (1987) by means of upper and lower bounds to the Kozeny–Carman parameters. Consider a nominally circular rough-walled pore, as in Figure 2.2.2, the actual permeability of this pore is bounded as follows:

$$\frac{\phi_i^3}{2S_i^2} = k_i \le k \le k_o = \frac{\phi_o^3}{2S_o^2}, \tag{2.2.7.5}$$

where the subscript i denotes the smallest inscribed circle, and the subscript '$_o$' refers to the smallest circumscribed circle.

If we consider a mean pore radius defined as

$$\bar{r} = \frac{r_o + r_i}{2}, \tag{2.2.7.6}$$

we may write the bounds as

$$\frac{\bar{r}^4}{8}(1-\varepsilon)^4 = k_{min} \le k \le k_{max} = \frac{\bar{r}^4}{8}(1+\varepsilon)^4, \tag{2.2.7.7}$$

where ε denotes the relative roughness, denoted by

$$\varepsilon = \frac{r_o - r_i}{\bar{r}}. \qquad (2.2.7.8)$$

An error of 1% in the estimate of r would produce an error of no more than 4% in the permeability. This also supports the resolution constraints dictated in (2.2.7.4).

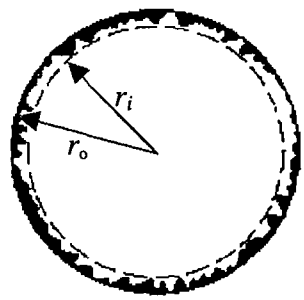

Figure 2.2.2 Schematic drawing of a rough-walled tube (after *Berryman and Blair,* 1987).

Table 2.2.2 Comparison of porosity and permeability values with those obtained from laboratory measurements (*Berryman and Blair,* 1986).

Sample	Magnification	S (μm^{-1})	Porosity		Permeability k(D)		F
			Image	Laboratory	Image	Laboratory	
Glass beads (55μm)	50	0.0241	0.35	0.3	9.7	8.7	10.9
	78	0.0281	0.43	0.3	10.7	8.7	10.9
Berea	100	0.0281	0.17	0.15-0.18[a]	0.312	0.023[a]	62[c]
Berea	200	0.0354	0.18	0.15-0.18[a]	0.197	0.023[a]	62[c]
Berea	490	0.1109	0.233	0.15-0.18[a]	0.021[b]	0.023[a]	62[c]
Berea	100	0.1231	0.393	0.15-0.18[a]	0.016[b]	0.023[a]	62[c]

[a] Computed using image porosity for magnification 100X

[b] *Daily and Lin* (1985)

[c] *Dullien* (1992)

In general the Kozeny-Carman equation is fairly accurate for unconsolidated sands, but overpredicts the permeability for consolidated sands such as sandstones (*Berryman and Blair,* 1986). Table 2.2.2 illustrates permeability estimates of 16 and 21 mD using the relevant input parameters as derived from thin section measurements, in comparison with the laboratory measurement of 23 mD (*Daily and Lin*, 1985). The formula used in all cases was (2.2.4.6). The underestimation is due to using a value of Kozeny's constant, b = 0.5. If the permeability is recalculated using b = 1/15, a value of 23 mD is obtained.

2.2.8 Numerical Approaches to the Kozeny-Carman Relation

Adler (1992) also made an assessment of the Kozeny-Carman equation in his studies of Stokes flow through fractal capillary networks. He considered the Sierpinski carpet and the fractal foam, which are two and three-dimensional versions of the Cantor set (*Mandelbrot,* 1982). It was noted that the porosity of the fractal foam at the third iteration in the fractal generation scheme is comparable to the porosity of Sierpinski carpets at the first generation. However, the three-dimensional permeability is much smaller than the two-dimensional permeability (*Lemaitre and Adler,* 1990).

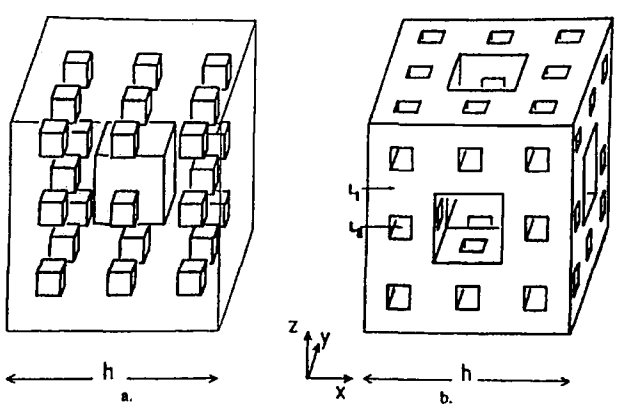

Figure 2.2.3 In (a), a triadic foam is displayed. Figure (b) can be viewed in two different ways since both phases are continuous; when the liquid phase corresponds to L_I, it is the Menger sponge of type 1 (MS1); when it corresponds to L_{II}, it is the Menger sponge of type II (MS2). The lattices shown here at the second construction stage (*Lemaitre and Adler,* 1990).

Adler (1986) concluded that the longitudinal permeability of Sierpinski carpets was in agreement with the predictions of the Carman equation. For the same iteration, the order

of magnitude of the permeabilities are the same. They can, however, be arranged in the following order for a given generation N:

$$k_{\perp} < k_{\parallel} < k. \tag{2.2.8.1}$$

The Kozeny constant was found to be close to 3.5, which is close to experimental values. The situation is less well determined for transversal flows in Sierpinski carpets. For the first generations, the Kozeny constant oscillates (*Delannay,* 1990; and *Adler,* 1992). Two types of asymptotic behavior are observed as N increases for the MS1 and MS2 fractals (*Lemaitre and Adler,* 1990). In the MS1 case, successively narrower pores are offered to the fluid when the iteration number increases, progressively hindering the circulation of the fluid as a whole. With MS2 however, the permeability tends towards a finite value when the wetted area increases since the largest pores are not modified when N increases, only successively smaller pores are added, and since the fluid does not circulate easily in these narrow pores, the overall permeability is not significantly altered.

2.3 Anisotropic Permeability

2.3.1 Introduction

"Anisotropy" refers to the directional variability of an observable quantity at a point in a body. It is distinct from the statistical heterogeneity of a porous medium, since the latter terminology refers to the spatial variation of an observable quantity at different points in the sample. It may also be noted that larger scale anisotropy may result from heterogeneities at smaller scales.

The form of Darcy's law that has been previously written for an isotropic medium, where there is flow in only one direction, was extended by *Ferrandon* (1948) to account for three different flow rates in three orthogonal directions only, as follows:

$$q_i = -\frac{A}{\eta}\left\{k_{ix}\frac{\partial p}{\partial x} + k_{iy}\frac{\partial p}{\partial y} + k_{iz}\frac{\partial p}{\partial z}\right\}. \tag{2.3.1.1}$$

This leads us to consider the permeability as having tensorial properties. Hence, one defines a permeability tensor, **k**, containing nine components, this arising from the coupling of the two vector fields, the velocity gradient and the pressure (or potential) gradient. Thus, the tensor form of Darcy's equation can be expressed as

$$\mathbf{q} = -\frac{\mathbf{k}}{\eta}\nabla p\,, \tag{2.3.1.2}$$

where $\mathbf{k}$ is a tensor of rank two, with components k_{ij}:

$$\mathbf{k} = \begin{pmatrix} k_{xx} & k_{xy} & k_{xz} \\ k_{yx} & k_{yy} & k_{yz} \\ k_{zx} & k_{zy} & k_{zz} \end{pmatrix}. \tag{2.3.1.3}$$

2.3.2 Observation and Experimental Measurement of Permeability Anisotropy

Anisotropy, like heterogeneity, is a scale-dependent property of naturally-occurring porous media (*Dagan*, 1986). Core-scale measurements on sandstones where bedding and crossbedding were quite marked typically give maximum-to-minimum permeability ratios no greater than about 3:1 (*Rose,* 1982). However, measurements of permeability anisotropy in field applications and on whole cores can reveal horizontal permeabilities as much as a factor of ten times larger than the vertical permeabilities (*Prats*, 1972). It has been conjectured that the origin of such a large directional dependence is a consequence of the hetrogenieties that may typically exist at scales smaller than the scale of the measurement (*Bernabé*, 1992).

At a scale smaller than that of alternation in a sand-shale sequence, depositional processes may also result in preferential orientations of the grains *within* the bedding plane. This causes variations in the horizontal permeability. This azimuthal variation in anisotropy has been noted by *Johnson and Hughes* (1948) and independently by *Dranchuk and Tait* (1981). More recently, *Hailwood and Bowen* (1999) demonstrated that differences of 10-15% between horizontal and vertical permeabilities in laboratory-scale measurements are quite common. *Johnson and Hughes* (1948) measured permeability as a function of the azimuth for an orientated, hollow core. Furthermore, each directional measurement was performed using a different position of the core. It remains uncertain, however, whether the observed variations in the measured permeabilities was due to a directional effect, or due to heterogeneities. Indeed, *Hailwood and Bowen* (1999) point out that a further underlying limitation of azimuthal permeability data is the difficulty of carrying out a full, three-dimensional permeability anisotropy determination owing to the potential spatial variability that arises when

sampling orientated cores from natural formations. In a conventional full-diameter core analysis however, it is common practice to determine a single vertical permeability and two horizontal transverse permeabilities at right angles to each other. The transverse measurements are obtained by inserting the core into a holder designed so that the core axis is vertical, permitting horizontal gas flow through a designated sector of the surface. The core is then rotated through an angle of $\pi/2$ and the gas-flow measurement repeated (*Kelton*, 1950; *Collins*, 1952). The extension of the experimental technique and apparatus of laboratory permeametry for the estimation of directional permeability in porous media has been reviewed by *Rice et al.* (1970).

The use of minipermeametry on both reservoir cores in the laboratory and rock outcrops in field studies has proven useful in the acquisition of localised permeability measurements by non-destructive means (*Goggin et al.*, 1988). The underlying principle of the technique is that a localised flow of an inert gas such as nitrogen can be induced by injection through a small tip seal directly into a sample of porous material. For a given pressure differential, the flowrate will be proportional to the permeability of the rock at the point of injection, assuming that the flow is both laminar and steady-state. *Young* (1989) has used minipermeametry in the determination of directional permeability of a core plug.

Controversy surrounds the technique due to uncertainties in the measurement arising from the boundary effects attributable to the samples geometry and finite size. The validity of the method is also the subject of ongoing debate relating to the complexity of the flow geometry (*Tartakovsky et al.*, 2000).

2.3.3 Diagonalisation of the Tensor Form of Darcy's Law

Despite the issue of heterogeneity, an important theoretical issue that arises is establishing the link between the experimental permeabilities, taken in field co-ordinates, and the co-ordinate system that gives the principal magnitudes of the permeability. To transform Darcy's law from field co-ordinates to a co-ordinate system in which $\mathbf{k}$ is a diagonalised matrix requires the use of a transformation that may be written formally in matrix notation as

$$\mathbf{C}^{-1}\mathbf{k}\mathbf{C} = \mathbf{D}, \qquad (2.3.3.1)$$

where $\mathbf{C}$ and its inverse $\mathbf{C}^{-1}$ are orthogonal matrices, whose columns are the normalised eigenvectors of the $\mathbf{k}$ matrix, and represent the permeability tensor in the co-ordinate system in which the tensor is diagonal.

Owing to the indistinguishability of the covariant character of the pressure gradient vector and covariant character of the flow rate vector in an orthogonal co-ordinate system, we may provide the following relations between an arbitrary co-ordinate system and the principal co-ordinate system, denoted by a circumflex. These relations will thus provide the values of the filter velocity vector and applied pressure gradient in the original system and in the system for which the permeability tensor is diagonal:

$$\hat{\mathbf{q}} = \mathbf{C}\mathbf{q} \ , \tag{2.3.3.2}$$

$$\hat{\nabla} p = \mathbf{C}\nabla p \, , \tag{2.3.3.3}$$

and conversely,

$$\mathbf{q} = \mathbf{C}^{-1}\hat{\mathbf{q}} , \tag{2.3.3.4}$$

$$\nabla p = \mathbf{C}^{-1}\hat{\nabla} p \, . \tag{2.3.3.5}$$

Note that the transformations (2.3.3.4) and (2.3.3.5) are corresponding inverses of (2.3.3.2) and (2.3.3.3), and that the mappings are bijective. Thus, again in matrix notation, we rewrite equation (2.3.1.2.), using (2.3.3.2) as

$$\hat{\mathbf{q}} = -\frac{1}{\eta}\mathbf{C}\mathbf{k}(\mathbf{C}^{-1}\hat{\nabla} p) , \tag{2.3.3.6}$$

and so by equations (2.3.3.1), (2.3.3.2) and (2.3.3.3), Darcy's equation in rotated co-ordinates is

$$\hat{\mathbf{q}} = -\frac{\mathbf{D}}{\eta}\hat{\nabla} p , \tag{2.3.3.7}$$

where $\mathbf{D} = \mathbf{C}\mathbf{k}\mathbf{C}^{-1}$. The permeability tensor corresponding to the original *field* co-ordinates, and the transformed matrix may therefore be found by evaluating the characteristic equation for $\mathbf{k}$:

$$\det(\mathbf{k} - \lambda\mathbf{I}) = 0 . \tag{2.3.3.8}$$

Thus, finding the roots of the resulting cubic equation defined by (2.3.3.8) provides the principal components of the permeability (eigenvalues) in the rotated co-ordinate system, and therefore the three unit eigenvectors corresponding to the **C** matrix in the diagonalised system. Consequently, we may then write Darcy's law in terms of the diagonalised tensor as

$$\begin{pmatrix} q_X \\ q_Y \\ q_Z \end{pmatrix} = -\frac{1}{\eta}\begin{pmatrix} k_{XX} & 0 & 0 \\ 0 & k_{YY} & 0 \\ 0 & 0 & k_{ZZ} \end{pmatrix}\begin{pmatrix} \partial p_X / \partial X \\ \partial p_Y / \partial Y \\ \partial p_Z / \partial Z \end{pmatrix}, \tag{2.3.3.9}$$

and so the three components of the velocity are

$$q_X = -\frac{k_{XX}}{\eta}\frac{\partial p_X}{\partial X}, \tag{2.3.3.10}$$

$$q_Y = -\frac{k_{YY}}{\eta}\frac{\partial p_Y}{\partial Y}, \tag{2.3.3.11}$$

$$q_Z = -\frac{k_{ZZ}}{\eta}\frac{\partial p_Z}{\partial Z}. \tag{2.3.3.12}$$

2.3.4 Obtaining the Experimental Permeabilities for a Cylindrical Core

We now outline the procedure for reconstructing the components of the permeability tensor when one of the principal axes are assumed to be perpendicular to the bedding plane, and consequently restrict our attention the co-ordinate transformations that involve rotations about the vertical axis.

The Mohr Circle construction allows a relationship between non-principal permeability measurements and the permeability parallel to the bedding plane to be established. Relations between these components have been previously derived by *Nye* (1957), *Szabo* (1968) and *Bear* (1972) for a two dimensional porous medium. Szabo derived these components by use of the following transformation law for a mixed tensor

$$\bar{k}^{i}_{j} = \frac{\partial x^r}{\partial \bar{x}^i}\frac{\partial \bar{x}^j}{\partial x^s}k^r_s = a_{ri}a_{sj}k^r_s, \tag{2.3.4.1}$$

where the derivatives form the components of the Jacobian matrix **J**, and correspond to the direction cosines that relate the original co-ordinate system to the new co-ordinate system. Expanding (2.3.4.1) in full matrix form gives

$$\begin{pmatrix} \bar{k}_{xx} & \bar{k}_{xy} \\ \bar{k}_{yx} & \bar{k}_{yy} \end{pmatrix} = \begin{pmatrix} \cos\theta & \sin\theta \\ -\sin\theta & \cos\theta \end{pmatrix} \begin{pmatrix} k_{xx} & k_{xy} \\ k_{yx} & k_{yy} \end{pmatrix} \begin{pmatrix} \cos\theta & \sin\theta \\ -\sin\theta & \cos\theta \end{pmatrix}^T$$

$$= \begin{pmatrix} \cos\theta & \sin\theta \\ -\sin\theta & \cos\theta \end{pmatrix} \begin{pmatrix} k_{xx} & k_{xy} \\ k_{yx} & k_{yy} \end{pmatrix} \begin{pmatrix} \cos\theta & -\sin\theta \\ \sin\theta & \cos\theta \end{pmatrix}, \qquad (2.3.4.2)$$

which can be written in component form as

$$\bar{k}_{xx} = \frac{k_{xx} + k_{yy}}{2} + \frac{k_{xx} - k_{yy}}{2}\cos 2\theta + k_{xy}\sin 2\theta, \qquad (2.3.4.3)$$

$$\bar{k}_{yy} = \frac{k_{xx} + k_{yy}}{2} - \frac{(k_{xx} - k_{yy})}{2}\cos 2\theta - k_{xy}\sin 2\theta, \qquad (2.3.4.4)$$

$$\bar{k}_{xy} = \bar{k}_{yx} = k_{yx}\cos 2\theta - \frac{(k_{xx} + k_{yy})}{2}\sin 2\theta, \qquad (2.3.4.5)$$

where use has been made of the identities $2\sin^2\theta = 1 - \cos 2\theta$ and $2\cos^2\theta = 1 + \cos 2\theta$.

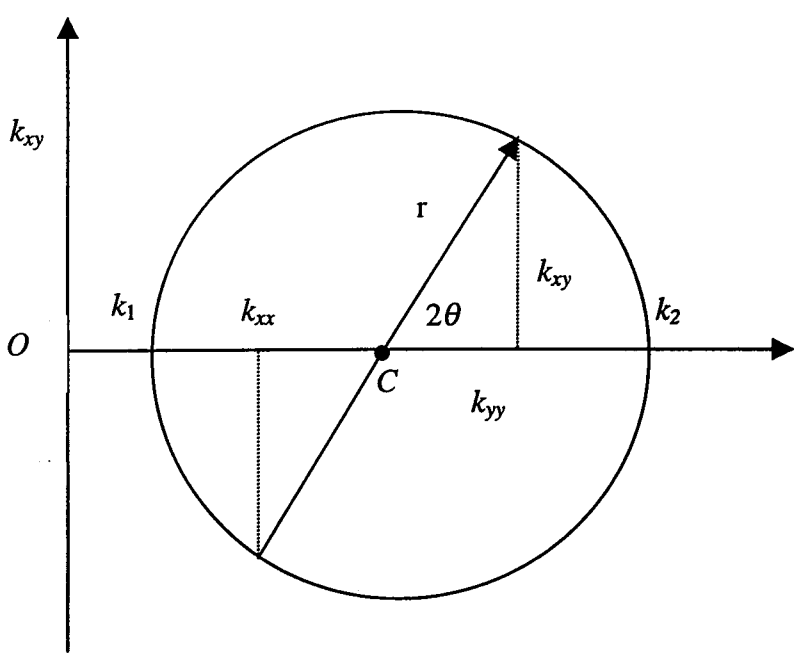

Figure 2.3.1 Mohr Circle construction showing the relation between directional permeabilities k_{xx} and k_{yy} measured in field co-ordinates and the principal permeabilities k_1 and k_2, obtained by rotating the former through an angle of 2θ.

The transformation of permeability components as given in the relations (2.3.4.3-5) can be geometrically interpreted by use of the Mohr Circle. In the present notation k_1 and k_2 refer to the two principal components, where $k_1 \leq k_2$ by convention, k_{xx} and k_{yy} are any two orthogonal measurements of permeability that in general are not principal, and k_{xy} is an off-diagonal component of the permeability tensor that will of course vanish in the principal co-ordinate system.

The distance OC, given by

$$OC = \frac{1}{2}\left(k_{xx} + k_{yy}\right) = \frac{1}{2}\left(k_1 + k_2\right), \tag{2.3.4.6}$$

is invariant to any rotation. The distance r can be expressed as

$$r = \frac{1}{2}(k_2 - k_1), \tag{2.3.4.7}$$

and can be obtained from the non-principal measurements by the following trigonometric expressions:

$$\cos 2\theta = \frac{k_{yy} - k_{xx}}{2r}, \qquad r = \sqrt{\frac{1}{4}(k_{yy} - k_{xx})^2 + (k_{xy})^2}\,. \tag{2.3.4.8}$$

From the Mohr circle construction we can find expressions for the principal components in terms of the two non-principal orthogonal measurements:

$$k_1 = \frac{1}{2}(k_{xx} + k_{yy}) - r, \tag{2.3.4.9}$$

$$k_2 = \frac{1}{2}(k_{xx} + k_{yy}) + r. \tag{2.3.4.10}$$

We now require an analytical expression for our third measurement. In practice, this measurement is taken at some intermediate angle α between k_{xx} and k_{yy}. Denoting this as k'_{xx}, we have

$$k'_{xx} = \frac{1}{2}(k_1 + k_2) + \frac{1}{2}(k_2 - k_1)\cos 2(\theta + \alpha). \qquad (2.3.4.11)$$

If $\alpha = 45^0$, then

$$k'_{xx} = \frac{1}{2}(k_1 + k_2) + \frac{1}{2}(k_2 - k_1)\cos 2(\theta + 45^0). \qquad (2.3.4.12)$$

Since $\cos 2(\theta + 45^0) = -\sin 2\theta$, the expression for the intermediate permeability measurement becomes

$$k'_{xx} = \frac{1}{2}(k_1 + k_2) - \frac{1}{2}(k_2 - k_1)\sin 2\theta. \qquad (2.3.4.13)$$

In light of equations (2.3.4.6 - 2.3.4.8), we note that

$$\tan 2\theta = \frac{k_{xx} + k_{yy} - 2k'_{xx}}{k_{yy} - k_{xx}}. \qquad (2.3.4.14)$$

From the Mohr circle construction we also have

$$\tan 2\theta = \frac{2k_{xy}}{k_{yy} - k_{xx}}. \qquad (2.3.4.15)$$

Thus, equating (2.3.4.14) with (2.3.4.15), gives the following relationship between the off-diagonal components, and the three (laboratory) measurements:

$$k_{xx} + k_{yy} - 2k'_{xx} = k_{xy}. \qquad (2.3.4.16)$$

Inverting (2.3.4.14) and (2.3.4.15) yields

$$2\theta = \tan^{-1}\left[\frac{k_{xx} + k_{yy} - k'_{xx}}{k_{yy} - k_{xx}}\right] = \tan^{-1}\left[\frac{k_{xy}}{k_{yy} - k_{xx}}\right]. \qquad (2.3.4.17)$$

It is now straightforward to calculate the angle 2θ for which the off-diagonal terms in the tensor will vanish. Alternatively, we may compute the principal terms directly, since we can write r as

$$r = \sqrt{\left\{\frac{1}{2}(k_{yy} - k_{xx})\right\}^2 + \left\{\frac{1}{2}(k_{xx} + k_{yy} - 2k'_{xx})\right\}^2}. \qquad (2.3.4.18)$$

and then insert this expression for r into equations (2.3.4.9) and (2.3.4.10) for the principal permeabilities.

2.3.5 Experimental Methodologies for Three-Dimensional Anisotropy

Hailwood and Bowen (1999) investigated the problem of reconstructing the full tensor in three dimensions from experimental measurements. The procedure in three dimensions involves permeability estimations across the three pairs of faces of a cubic sample, orientated either parallel or perpendicular to the bedding planes in the parent core. A smaller sample is then cut from within this cube with the required diagonal orientation.

Measurements along the faces of the inner cube are then made to provide the diagonal measurements. An obvious disadvantage of this method is that permeability data is collected from cubic samples of different sizes, which can make the scaling and combination of the two sets of measurements problematic.

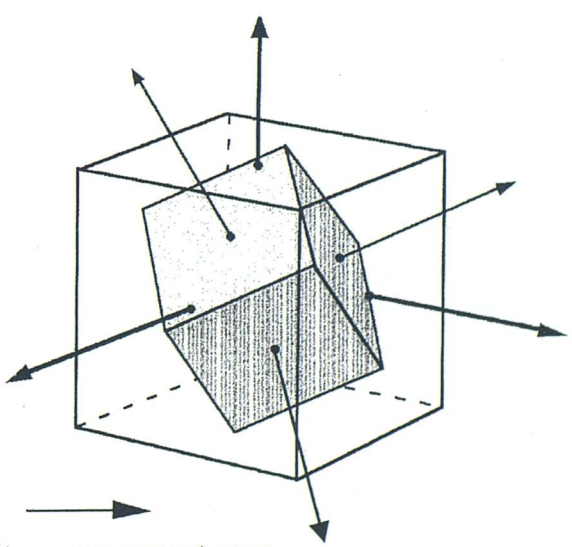

Figure 2.3.2 Diagram illustrating the diagonal orientation of a smaller cube cut to provide ''non-principal'' measurements from an original cube orientated for ''principal measurents'' relative to the bedding planes in the sediment (after *Hailwood and Bowen*, 1999).

An alternative approach, also used by *Hailwood and Bowen* (1999) and generally considered the more reliable of the two methods despite the fact that it reintroduces the

problem of sampling heterogeneity, is to cut three separate cubes from a single bed, all identical in size.

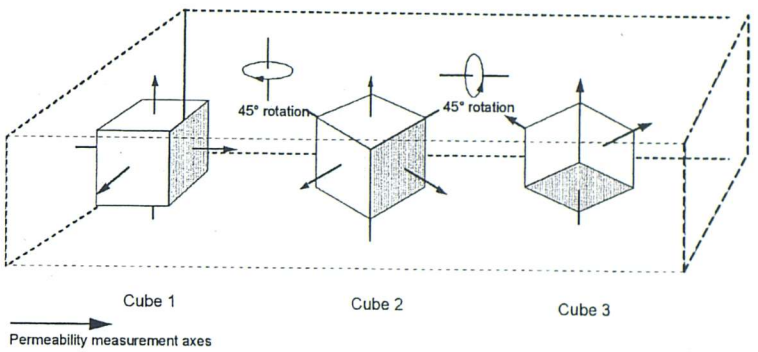

Figure 2.3.3 Schematic showing three separate cubes cut at different orientations relative to the bedding planes (after *Hailwood and Bowen*, 1999).

The first cube is used for the "principal" measurements, the second provides diagonal measurements within the bedding plane, and the third is used to provide diagonal measurements out of the bedding plane.

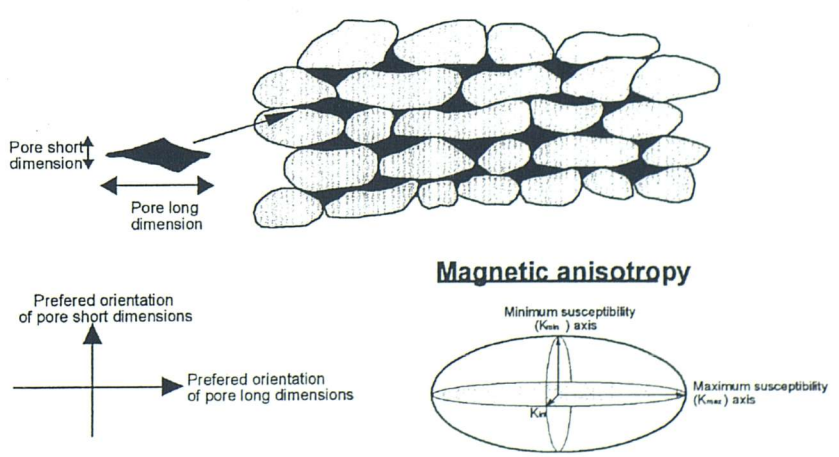

Figure 2.3.4 The relationship between maximum and minimum susceptibility axes and preferred orientations of pore long and short axes in a sample in which the pore space is filled with ferrofluid (after *Hailwood and Bowen*, 1999).

A method that also claims to provide the principal directions of the permeability tensor in three dimensions *directly* has also been investigated by *Hailwood and Bowen* (1999). This involves saturating a cubic sample with a ferrofluid and examining the

directionality of the magnetic susceptability (*Pfleiderer and Halls,* 1990). The assumption made is that the principal directions of magnetic susceptability coincide with those of permeability (*Hailwood and Bowen,* 1999). The technique, termed 'MAGPORE', thus defines the pore fabric of the formation by detecting the magnetic response of the ferrofluid that arises from the statistical alignment of the pores (*Lisle,* 1989; *Jezek and Hrouda,* 2000). The magnetic response can be described in three dimensions by an ellipsoid of magnetic susceptability. It should not, however, be assumed that the principal axes of this ellipsoid will coincide with the principal axes of the permeability ellipsoid, as these axes correspond to entirely different physical quantities whose directional properties are not necessarily related.

2.3.6 The Representation of Directional Permeability

The problem of relating measured directional permeability to the components of **k** with respect to either the flow gradient or the hydraulic head gradient was investigated by *Scheidegger* (1963), who distinguished two alternative formulations.

Case 1. The component of the filter velocity is taken in the direction of the pressure gradient and used in Darcy's law. In this instance, it is the direction of the pressure gradient defined by **n**, so the then the component of the flow rate vector q_n parallel to **n** is given by the inner product:

$$q_n = \mathbf{q} \cdot \mathbf{n} = \mathbf{n}^{\mathrm{T}}\mathbf{q}. \tag{2.3.6.1}$$

Since ∇p lies in the **n** direction, we can write

$$\nabla p = (\nabla p \cdot \mathbf{n})\mathbf{n} = \nabla p_n \mathbf{n}. \tag{2.3.6.2}$$

Furthermore, we may write a version of Darcy's law (equation 2.3.1.2) along an arbitrary direction **n** as

$$q_n = -k_n \nabla p_n, \tag{2.3.6.3}$$

which serves to define the permeability k_n in the **n** direction. Equation (2.3.6.3) may be substituted into (2.3.1.2) to yield

$$q_n = \mathbf{n}^{\mathrm{T}}\mathbf{q} = -\mathbf{n}^{\mathrm{T}}\mathbf{k}\nabla p = -\mathbf{n}^{\mathrm{T}}\mathbf{k}\nabla p_n \mathbf{n} = -\mathbf{n}^{\mathrm{T}}\mathbf{k}\mathbf{n}(\nabla p_n). \tag{2.3.6.4}$$

Equating this expression with (2.3.6.3) gives

$$k_n = \mathbf{n}^{\mathrm{T}}\mathbf{k}\mathbf{n}. \tag{2.3.6.5}$$

By means of the transformation (2.3.3.1), we can then diagonalise **k** to obtain (2.3.6.6)

$$k_n = \mathbf{n}^{\mathrm{T}}\mathbf{D}\mathbf{n} = \begin{pmatrix} n_X & n_Y & n_Z \end{pmatrix} \begin{pmatrix} k_{XX} & 0 & 0 \\ 0 & k_{YY} & 0 \\ 0 & 0 & k_{ZZ} \end{pmatrix} \begin{pmatrix} n_X \\ n_Y \\ n_Z \end{pmatrix}. \tag{2.3.6.6}$$

where k_n now represents the permeability in an arbitary direction in the new co-ordinate system. Carrying through the algebra we eventually obtain

$$k_n = \begin{pmatrix} n_X k_{XX} & n_Y k_{YY} & n_Z k_{ZZ} \end{pmatrix} \begin{pmatrix} n_X \\ n_Y \\ n_Z \end{pmatrix} = \left(n_X^2 k_{XX} + n_Y^2 k_{YY} + n_Z^2 k_{ZZ} \right). \tag{2.3.6.7}$$

If the principal axes of the symmetric permeability tensor are chosen as co-ordinate axes, the tensor consequently becomes diagonal and expression (2.3.6.7) will represent k_n. Denoting the principal permeabilities (eigenvalues) as k_{XX}, k_{YY}, and k_{ZZ}, and denoting the angles between **n** and the principal axes (X,Y,Z) by α, β and γ respectively, then we may write the unit vector **n** in terms of the component of the three direction cosines that specify the direction of $\mathbf{q}_I$:

$$\frac{\mathbf{q}_I}{|\mathbf{q}_I|} = \mathbf{n} = n_x\mathbf{e}_x + n_y\mathbf{e}_y + n_z\mathbf{e}_z = (\cos\alpha)\mathbf{e}_x + (\cos\beta)\mathbf{e}_y + (\cos\gamma)\mathbf{e}_z. \tag{2.3.6.8}$$

Substituting for **n** in equation (2.3.6.7) then gives the following for the directional permeability in an arbitary direction:

$$k_n = k_{XX}\cos^2\alpha + k_{YY}\cos^2\beta + k_{ZZ}\cos^2\gamma. \tag{2.3.6.9}$$

Case 2. The filter velocity is measured directly and the component of the pressure gradient in the direction of the filter velocity must be used in Darcy's law. If we let the direction of the filter velocity be given by the unit vector **n**, then the component ∇p_n of the pressure gradient parallel to **n** is given by

$$\nabla p_n = \nabla p \cdot \mathbf{n} = \mathbf{n}^{\mathrm{T}}\nabla p. \tag{2.3.6.10}$$

Rearranging Darcy's law for ∇p then gives

$$\nabla p = -\mathbf{k}^{-1}\mathbf{q}\,. \tag{2.3.6.11}$$

But since **q** is in the **n** direction,

$$\mathbf{q} = (\mathbf{q}\cdot\mathbf{n})\mathbf{n} = q_n\mathbf{n}\,, \tag{2.3.6.12}$$

in which case

$$\nabla p_n = \mathbf{n}^{\mathrm{T}}\nabla p = -\mathbf{n}^{\mathrm{T}}\mathbf{k}^{-1}q_n\mathbf{n} = \mathbf{n}^{\mathrm{T}}\mathbf{k}^{-1}\mathbf{n}(-q_n)\,. \tag{2.3.6.13}$$

The filter velocity lies parallel to the unit vector **n**, so its component along the principal axes may be given as

$$q_n = -k_n\nabla p_n, \quad \text{or} \quad \nabla p_n = -\frac{1}{k_n}q_n\,. \tag{2.3.6.14}$$

Comparison of equations (2.3.6.13) and (2.3.6.14) shows that

$$k_n = \frac{1}{\mathbf{n}^{\mathrm{T}}\mathbf{k}^{-1}\mathbf{n}}\,. \tag{2.3.6.15}$$

Again, the unit vector **n** with respect to ∇p is given as

$$\frac{\nabla_I p_I}{|\nabla_I p_I|} = \mathbf{n} = n_X\mathbf{e}_x + n_Y\mathbf{e}_y + n_Z\mathbf{e}_z = (\cos\alpha)\mathbf{e}_x + (\cos\beta)\mathbf{e}_y + (\cos\gamma)\mathbf{e}_z\,. \tag{2.3.6.16}$$

Diagonalising **k** as before gives

$$k_n = \frac{1}{\mathbf{n}^{\mathrm{T}}\mathbf{D}^{-1}\mathbf{n}}\,. \tag{2.3.6.17}$$

We evaluate the denominator in (2.3.6.17) as follows

$$\mathbf{n}^{\mathrm{T}}\mathbf{D}^{-1}\mathbf{n} = \begin{pmatrix} n_X & n_Y & n_Z \end{pmatrix}\begin{pmatrix} 1/k_{XX} & 0 & 0 \\ 0 & 1/k_{YY} & 0 \\ 0 & 0 & 1/k_{ZZ} \end{pmatrix}\begin{pmatrix} n_X \\ n_Y \\ n_Z \end{pmatrix}$$

$$= \begin{pmatrix} \frac{n_X}{k_{XX}} & \frac{n_Y}{k_{YY}} & \frac{n_Z}{k_{ZZ}} \end{pmatrix} \begin{pmatrix} n_X \\ n_Y \\ n_Z \end{pmatrix} = \left(\frac{n_X^2}{k_{XX}} + \frac{n_Y^2}{k_{YY}} + \frac{n_Z^2}{k_{ZZ}} \right). \qquad (2.3.6.18)$$

Using (2.3.6.18), equation (2.3.6.17) becomes

$$k_n = \frac{1}{\mathbf{n}^T \mathbf{D}^{-1} \mathbf{n}} = \frac{1}{\left(\frac{n_X^2}{k_{XX}} + \frac{n_Y^2}{k_{YY}} + \frac{n_Z^2}{k_{ZZ}} \right)} = \frac{1}{\left(\frac{\cos^2 \alpha}{k_{XX}} + \frac{\cos^2 \beta}{k_{YY}} + \frac{\cos^2 \gamma}{k_{ZZ}} \right)}. \qquad (2.3.6.19)$$

Finally, we obtain the following expression for the directional permeability:

$$\frac{1}{k_n} = \frac{\cos^2 \alpha}{k_{XX}} + \frac{\cos^2 \beta}{k_{YY}} + \frac{\cos^2 \gamma}{k_{ZZ}}. \qquad (2.3.6.20)$$

Recognising that the diagonal components of **k** are the permeabilities along the principal axes of this tensor, two expressions for the directional permeability k_n may be derived for the measurement direction **n**. In general, these two definitions of the directional permeability are not equal. The fact that these two values are not equal arises from the fact that these two measurements consider two different orientations of the potential gradient and filter velocity. Taking either formulation, the direction cosines in equation (2.3.6.7) and (2.3.6.20) produce an ellipsoidal representation quadric of the diagonalised tensor, where $k_n^{1/2}$ is represented graphically as a function of the directions of **n** to produce an ellipse, whose principal axes are in the direction of the principal axes of the permeability tensor (Figure 2.3.5).

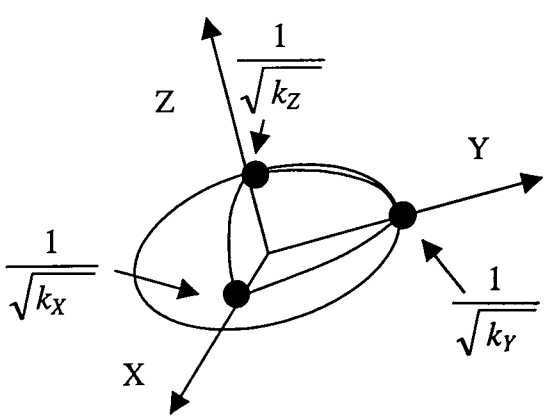

Figure 2.3.5 The representation quadric for permeability corresponding to case 1. The tensor is represented in the rotated co-ordinate system to give the principal axes of an ellipse with lengths ($1/\sqrt{k_n}$).

The permeability ellipsoid is an ellipsoid of revolution (*i.e.* a spheroid) if $k_{XX} = k_{YY}$. In matrix language this corresponds to a doubly degenerate eigenvalue, in which case **D** takes the form:

$$\mathbf{D} = \begin{pmatrix} k_{XX} & 0 & 0 \\ 0 & k_{XX} & 0 \\ 0 & 0 & k_{ZZ} \end{pmatrix}. \qquad (2.3.6.21)$$

In the case where $k_{XX} = k_{YY} = k_{ZZ}$, the system is triply degenerate and the tensor may be written as

$$\mathbf{D} = \begin{pmatrix} k_{XX} & 0 & 0 \\ 0 & k_{XX} & 0 \\ 0 & 0 & k_{XX} \end{pmatrix} = k_{XX} \begin{pmatrix} 1 & 0 & 0 \\ 0 & 1 & 0 \\ 0 & 0 & 1 \end{pmatrix} = k_{XX}\mathbf{I}. \qquad (2.3.6.22)$$

In a general permeability experiment, what is generally measured is the volumetric flux, Q/A. The non-equivalence of cases 1 and 2 arises from the fact that they do not both represent a situation in which the direction **n**, in which the flux is measured, lies parallel to the applied potential gradient. For example, when conducting a permeability measurement on an orientated cylindrical core plug, **n** would be parallel to the axis of the core and the volumetric flux would then be *exactly* the flow rate per cross sectional area of the plug perpendicular to **n**; this corresponds to case 1. However, the second case refers to the situation in which the applied potential gradient is projected onto some direction **n** of the filter velocity vector, and so the apparent cross-sectional area across which the flow rate is measured becomes greater. Consequently, the measured volumetric flux would in general be relatively larger, since the quotient Q/A would no longer be a maximum. To date, no experimental method has been developed for the purpose of flux measurements corresponding to case 2, that is, at some general angle to the applied potential gradient. Consequently, the measurement of directional permeability is taken to suggest an experimental scheme following case 1, where the filter velocity is always measured parallel to the direction of the applied pressure gradient.

2.3.7 Symmetry of the Permeability Tensor

Much work has gone into proving that the permeability tensor is symmetric, that is, $k_{ij} = k_{ji}$ (*Szabo,* 1968). In fact, most research articles in connection with the tensor form of Darcy's law assume that **k** is indeed symmetric (*Case and Cochran,* 1972; *Guin et al.,* 1971). If we decide to operate on the assumption that **k** is symmetric, then we need only consider the six independent k_{ij} in the matrix. Furthermore, we note that symmetry of a matrix is a sufficient condition for its eigenvalues to be real and the corresponding eigenvectors to be orthogonal. The relationship $k_{ij} = k_{ji}$ is a consequence of Onsager's reciprocal relation (*Nye,* 1957) and is an empirical expression that is concerned only with a macroscopic description of the permeability tensor. Usually it is assumed that an anisotropic formation has three mutually orthogonal principal axes, and this assumption itself is sufficient to ensure the symmetry of **k**. Some authors, however, have tried to prove the symmetry of the permeability tensor on the basis of specific models representing the porous medium, but these are not general proofs.

2.3.8 Scheidegger's Argument for the Symmetry of k

The symmetry relation $k_{ij} = k_{ji}$ states that the permeability coefficient relating a pressure gradient in the i direction to the flux in the j direction is the same as the permeability coefficient relating a pressure gradient in the j direction to the flux in the i direction. We can prove the validity of the above relation for a rock whose permeability is due to sets of parallel conduits that may be orientated in arbitrary directions, as follows. Imagine a single circular tube of radius r, orientated in a direction defined by the vector **n**. If the pressure gradient is ∇p, then the projection of the pressure gradient along the axis of the tube is $\nabla p \cdot \mathbf{n}$. The vector ∇p can be written in the equivalent form $(\nabla p \cdot \mathbf{n})\mathbf{n}$. According to the Hagen-Poiseuille law, the flow vector through this tube can be expressed as

$$\mathbf{Q} = -\frac{\pi r^4}{8\eta}(\nabla p \cdot \mathbf{n})\mathbf{n}. \qquad (2.3.8.1)$$

If we now imagine that there are N tubes within an area A (measured in the plane perpendicular to **n**), the total flux vector will be

$$\mathbf{q} = \frac{\mathbf{Q}}{A} = -\frac{N(\mathbf{n})\pi r^4}{8A\eta}(\nabla p \cdot \mathbf{n})\mathbf{n} = -\frac{\nu(\mathbf{n})\pi r^4}{8\eta}(\nabla p \cdot \mathbf{n})\mathbf{n}, \qquad (2.3.8.2)$$

where $\nu(\mathbf{n}) = N(\mathbf{n})/A$ is the areal density of tubes. We may write this result in terms of indicial notation, with $\mathbf{n}$ replaced by n_i, the repeated indices implying summation over all possible values of that index:

$$q_j = -\frac{\nu\pi r^4}{8\eta}(\nabla_i p n_i)n_j . \tag{2.3.8.3}$$

We now recall the vector form of Darcy's law for an anisotropic medium,

$$q = -\frac{\mathbf{k}}{\eta}\nabla p , \tag{2.3.1.2}$$

which in indicial form can be written as

$$q_j = -\frac{k_{ji}}{\eta}\nabla_i p . \tag{2.3.8.4}$$

Thus, comparing (2.3.8.3) and (2.3.8.4), we obtain

$$q_j = \frac{\nu\pi r^4}{8\eta}(\nabla_i p n_i)n_j = \frac{k_{ji}}{\eta}\nabla_i p , \tag{2.3.8.5}$$

which shows that the permeability tensor is given by

$$k_{ji} = \frac{\nu\pi r^4}{8} n_i n_j . \tag{2.3.8.6}$$

If we interchange the directions of the pressure gradient and flux vector, we may write the similar expression

$$k_{ij} = \frac{\nu\pi r^4}{8} n_j n_i . \tag{2.3.8.7}$$

Due to the commutative nature of the product $n_i n_j$, expressions (2.3.8.6) and (2.3.8.7) are identical, and so $k_{ij} = k_{ji}$ for a set of N conduits orientated in an arbitrary direction $\mathbf{n}$.
As the sum of two or more symmetric matrices is also symmetric, expressions (2.3.8.6) and (2.3.8.7) may be extended to include all possible orientations of conduits by the following summations

$$k_{ij} = \sum_{l=1}^{l=n} \frac{\pi r_l^4}{8}(n_i n_j)_l \nu(\mathbf{l}) \tag{2.3.8.8}$$

$$k_{ji} = \sum_{l=1}^{l=n} \frac{\pi r_l^4}{8} (n_j n_i)_l v(\mathbf{l}), \qquad (2.3.8.9)$$

which then also satisfy (2.3.8.7). *Scheidegger* (1963) replaced these summations by integrating (2.3.8.6) and (2.3.8.7) over all possible orientations of conduits in a solid angle Ω to give

$$k_{ij} = \int \frac{\pi r^4}{8} (n_i n_j) v d\Omega = \int \frac{\pi r^4}{8} (n_j n_i) v d\Omega = k_{ji}. \qquad (2.3.8.10)$$

Inserting this expression into (2.3.6.3) gives

$$q_n = \frac{\pi r^4}{8} \int (n_i n_j) v d\Omega \nabla p_n = \frac{\pi r^4}{8} \int (n_j n_i) v d\Omega \nabla p_n, \qquad (2.3.8.11)$$

which is Scheidegger's argument for the symmetry of **k**. Expression (2.3.8.11), however, only applies to sets of non-interacting conduits, and is therefore not general.

2.4 Network Modelling, Percolation and Effective Medium Theories

2.4.1 Overview

The incorporation of the geometrical characteristics of the pore space into lattice representations allows network computations to incorporate both pore shape and orientation into the calculation. Thus, data representing the pore structure and interconnectivity of a porous rock can be mapped into a simplified network conforming to a two- or three-dimensional grid. These were known as branching type models (*Fatt,* 1956a,b), where the conduit system consisted of a multitude of capillaries arranged in the form of a regular array. Fatt initially adopted an electrical network analogy that was used to predict the capillary pressure characteristics of porous media (*Ksenzhek,* 1963; *Harris,* 1965). Application of the electrical resistor network was subsequently extended to permeability modelling, to establish a critical pathway analysis of fluid flow (*Friedman and Seaton,* 1998a).

Percolation theory treats the problem of fluid flow through a network of interconnected capillaries, consisting of nodes and conducting bonds connecting them. Furthermore, the theory shows that although the distribution of conducting bonds is random, there exists a well-determined threshold conductivity probability for a bond, when the network as a whole acquires conductivity. Percolation models were first

studied by *Broadbent and Hammersley* (1957), who developed lattice network representations of fluid flow through a rigid medium, and showed that no fluid would flow if the concentration of bonds is less than some threshold value. They also introduced the notion of the percolation probability, which served to indicate the extent to which conductance could take place through the network, or specifically the interconnectivity of the spanning cluster.

An alternative approach to the "exact" network model is the effective-medium approximation, generally valid away from the percolation threshold. In this instance an effective conductance (and hence effective permeability) is obtained by modelling the "true" heterogeneous medium by a statistically equivalent homogeneous network (*Kirkpatrick,* 1971). This approach thus derives a representative average conductance parameter without the extensive matrix computations required by an exact network model.

2.4.2 "Exact" Network Models

The regular network consists of periodic arrays of a unit cell, and will consequently possess some degree of symmetry. Indeed, several types of network geometry have been proposed for two- and three-dimensional networks, respectively (*Nicholson and Petropoulos,* 1971; *Chatzis and Dullien,* 1977; *Shankland and Waff,* 1974). Two-dimensional networks have been used more often than three-dimensional networks, due to their simplicity and ease of computability.

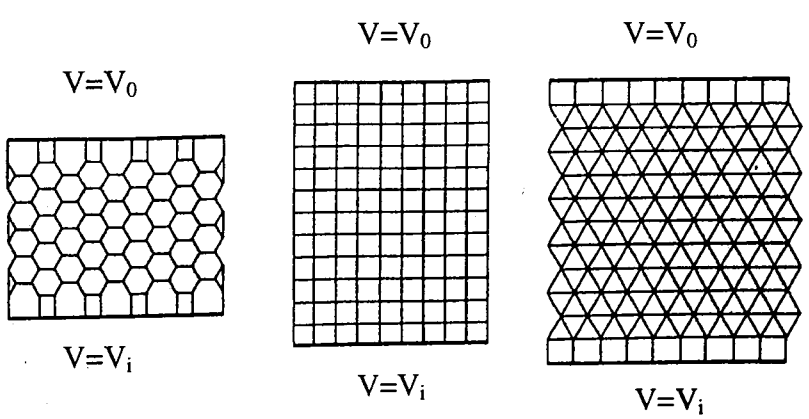

Figure 2.4.1 Examples of 2D lattices (hexagonal, square and triangular) used by *David et al.* (1990).

Among the two-dimensional arrays are the hexagonal lattice, the square lattice, and the triangular lattice, with co-ordination numbers of three, four, and six, respectively (*Chatzis and Dullien,* 1977). Nevertheless, it has become apparent that two-dimensional networks are not the most realistic representation of the pore space, and are restricted to modelling in single-phase flow, owing to the phase discontinuity in multiple-component systems.

2.4.3 Solution of the Network Conductance Problem

The estimation of the conductance parameters for regular networks is a well-established problem (for example, *Seeburger and Nur,* 1984), and involves a procedure of constructing a regular network of variable elements consisting of a node set $\{i\}$, and a bond set $\{ij\}$, connecting nodes i and j with conductance g_{ij}. The application of an external potential will consequently induce a distributed set of voltages $\{V_i\}$ on the node set and a current $i_{ij} = g_{ij}(V_i - V_j)$ then flows through the bonds. Furthermore, Kirchhoff's law of current conservation holds locally at each node i, so that

$$\sum_{j \to i} g_{ij}\left(V_i - V_j\right) = 0, \tag{2.4.3.1}$$

where the sum over $j \to i$ indicates a summation over all the bonds connected to the i^{th} node. For a regular (ordered) lattice, we may invoke a constant co-ordination number, z which allows us to represent the conduction problem algebraically as

$$\mathbf{Gv} = \mathbf{w}. \tag{2.4.3.2}$$

The elements of the conductance matrix **G** are given as (*David et al.,* 1990)

$$G_{ij} = \delta_{ij}\left(\sum_{k \to i} g_{ki}\right) - g_{ij}, \tag{2.4.3.3}$$

where a "pseudo-summation" convention has been used to describe the conductance of each node.

After solving equation (2.4.3.3) for **v**, it is straightforward to calculate the total current I_{tot} flowing out of the network by summing up the contributions of the conductances connected to the lower boundary of the network where $V = V_\infty$. The net conductance for the network is then given by

$$G_{eq} = \frac{I_{tot}}{V_\infty - V_0}. \qquad (2.4.3.4)$$

2.4.4 Deriving an Effective Conductance from the Exact Network Solution

If we now consider the situation for a regular network where all the conductances adopt a single value g_0, the equivalent conductance of the homogeneous network will be given by (*David et al.*, 1990)

$$G_{eq} = g_0 G[1], \qquad (2.4.4.1)$$

where G[1] represents the overall conductance of the equivalent homogeneous network with the same topology, with the local elements set to unity. David *et al.* give the following expression for G[1] on the square lattice, as a function of the number of bonds, p:

$$G[1] = \frac{p}{p+1}. \qquad (2.4.4.2)$$

In order to obtain g_{eff}, equations (2.4.3.4) and (2.4.4.1) are set equal to each other, and thus $g_0 = g_{eff}$, yielding

$$g_{eff} = \frac{I_{tot}}{(V_\infty - V_0)G[1]}. \qquad (2.4.4.3)$$

2.4.5 The Effective-Medium Approximation

Numerous attempts have been made to calculate the transport properties of heterogeneous media, specifically the resistance of binary mixtures of conducting materials. Initial studies used simple mixing laws that failed to adequately describe the behavior of insulating–conducting mixtures, a situation that represents fluid transport through a porous medium, where the grains act as the insulating phase. Such approaches were unsuccessful and were consequently superseded by the effective-medium theory suggested by *Kirkpatrick* (1973) based on the earlier work of researchers such as *Landauer* (1952). If we consider a heterogeneous continuum in which a local conductive property can be defined, we may approximate the conducting medium by a network with a regular topology, where each bond is occupied by a conductance g_k. To

account for heterogeneity, the set of all g_k follows some probability density function, and so it becomes possible to build up a network with the same topology, but in which all the conductances have a single effective value, g_{eff}. In doing this we effectively map all elements from $\{g_k\}$ to some single value, g_{eff}. To find a mathematical expression for the effective conductance g_{eff}, a classical self-consistent method can be employed in which a single conductance g_m is inserted into the homogeneous system. The inclusion of g_m in the effective medium locally disturbs the uniform field. If this procedure was repeated over all local conductances, the disturbing effects of embedding g_m into the voltage distribution should eventually average out to zero.

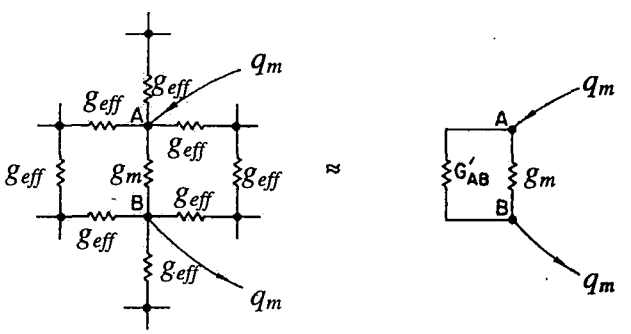

Figure 2.4.2 Construction used in calculating the voltage induced across one conductance, g_m, surrounded by a uniform medium (after *Kirkpatrick*, 1973).

In the self-consistent field approximation, the single conductances are calculated under the assumption that each bond is subject to a potential equivalent to all the others *plus* that due to an external potential; the external potential in this case is taken to be a continuous pressure. If we then consider one conductance orientated along the external pressure field surrounded by the effective medium (Figure 2.4.2), and having the value g_m, then the self-consistent solution in the presence of g_m is constructed by adding the effects of a fictitious current or flow rate, q_m, introduced at A and extracted at B, to the uniform field. Far from g_m, the perturbation is small and the solution will correspond to the uniform field. Across A and B however, the uniform solution fails to satisfy current conservation, and so the magnitude of q_m is chosen to account for this:

$$P_{eff}(g_{eff} - g_m) = q_m . \qquad (2.4.5.1)$$

The extra pressure, P_m, induced between A and B, can be calculated if we know the conductance G_{AB}' of the network between points A and B when the perturbation is absent. Then

$$P_m = \frac{q_m}{(g_m + G'_{AB})}. \tag{2.4.5.2}$$

The total flow rate through each of the z equivalent bonds at the points where the current enters and leaves is partitioned as q_m/z, so that a total flowrate of $2q_m/z$ passes through the AB bond. This then determines the pressure that develops across AB, and from that we deduce the following relationships:

$$G_{AB} = G'_{AB} + g_{eff}, \tag{2.4.5.3}$$

$$G_{AB} = (z/2)g_{eff}, \tag{2.4.5.4}$$

and so

$$G'_{AB} = (z/2 - 1)g_{eff}. \tag{2.4.5.5}$$

Substituting (2.4.5.1) and (2.4.5.5) into (2.4.5.2) then gives

$$P_m = P_{eff}\frac{g_{eff} - g_m}{[(z/2)-1]g_{eff} + g_m}. \tag{2.4.5.6}$$

Equation (2.4.5.6) is solved to give a new set of discrete conductances which are in turn used to construct new potentials. This iterative process is continued until no further significant changes occur, at which point the system is said to be *self-consistent.* The requirement that the average of P_m vanishes gives

$$\left\langle \frac{g_{eff} - g_k}{[(z/2)-1]g_{eff} + g_k} \right\rangle = 0, \tag{2.4.5.7}$$

where the angle brackets signify an averaging procedure with respect to the probability density function of the g_k. The co-ordination number z represents a mean value of the 'true' co-ordination number in the disordered material, and may be defined locally as the number of conducting bonds reaching a node in the network. Consequently, the relation above represents the minimisation of the discrepancies between g_m and g_k, normalised to

the macroscopic conductance of the homogeneous network model. Furthermore, as we are dealing with a random medium, we ignore any possible spatial correlation between the magnitude of the local conductances.

2.4.6 The Integral Form of the EMA and Examples of Closed-form Solutions

If the values of the g_k can be represented by a continuous probability density function, denoted as $p(g)$ defined within the conductance interval $g \in [G_1, G_2]$, then the averaging process above can be expressed as an integral of the form

$$\int_{G_1}^{G_2} p(g) \frac{g_{eff} - g}{[(z/2)-1]g_{eff} + g} dg = 0. \qquad (2.4.6.1)$$

For example, if $p(g)$ is uniform, *i.e.*,

$$p(g) = \frac{1}{G_1 - G_2}, \qquad (2.4.6.2)$$

then equation (2.4.6.1) can be evaluated analytically to yield the following explicit equation for g_{eff} (*David et al.*, 1990):

$$\frac{z}{2} g_{eff} \ln\left\{1 + \frac{(G_2 - G_1)}{[(z/2)-1]g_{eff} + G_1}\right\} = (G_2 - G_1), \qquad (2.4.6.3)$$

Schlueter (1995) solved (2.4.6.1) for a log-uniform distribution of the form $f(g) = (2g\ln G)^{-1}$ for $g \in [G^{-1}, G]$, for co-ordination numbers corresponding to a series arrangement of conductors ($z = 2$), a parallel arrangement of conductors, ($z = \infty$) and for the isotropic cubic lattice, ($z = 6$). The results were:

$z = 2$: $$g_{eff} = \frac{2G\ln G}{G^2 - 1}, \qquad (2.4.6.4)$$

$z = \infty$: $$g_{eff} = \frac{G^2 - 1}{2G\ln G}, \qquad (2.4.6.5)$$

$z = 6$: $$g_{eff} = \frac{G^{4/3} - 1}{2(G - G^{1/3})}. \qquad (2.4.6.6)$$

In the case $z = 6$, for very large G, the effective conductance may be approximated as

$$g_{eff} \approx \frac{1}{2} G^{1/3}. \qquad (2.4.6.7)$$

2.4.7 The Discrete Form of Kirkpatrick's Equation

In certain cases the distribution of the local conductance values may not always be fitted by means of a continuous distribution function, and in this situation the integral is replaced by a series:

$$\sum_{k=1}^{N} \frac{g_{eff} - g_k}{[(z/2)-1]g_{eff} + g_k} = 0, \qquad (2.4.7.1)$$

where N is the total number of conductors. As g_{eff} is a monotonic increasing function of z, the two cases $z = 2$ and $z = \infty$ provide the following bounds, which hold for all z:

$$N\left[\sum \frac{1}{g_i}\right]^{-1} \leq g_{eff}(z) \leq \frac{1}{N}\sum g_i \,. \qquad (2.4.7.2)$$

2.4.8 Anisotropic Effective-Medium Approximation

The effective-medium formalism of *Kirkpatrick* (1973) was subsequently extended to include anisotropic lattices, irrespective of their connectivity structure. *Bernasconi* (1974) showed that the isotropic effective-medium approximation works well for square lattices with anisotropic binary distributions, even at percolation. *Toledo et al.* (1992) extended the work of *Bernasconi* (1974) to make the anisotropic effective-medium approximation applicable to any regular lattice, regardless of its connectivity structure. The theory has been used to model the permeability of anisotropic fracture networks (*Harris,* 1990, 1992; *Hestir and Long,* 1990). An anisotropic resistor network can be represented by an equivalent anisotropic effective medium in which all bonds orientated along a particular direction v have the same effective conductance, denoted here as g_{eff}^{v}. As in the isotropic case we require that the extra voltages induced when individual conductances replace g_{eff}^{v} in the anisotropic medium average to zero. Thus, analogously to equation (2.4.5.7), we write

$$\left\langle \frac{g_{eff}^{v} - g_k}{S_v\{g_{eff}^{v=1}, \ldots g_{eff}^{v=d}\} + g_k} \right\rangle = 0. \qquad (2.4.8.1)$$

The effective bond conductances for each of the lattice directions can be self-consistently determined. We have, in accordance with equation (2.4.7.1):

$$\sum_{k=1}^{n} \frac{g_{eff}(v) - g_k}{S_v\{g_{eff}^{v=1}, \ldots g_{eff}^{v=d}\} + g_k} = 0, \qquad (2.4.8.2)$$

where d denotes the total number of lattice directions lattice directions. The term S_v in the denominator of (2.4.8.2) is a function of the directionally-dependent effective conductances, and is used to describe the connectivity of the lattice. For homogeneously isotropic lattices, equation (2.4.8.2) reduces to Kirkpatrick's result, equation (2.4.7.1). In this case, all the $g_{eff}(v)$ are then equal, and so calculating S_v becomes relatively straightforward by virtue of the network symmetry. For anisotropic networks the task is more complex, and analytical expressions for S_v are found by solving the appropriate set of Kirchhoff's equations or by the Fourier transform techniques employed by *Bernasconi* (1974). The function has been approximated in the case of a cubic network as (*Bernasconi,* 1974)

$$S_v\{g_{eff}^{v=1}, \ldots g_{eff}^{v=d}\} \approx g_m^{v=1} \frac{\tan^{-1}\left\{\sqrt{\left[g_{eff}^{v=1} g_{eff}^{v=2} + g_{eff}^{v=2} g_{eff}^{v=3} + g_{eff}^{v=3} g_{eff}^{v=1}\right]} / g_{eff}^{v=1}\right\}}{\tan^{-1}\left\{g_{eff}^{v=1} / \sqrt{\left[g_{eff}^{v=1} g_{eff}^{v=2} + g_{eff}^{v=2} g_{eff}^{v=3} + g_{eff}^{v=3} g_{eff}^{v=1}\right]}\right\}}. \qquad (2.4.8.3)$$

For $d = 3$ lattice directions, the problem of finding the effective conductances evolves into solving three non-linear simultaneous equations that are formed from a cyclic permutation of {1,2,3}. For lattices other than the square or simple cubic lattice, these techniques prove somewhat complicated, and *Toledo et al.* (1992) used the operational methods of *Van der Pol and Bremmer* (1950) to calculate S_v for a number of regular lattices with anisotropic distributions of conductances.

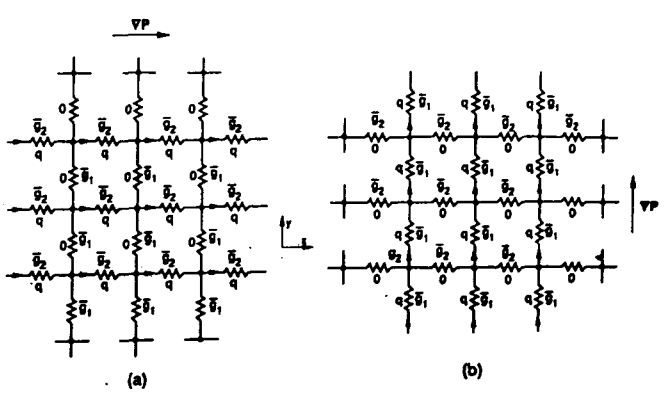

Figure 2.4.3 Flow pattern in the effective anisotropic lattice (after *Toledo et al.,* 1992).

Toledo et al. (1992) compared bond-percolation of the anisotropic medium permeability with that according to Monte Carlo calculations on a variety of two- and three-dimensional lattices, and found that the anisotropic effective-medium theory is accurate to within 5%, except near the percolation threshold of three-dimensional lattices.

2.4.9 Percolation Theory

Several reviews of percolation modelling exist in direct relation to fluid flow in porous media (*Alder,* 1992; *Dullien,* 1992; *Berkowitz and Balberg*, 1993; *Sahimi,* 1995; *Berkowitz and Ewing,* 1998). However, these rest on a broader literature, which examines percolation theory in greater generality (*Frisch and Hammersley,* 1963; *Shante and Kirkpatrick,* 1971; and *Stauffer and Aharony,* 1992). *Shante and Kirkpatrick* originally examined the role of percolation effects in the metal-semiconductor phase transitions that were observed in some disordered systems, and also the hopping conductivity in amorphous materials (*Ambegaokar et al.,* 1971).

The percolation threshold may be defined as the fraction of conducting sites that need to be present for conduction to occur across the network. A natural way of studying conducting networks is to remove all the bonds successively, and then reassign them to the network over multiple realisations until the most likely threshold cluster or critical path is obtained. After defining a threshold cluster, or critical subnetwork, we assume that flow localisation occurs on the backbone of the critical subnetwork, which is then designated as the "Critical Path".

Ambegaokar et al. (1971) considered an analogy between the flow of current by the mechanism of electron-hopping between the localised states in semiconductors at low temperatures and the flow between the nodes of a random network composed of individual conductances. It was suggested that close to percolation (that is, at sufficiently low temperatures) the conductance of such a network would be controlled by a critical or limiting conductance, g_c. This arises because current originating from isolated high-conductance zones or clusters inside the network has to pass through sites with conductances of the order g_c in order to traverse the system. For a set of conductances distributed log-uniformly over the interval $[G^{-1},G]$ with density $f(g) = (2g\ln G)^{-1}$, the critical conductance g_c takes the form (*Schlueter*, 1995)

$$g_c = G^{\frac{1}{2}}. \qquad (2.4.9.1)$$

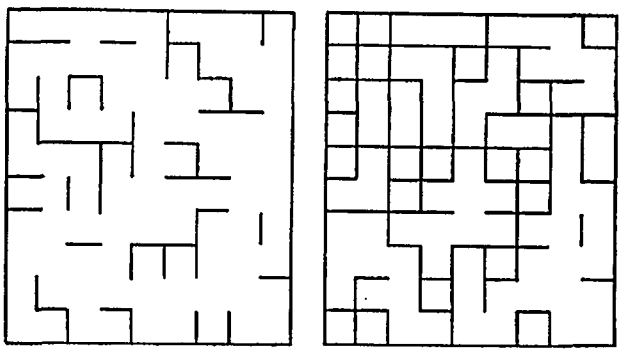

Figure 2.4.4 Bond percolation on the square network at bond occupancies of p=1/3 and p=2/3. The value of the critical occupancy, p_c for the square network is *exactly* 0.5, marking the formation of a spanning network (after *Sahimi,* 1995).

2.4.10 Correlation Length

Selyakov and Kadet (1996) proposed a model of the infinite cluster in which it was possible to represent the conducting skeleton or backbone of the cluster by means of a scaling law of the form

$$\xi \propto |p - p_c|^{-\upsilon}, \qquad (2.4.10.1)$$

where υ is a scaling exponent and the quantity ξ is known as the *connectivity* (or *correlation*) *length.* The correlation length represents the average distance between two sites in a cluster near the percolation threshold in a d-dimensional system.

2.4.11 The Critical Exponents in Transport Phenomena

For finite lattices, the percolation threshold depends on the specific realisation of the conducting bond distribution. However, in the limit of the lattice becoming infinite, the fluctuation of the percolation threshold vanishes, and this value converges exactly to what would be predicted by percolation theory. In an infinite system this threshold value is dependent only on the network type and the dimensionality of the problem, but remains independent of the specific realisation of the system. The formation of an infinite conducting (spanning) cluster is effectively a second-order phase transition and bears analogy with second order phase changes in amorphous semiconductors, as well as

in ferromagnets near the Curie point. Phase changes are generally characterised by a set of universal critical exponents that are tied to the dimensionality of the system. These parameters serve to quantify the behaviour of the system about its critical point, that is the rate at which a physical quantity diverges as the percolation threshold of the system is approached.

A variety of appropriate critical exponents exist, some of these being defined by *Stanley* (1971) and *Straley* (1980). A relationship proposed by *de Gennes* (1976) gives an exponent t as a linear combination of the dimensionality of the system, d, a correlation length, ζ, and the critical parameter, υ:

$$t = (d-2)\,\upsilon + \zeta, \tag{2.4.11.1}$$

The *Shklovsky-de Gennes* model of conductance (*Selyakov and Kadet*, 1996) allows us to relate the dimensionality of the system to the exponent υ, to give an approximation of the bulk conductivity of a cluster, Σ, in dimension d as

$$\Sigma \sim N\sigma_1 \approx \sigma_0 (p - p_c)^{(d-1)\upsilon}, \tag{2.4.11.2}$$

where σ_1 is the specific conductivity of a chain and σ_0 is the specific conductivity of the network when $p = 1$. Alternatively, the bulk conductivity has been found to scale with the exponent t, so that

$$\Sigma \approx |p - p_c|^t. \tag{2.4.11.3}$$

The exponent t has been found to be largely universal, where $t(d=2)\sim1.3$ and $t(d=3)\sim1.7$ (*Normand et al.*, 1988; *Gingold and Lobb*, 1990); the permeability k of a fluid in a hypothetical pore network scales in an identical fashion according with the critical exponent t (*Berkowitz and Ewing*, 1998):

$$k \approx |p - p_c|^t. \tag{2.4.11.4}$$

2.4.12 Effective Medium Theory and PSRG Procedures

The effective-medium theory, on account of its reliance on a probability density function of network conductances, is expected to be more accurate when the conducting network is not sparse, that is, when the correlation between the discrete conductances is carried out over a relatively large population of occupied sites. Outside the critical

region, one can obtain a conductance with some reliability from an effective medium treatment. *Koplik* (1982) showed that effective-medium representations of heterogeneous materials are successful for uniform distributions, but not for networks fitted by broad lognormal distribution functions.

As a consequence of the unreliability of the effective-medium approximation near the percolation threshold, a renormalisation procedure was developed by *Sahimi et al.* (1983) based on the combination of the effective-medium approximation and Position-Space Renormalisation Group (PSRG) procedures. This has been reviewed by *Zhang and Seaton* (1992) in a study of effective diffusivities in porous solids with continuous pore size distributions. In PSRG theory (*Stinchcombe and Watson,* 1976), the original network is divided into identical unit cells with linear dimension b. Figure 2.4.5 shows the renormalisation procedure for the isotropic cubic lattice when $b = 2$. The renormalisation procedure involves replacing the original unit cell by three renormalised bonds, where the conductance distribution of the renormalised bonds is chosen such that they offer the same resistance to transport as the original cell. Thus, a new cell, topologically equivalent to the original, is created out of the renormalised bonds, but with linear dimension a factor of b larger. The fraction of unoccupied bonds changes on renormalisation, this fraction being denoted as $R(p)$. With each successive renormalisation, the conductance distribution becomes increasingly narrow. As the number of realisations approaches infinity, the fraction of unoccupied bonds moves to one of three fixed points:

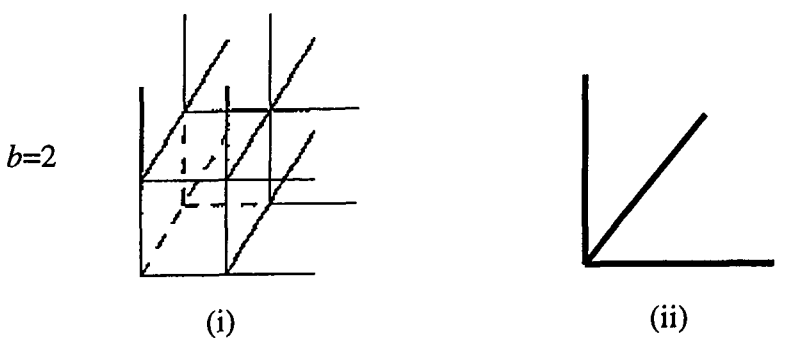

Figure 2.4.5 (i) b=2 Renormalisation cell for the simple cubic lattice; (ii) Renormalised bonds corresponding to this cell (after *Zhang and Seaton,* 1992).

- If the initial fraction of occupied bonds satisfies $p_c=R(p_c)$, the fraction of renormalised bonds does not change as a result of renormalisation, and hence p is a true estimate of the percolation threshold.
- If, however $p>p_c$, then the fraction of occupied bonds increases with each renormalisation step, and tends to unity.
- If $p<p_c$, the fraction of occupied bonds decreases with each renormalisation step. Thus, with each renormalisation the system moves further away from the percolation threshold.

Sahimi et al. (1983), in noting that a renormalised network lies further away from the percolation threshold than the original network, developed the Renormalised Effective Medium Approximation (REMA), where a single renormalisation approach is carried out and the renormalised conductance distribution $p'(g)$ is used as the input into Kirkpatrick's equation, (2.4.3.8). Furthermore, Sahimi applied REMA to a binary conductance distribution on the square and simple cubic lattices, and compared the results with the original EMA and also with the network Direct Solution (or DS) method. It was discovered that REMA was more accurate than EMA in the region of the percolation threshold and for the simple-cubic lattice. Estimates of p_c for the EMA and REMA methods could be compared directly to the DS method as follows:

$$p_c(\text{EMA}) = 1/3 > p_c(\text{REMA}) = 0.2673 > p_c(\text{DS}) = 0.2493. \qquad (2.4.12.1)$$

The PSRG method yielded a bond fraction of 0.2083 at p_c, in accordance with the renormalisation procedure, moving the system further away from the percolation threshold, when $p<p_c$.

2.4.13 Percolation on Anisotropic Networks

Toledo et al. (1992) noted that the anisotropic effective-medium approximation should be useful whether the lattice anisotropy is intrinsic, or introduced by a lattice decoration process in which conductances of bonds aligned in different directions are drawn from different probability density functions. In the latter case, the geometrical variability of pore-segment characteristics is therefore approximated by distributing conductances to the bonds of the representative network according to *directionally dependent* probability density functions. The work of *Friedman and Seaton* (1998b)

also included a consideration of connectivity-induced anisotropy. This was introduced into their network models by the application of a directionally-dependent bond deletion routine to the isotropic cubic lattice which was then subsequently "decorated" with bonds from a set of directionally-dependent pore radius distributions.

The first research into percolation anisotropy was made by *Shklovskii* (1978), who quantified the conductivity anisotropy of a network by

$$A = \frac{g_l}{g_t} - 1. \tag{2.4.13.1}$$

The quantities g_l and g_t are the macroscopic conductivities of the network, parallel and perpendicular to the direction of the macroscopic potential gradient, respectively. Near the percolation threshold, the anisotropy factor begins to follow a scaling law of the form

$$A \sim (p - p_c)^{\lambda}, \tag{2.4.13.2}$$

where λ is the critical exponent for the anisotropic system. *Mukhopadhyay and Sahimi* (1994) discovered that $\lambda_2 > \lambda_3$, which shows that the anisotropy in a two-dimensional network vanishes faster than in the three-dimensional case. This may be understood by considering the structure of the subcritical network; *Sarychev and Vinogradoff* (1983) reasoned that the conducting backbone consists of a skeleton together with dead ends, the latter being less dense in the three dimensional case, thereby giving $\lambda_2 > \lambda_3$. However, it is not yet known how to relate λ to the structure of these dead ends, and so it is difficult to build up a quantitative verification of this postulate. The fact that A disappears at the threshold is due to the tortuous nature of the conductance pathways. In close proximity to p_c, the tortuosity becomes so large that the directional aspects of the flow channels become indistinct, and the anisotropy vanishes. This phenomenon allows us to explain why the critical exponent λ_d is greater in two than in three dimensions, since this may be interpreted as suggesting that as we approach the percolation threshold, the tortuosity of the three-dimensional paths will similarly increase at slower rates than the two–dimensional counterpart. Consequently, the anisotropy should indeed vanish faster in the case of the two–dimensional network.

Much effort has been given to the estimation of percolation thresholds of infinite isotropic simple cubic lattices using scaling theories (*Gingold and Lobb,* 1990).

However, the percolation threshold in a given direction will depend on the occupation (co-ordination) number in that direction. For two-dimensional lattices, there exists an exact solution to the percolation problem (*Sykes and Essam,* 1963), that is consistent with other approaches, such as the expansion method of *Redner and Stanley* (1979), and also with other related Monte Carlo Renormalisation Group methods (*Kim and Lee,* 1992). In a further study by *Friedman and Seaton* (1998c), the percolation thresholds of three-dimensional cubic lattices was employed. This was achieved by a repetition of their directionally-dependent bond deletion routine until a critical network was obtained. They addressed the likely trend of the anisotropy ratio as the critical bond occupation probability was approached, employing an isotropic bond decorating procedure together with an anisotropic bond deletion routine, using reasoning similar to *Shklovskii* (1978).

Friedman and Seaton (1998c) have extended their work to calculating percolation thresholds on the infinite cubic lattice, employing the extended finite-size scaling equation of *Wilke* (1983). Related to this work is the algorithm SYMMLQ (*Friedman and Seaton,* 1998a,c) for calculation of the network conductance. The use of this algorithm requires relatively large lattices in order to eliminate the effect of the finite size of the system. In addition, many repetitions of the calculation for the differing random assignments of bond deletion are needed to get accurate values for the threshold porosity and conductivity.

3 ROCK SAMPLES

3.1 Introduction

This study involved two independent data sets. The first consisted of a collection of backscattered electron micrographs that were prepared from the core extractions of a commercial well that lies inside the UK Continental Shelf (UKCS), and was supplied by Enterprise Oil.

It was thought to be worthwhile to incorporate a second, independent dataset into the study. The second dataset was prepared by coring a sample of St. Bees sandstone for laboratory permeability measurements, the end trims been taken to prepare a collection of backscattered electron micrographs. The St. Bees sample was provided by Core Magnetics as an outcrop cutting from the Birkham quarry in Cumbria, UK.

3.2 UKCS Data Used in This Study

A geological description of the UKCS sandstone has been provided by *Hatfield* (1999), who suggests the following petrology. The samples are mostly fine grained, ranging from a very fine to medium granularity with moderate to poor sorting. Furthermore, the samples exhibit similar grain contact and roundness characteristics throughout. The main detrital components are monocrystalline quartz (24-62%) and feldspar (2-16%). It has also been noted that the feldspars have suffered from dissolution processes to form secondary porosity. Lithic fragments are also present (26%) and are composed mainly of polycrystalline quartz, minor amounts of chert and sandstone. Metamorphic granitic and volcanic rock fragments are also present. The principle diagenetic minerals are the clays kaolinite (0-9%), and chlorite (identified by Scanning Electron Microscopy (SEM) and X-Ray Diffraction (XRD). Quartz overgrowths (0-12%), ferron calcite (0-42%) and siderite (0-28%) are also present. The cementation has developed preferentially in thin bedded sandstone facies that are associated with mudstones.

3.3 ENTERPRISE Method of Data Acquisition

In practice, a core, approximately 4 inches in diameter, is taken parallel to the bedding plane in the course of drilling. A rectangular section of material, is then taken, parallel to the bedding laminations and a set of cubes are then cut from this slab, their

orientation carefully registered and retained with respect to the core. These cubes are utilised in pore magnetic susceptibility measurements using the MAGPORE method of *Hailwood and Bowen* (1999) to establish the mean pore orientation. To obtain the directional permeabilities however, a final section is then taken from the remainder of the core and from this material, a single cube approximately two inches across cut parallel with the bedding plane. The remaining end trims carefully marked to retain correspondence with the orientation of this cube. Permeabilities are obtained directly from measurements across the faces of the cube to give two measurements parallel with, and one measurement normal to the bedding planes of the formation. Each pair of end trims from any two opposing faces of the cube therefore represent one of three orthogonal slices, two lying parallel, and one perpendicular to the bedding plane in the reservoir. This set of end trims, registered with respect to the faces of the cube, are then mounted and polished for SEM analysis.

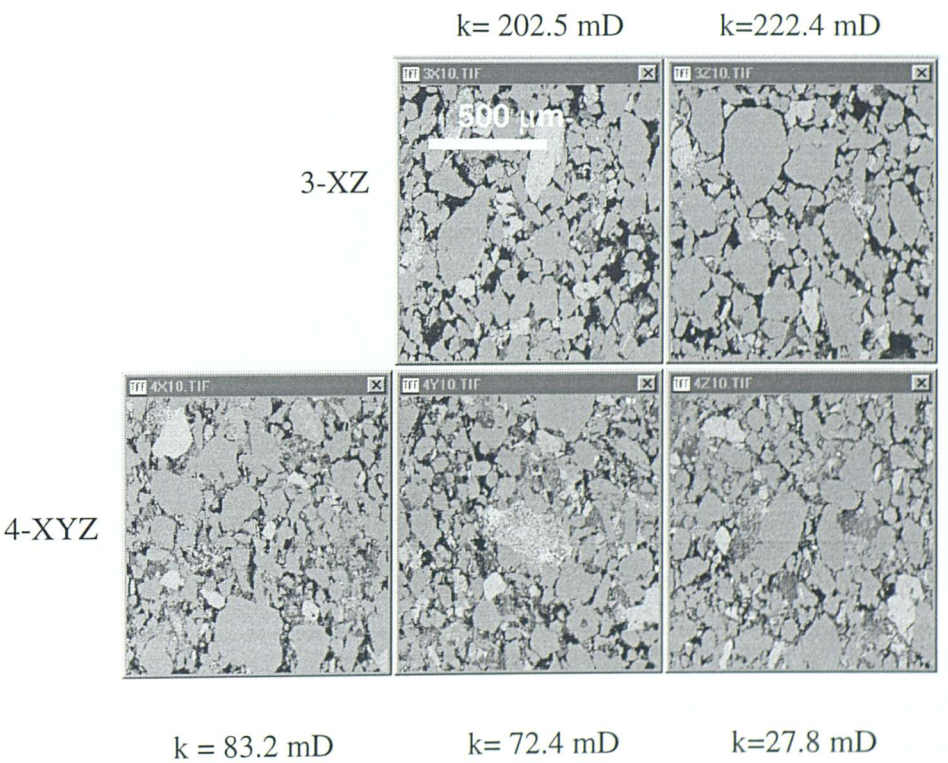

Figure 3.3.1 Examples of Backscattered Electron micrographs (BSEIs), taken from Well "A", along with their directed core measurements at X30. The notation gives a core identifier and thin section number, where the "X, Y, Z", tagging refers to the direction that lies perpendicular to the slice of the thin section.

The Backscattered Electron micrographs used were originally acquired by Applied Reservoir Technologies Ltd, and supplied for each core as a set of images taken in a five-spot configuration over the area of each of the mounted end trims, at a magnification of X30. Each image contains 512x400 pixels with a vertical to horizontal aspect ratio of 0.78125. As each pixel occupies an area of approximately 37 μm^2, the total field of view is 7.5 mm^2.

3.4 St. Bees Sample

St. Bees is a lower Triassic bunter sandstone from an Aeolian desert shoreline, and is transversely isotropic. The grains are subrounded with poor sphericity, and do not exceed 0.5 mm across. There is a low mica content and the sandstone is also considered to be texturally and mineralogically mature. *Al-Harthy* (1999) gives the porosity of St. Bees as 26%, and estimates the quartz content at 90% and the feldspar content at 5%.

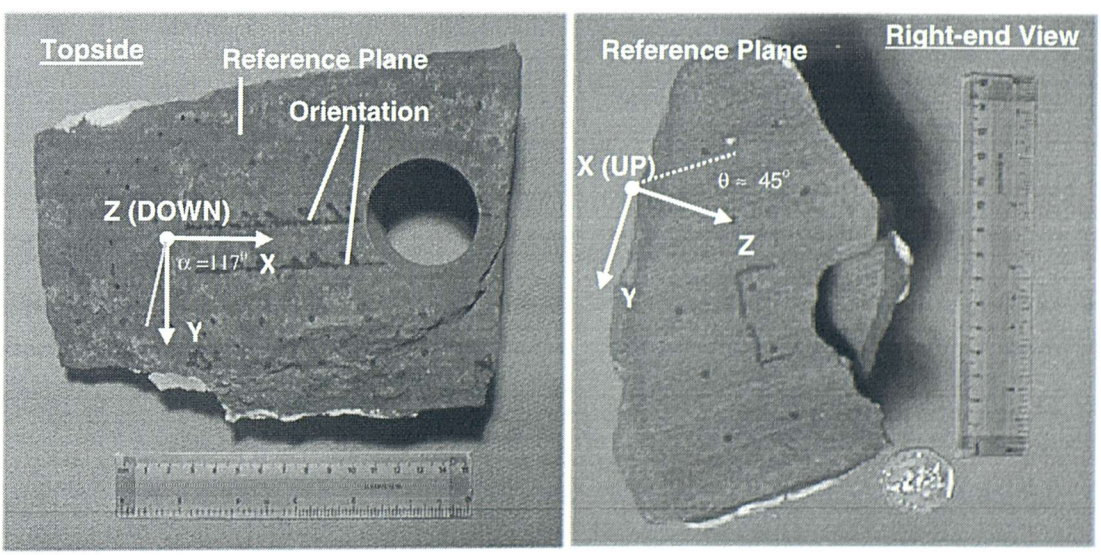

Figure 3.4.1 A diagram of the topside and the right hand view of the St. Bees sample together with the "**XYZ**" field co-ordinates. The mean pore long axis alignment as derived from the MAGPORE method is 117° clockwise from the **X**-axis. Close examination of the second figure shows the presence of cross-bedding; however, the angle between the **Z** field co-ordinate and the major bedding plane is approximately 45°.

The sample forms part of a larger cutting from the outcrop where magnetic measurements of pore fabric have been made, using bold notation, in "**XYZ**" field co-ordinates, referred to the reference plane as shown in Figure 3.4.1. Orientation axes

have been drawn along the sample *in situ* before its detachment from the outcrop; the orientation of this plane relative to the horizontal, and of the orientation line relative to North, has also been recorded.

3.5 Heterogeneity Mapping

An assessment of the spatial variation in the local permeability of the sample was made using minipermeametry. A transparent grid containing regularly spaced points on a square lattice was overlaid on each face of the sample, and these points were then marked at regular intervals as possible onto the surface of the sample. The minipermeameter was then applied to each of these points, and a flow rate Q them measured in $cm^3\ s^{-1}$. The permeability is calculated from this flow rate in milliDarcies using

$$k = \beta Q, \tag{3.5.1}$$

where β = 467.6 mD s^{-1} is a composite constant that includes the factors of the differential gas pressure, cross-sectional area and gas viscosity, and allows the permeability to be calculated directly in milliDarcies from the injection rate and pressure differential across the probe tip. Some points have been deliberately omitted where the flow measurement is thought to be particularly unreliable, either due to surface irregularities preventing a good seal at the injection point, or because the sample becomes too thin and the support volume is not sufficiently large to allow boundary effects to remain negligible.

Table 3.5.1 A compilation of the minipermeametry statistics for the St. Bees sample.

Parameter	Topside	Bottomside	Leftside	Rightside	Frontside	Rearside
n	31	21	2	3	2	6
$\langle k \rangle$	83	208	234	284	175	119
σ_{n-1} (mD)	67	116	126	56	17	46
σ_{n-1} (%)	80	56	54	20	9	39

The following pictures show the local permeabilities, expressed in mD, for the six faces of the sample.

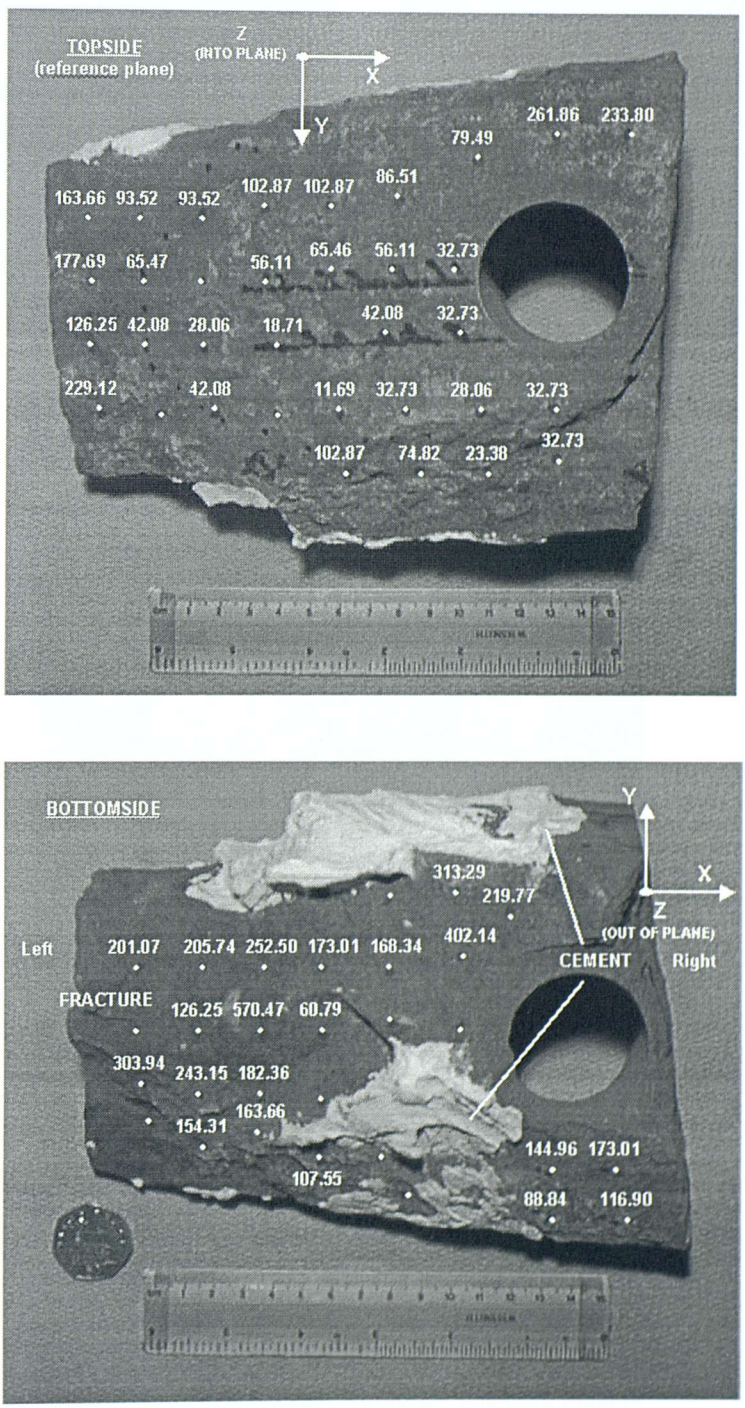

Figure 3.5.1 Topside and the corresponding bottomside of the St. Bees sandstone, showing the permeability mapped at designated points.

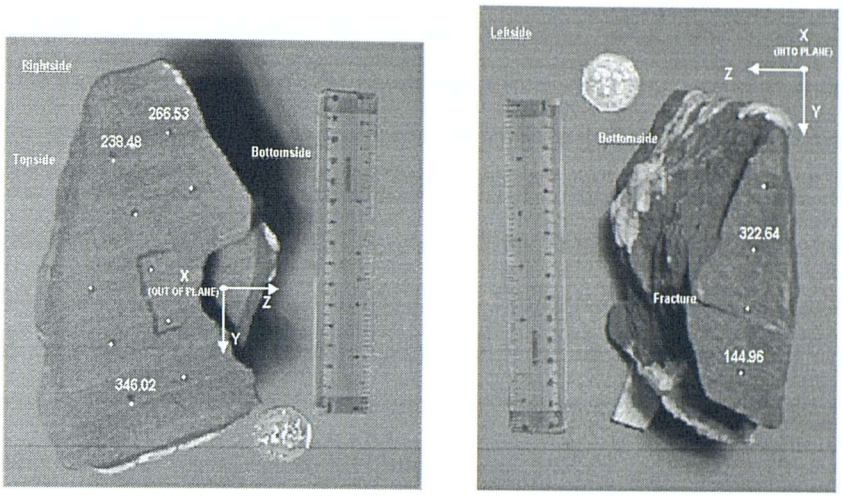

Figure 3.5.2 Left and right-hand sections of the St. Bees sandstone showing the relative orientation of the reference axes as the sample is rotated.

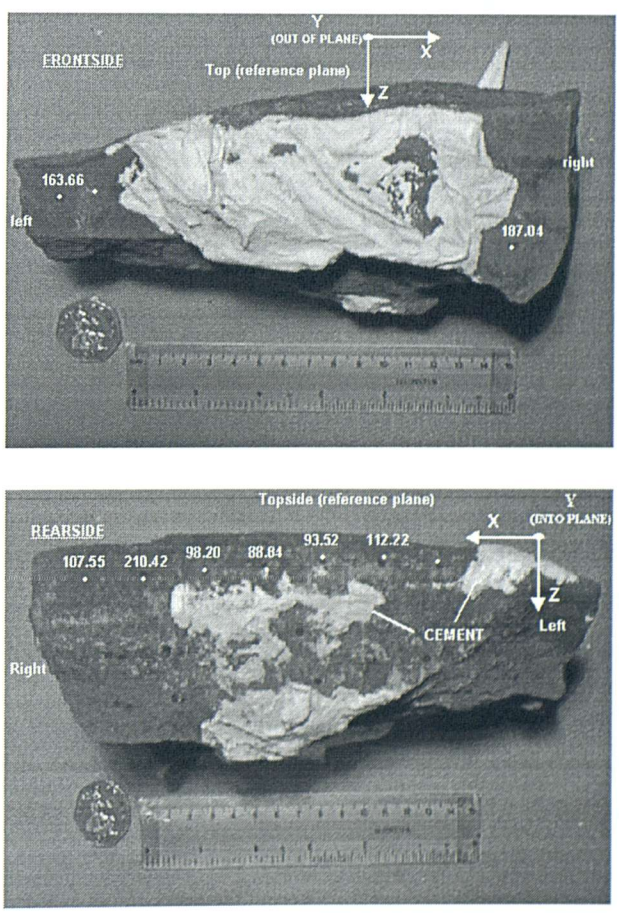

Figure 3.5.3 The final set of permeability measurements for the front and rear sides of the St. Bees sample again relative to the reference axes.

An examination of the statistics for the left and right faces, that is, along the **X** axis, shows that the average permeabilities are comparable. It should be noted, however, that the relatively low number of measurements may make this result somewhat fortuitous. Similarly, the sparseness of data makes it difficult to draw any conclusion for the standard deviations calculated for the permeabilities from the left and right faces of the sample. The results also indicate an increase in the average permeability by a factor of 2.5 as the **Z** axis is traversed from the reference plane to the bottomside of the sample, but in addition, the standard deviation increases by over 20% indicating a moderate degree of heterogeneity along the **Z** direction.

The differences in the average pemeability between the front and back faces are not significant, although the standard deviations calculated for each face vary by nearly a factor of four. However, such differences may be attributable to a lack of sampling rather than being indicative of spatial variations in lithology.

The overall permeability parallel to the bedding plane, taken along the **X** axis (*i.e.*, parallel with the left and right side faces), is slightly higher than the other collections of measurements which have been taken at some other orientation relative to the bedding plane. Unfortunately, however, the heterogeneity, although producing permeability variations that remain within an order of magnitude, makes it difficult to judge if this difference is indeed attributable to lithological anisotropy, or is simply an artefact of spatial variation in the collected permeabilities.

3.6 Coring Details

A first cylindrical core approximately 2.5 cm in diameter was cut from the sample at a right angle to the major bedding plane, and denoted as "Z", using nonbold notation. Magnetic susceptibility measurements showed the mean pore long axis to be aligned at 117° degrees clockwise to the orientation arrows. To cut the second cylindrical plug, this axis was projected onto the bedding plane, and then a second core was cut into the bedding parallel to this projection and denoted as "X". Finally, a third core was removed from the sample, within the bedding plane, orthogonal, but at a clockwise orientation to the X core so as to obtain a right-handed set of plugs. The final core was labelled "Y" and similarly lies at 117° clockwise from the parent **Y** axis in the reference plane. The endtrims of the three cores were removed, and their registration with the remaining cylinders recorded. Both the endtrims and the cylinders were continuously

extracted in ANALAR grade methanol for 48 hours, and then allowed to dry for 24 hours under a partial vacuum at 200°C. The endtrims were then imbibed with epoxy resin and mounted as thin sections approximately 3.8 cm^2 in area for scanning electron microscopy analysis. A total of seven endtrims were collected from the three orientated core plugs. The remaining cylinders, 5 cm in length, were then further cleaned to remove the fines from the end faces. This was achieved by sonication in ANALAR grade methanol for eight hours, replacing the methanol every two hours. The cores were subsequently dried under the same conditions detailed above. The final cylindrical plugs were then taken and used in Klinkenberg-corrected gas-permeability measurements.

3.7 Klinkenberg Measurements

Gas flow measurements were performed on an Ergotech fast-loading Hassler cell permeameter at a confining pressure of 300 psi ($\approx$ 20 atm), using nitrogen as the carrier gas. At least twenty measurements of flow rate were recorded for each of the three plugs with upstream pressures ranging from 1.2 to 3.0 atm. The downstream pressure was maintained as approximately 1 atm.

The calculated permeabilities were plotted against the inverse of mean flow pressure and extrapolated to infinite mean pressure using the equation (*Scheidegger*, 1963)

$$k_{gas} = k_{\infty}\left(1+\frac{b}{P_m}\right), \tag{3.7.1}$$

where k_{gas} is the gas permeability, calculated from Darcy's law, P_m is the mean pressure across the length of the plug at which the measurement is made, b is the Klinkenberg coefficent, and k_{∞} is the equivalent liquid permeability. The the results are summarised in Table 3.2.2, and the Klinkenberg plots are shown in Figure 3.7.1.

Table 3.2.2 Compilation of data for the three cores from the St. Bees sample.

CORE	k_{∞} (mD)	b (atm^{-1})	R^2
X	648	0.1520	0.8308
Y	1380	0.1519	0.8479
Z	1050	0.1950	0.8690

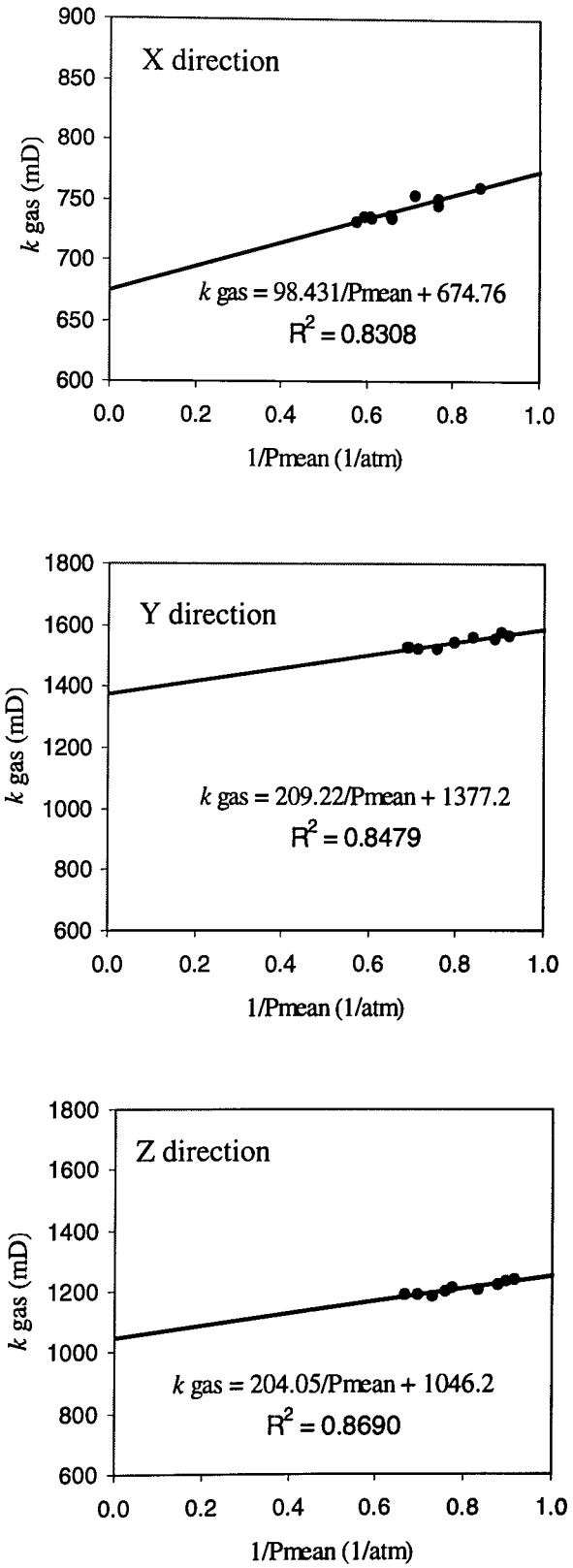

Figure 3.7.1 Klinkenberg plots obtained for the directed cores X, Y and Z.

Somewhat suprising is the permeability of the X core, which although cut parallel to the major bedding and, more significantly, aligned with the mean pore long axis (as assumed from MAGPORE measurements), exhibits a lower permeability than the Z core, which was cut perpendicular to this bedding. The ordering of the permeabilities as derived from a Klinkenberg-corrected gas flow measurement is $k_X < k_Z < k_Y$, with an anisotropy ratio of 2:3:4. This is counterintuitive, as it might be expected that the permeability in the Z direction would be the lowest. However, there is strong visual evidence to support the fact that in fact the sample is cross-bedded. Although the presence of heterogeneities and other lithological factors such as cross-bedding will influence the magnetic response of a sample, the ordering of the permeabilities suggests that the statistical alignment of the pores may not correlate that closely with the direction preferential for the flow of fluids. Consequently, this brings the MAGPORE method of determining the principal directions of permeability using mean magnetic susceptibility measurements of the pores into question, and raises the issue of whether or not the orientation of the cores had been correctly chosen to provide the components corresponding to the diagonalised permeability tensor.

3.8 SEM Details for St. Bees Sample

Five BSEI were collected for each endtrim in *.BMP format, again in the five-spot configuration, but at the slightly higher magnification of X35. The instrument used was a Jeol T200 scanning electron microscope equipped with a four quadrant semi-conductor backscattered detector, supplied by KE Instruments. The microscope was run at an accelerating voltage of 25 KeV.

The stored images were resized to a common format of 650x500 pixels. The horizontal scalebar integral to each image was 205 pixels across, corresponding to 1000 microns. Each image was then cropped to 649x450 pixels to remove the integral scalebar and other extraneous information. The final images, stored in uncompressed *.TIF format, were composed of pixels with an aspect ratio of 0.27 and an area of 88.83 μm^2. The total field of view of each stored BSEI is then approximately 26 mm^2.

4 IMAGE ANALYSIS

4.1 Introduction

The purpose of using image analysis is to obtain faithful representations of the pore space, and therefore an estimate of the relevant pore space parameters. In this study, the aim is to reproduce the permeability of anisotropic rocks by collecting area and perimeter measurements, within imaging resolution constraints, to form the set hydraulic conductances corresponding to the pores in the image. This data is then input into an effective-medium network model that will predict permeability.

Image analysis may be regarded as a technique for characterising and classifying images, and features within images, when a corresponding core analysis on a 3D sample is unfeasible. In the context of estimating the permeability of a reservoir rock, this situation may arise in field development scenarios where insufficient material is available for routine core analysis.

The procedure of obtaining tractable information from thin sections will typically involve the use of a microscope, together with a video scanner or camera, a digital converter and image processing software. The successful analysis of data requires the development of consistent image processing methods with which regions of interest can be identified and segmented from the rest of the image. The following sections discuss these procedures in more detail.

4.2 Electron Microscopy

Representative images of thin sections are obtained by some form of optical or electron microscopy. In the present study, scanning electron microscopy is used, in which a scanning electron beam then replaces the incident light beam, affording greater resolution than other optical methods. An operational difficulty arises because electrons would be scattered by air, and so the beam path must operate in a vacuum. In scanning electron microscopy the beam sweeps the surface of the sample synchronised to the output from a cathode ray tube. Backscattered electrons from below the surface of the specimen modulate the intensity of the beam from the cathode ray tube. The interactions which occur between incident electrons and target atoms may be divided into elastic and inelastic processes. In the former case the collision between the electron and the relatively massive nuclei results in virtually no momentum transfer; this is because the

nuclear energy levels are widely spaced (MeV) compared with the electron energies used in the analysis (~10 KeV), and so there is little possibility of energy exchange between the surface and the incident electron beam.

If the incident electrons are of a sufficiently high energy, interactions with the inner shell electrons of the specimen may take place, resulting in the release of X-rays, which can themselves be used as an analytic tool for elemental mapping (*Birks,* 1959; *Briggs and Seah,* 1983). Additional inelastic processes do occur, in which case the mechanism for collisional energy transfer becomes operative when the incident electrons interact with outer orbital electrons of comparable energy in the target (*Scott and Love,* 1983).

For mineralogical classification of reservoir rocks, the main aspects of the analysis are concerned with the detection of the elastic processes that occur at the target, since the emission intensity of the elastically scattered electrons is a function of the specimen's atomic number (*Petruk,* 1989). Thus, the brighter the signal the heavier the element, with the contrasts provided by differences in electron density within the specimen. Often these contrasts may not be sufficient to give a great enough difference in scattering power to allow different material domains to be distinguished and various techniques are employed to enhance this contrast during sample preparation (*Schlueter,* 1995). In the application of electron probe techniques for the examination of the pore space of a fluid-bearing porous medium, a 3D sample is subjected to vacuum and then a low-viscosity fluid epoxy resin is allowed to imbibe under at positive pressure, into all the interconnected pore space. The resin is then allowed to set under ambient pressure allowing its polymerisation into a material with a molecular mass that is small relative to the mineral phases present (*Ruzyla,* 1986; *Tsakiroglou and Payatakes,* 2000). The 3D specimen is then sliced into 2D sections of approximately 50 μm width, and mounted onto a sample holder. Finally, preparation of samples may involve polishing to eliminate shadowing effects, and the surface deposition of a thin conductive layer such as graphite to prevent charging of the surface by the scanning electron beam. This conductive layer masks surface features to some extent, limiting resolution to about 10 nm. However, the contrast between the molecular weights of the resin the mineral phases still makes the pore phase component of the thin section discernable. Alternatively, impregnation with a low-melting alloy such as Wood's metal may be used to enhance the difference in optical brightness (*Rink and Schopper,* 1978).

Computers are unable to process a continuous spectrum of grey values, and so the input image must be represented by a finite range of discrete values arranged as a matrix. Thus, the image is treated as a set of "points", each having a value corresponding to the average intensity of the image about that point. The image may be captured directly in digitised format, or may be kept initially as a photograph to be later scanned/digitised and stored in some conventional digital format such as a *.BMP or *.TIF image file.

4.3 An Overview of Image Processing Software

Once stored in a permanent digital format, the image can be accessed by use of a suitable image processing software that will allow the editing, enhancement and subsequent analysis of digital images. The software used in this study was the "Scion Image for Windows" package - Version: Image Beta1a 1997.

Scion Image is an image processing and analysis program for the IBM PC. It operates as a menu-driven interface that has the capacity to provide the conventional image processing operations such as smoothing, sharpening, edge detection, median filtering and two-dimension convolution with user-defined kernels. It also performs automated feature analysis and spatial calibration is supported to provide real-world area and length/perimeter measurements. Collected results may be printed or exported to a text file for further study.

4.4 Image Segmentation and the Grey-level Histogram

Segmentation is the assignment of a grey-level or energy threshold with which to convert the digitised image into a binary signal (*Joyce-Lobel,* 1985; *Castleman,* 1996). The term "thresholding" in this context then refers to the mapping of all "points", or pixels, with energy levels up to and including a certain predetermined threshold value to a binary output of zero, with all higher levels mapped to a binary output of 1. In the context of deriving fluid transport parameters, a threshold is sought that allows separation of the 2D representation of the pore space from the remainder of the mineral phases present in the 2D section. Consequently, the procedure of image analysis is performed only on this "meaningful" representation of the conducting phase of the porous material.

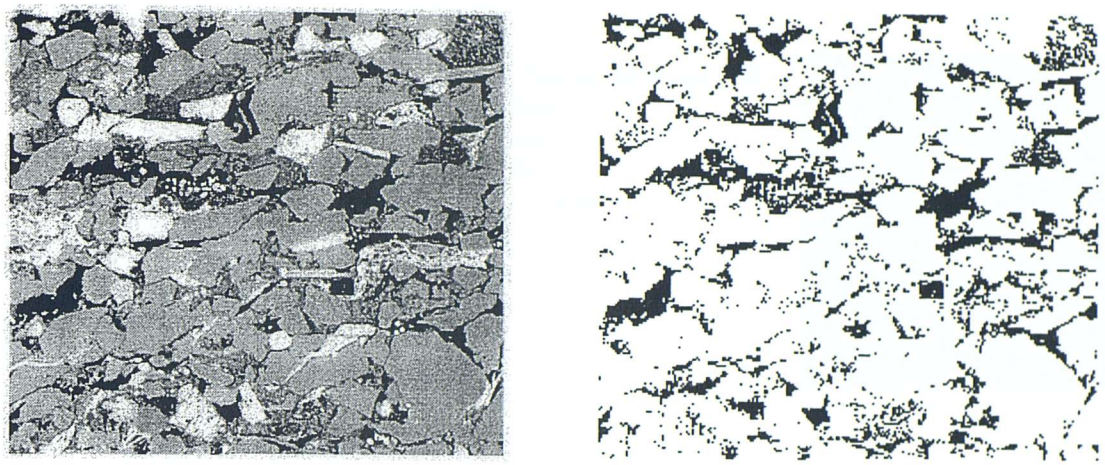

(a) (b)

Figure 4.4.1 (a) A digitised SEM image of a single representative thin section at X150. The dark regions represent the pore space and the remainder the grain area complete with mineralogical features (supplied by Enterprise Oil). (b) Binary representation of the image, with the pores distinguished as black and the remaining features mapped to a binary output of zero. The length of each image is 708.25 μm.

An important visual aid in the determination of correct image segmentation and thresholding comes from using the histogram window in conjunction with the corresponding image, and forms a very central part in much image analysis. The grey-level histogram is a display device which shows the number of pixels that are attributable to the various mineral phases present in the thin section, and therefore provides a visual summary of grey-level content of an image.

Figure 4.4.2 shows a typical histogram for this set of data, where the abscissa is grey-level (1-256), and the ordinate is frequency of occurrence. A complement to the Enterprise data set is a collection of the grey-level calibration standards supplied by Applied Reservoir Technologies Ltd, that is particular to the SEM instrument. These standards suggest limits to the regions of the grey-level histogram that are attributable to the minerals present in the sample. In field conditions, a service company may not always have access to the same SEM instrument. The criteria that have been developed to establish a set of mineralogical standards particular to a given microscope facility are not clear, and it may therefore be instructive to develop an individual set of segmentation criteria that remain uninfluenced by the operational characteristics of a particular SEM. On this basis, the present study does not rely on the suggested grey-level standards given in Figure 4.4.2 for image segmentation purposes.

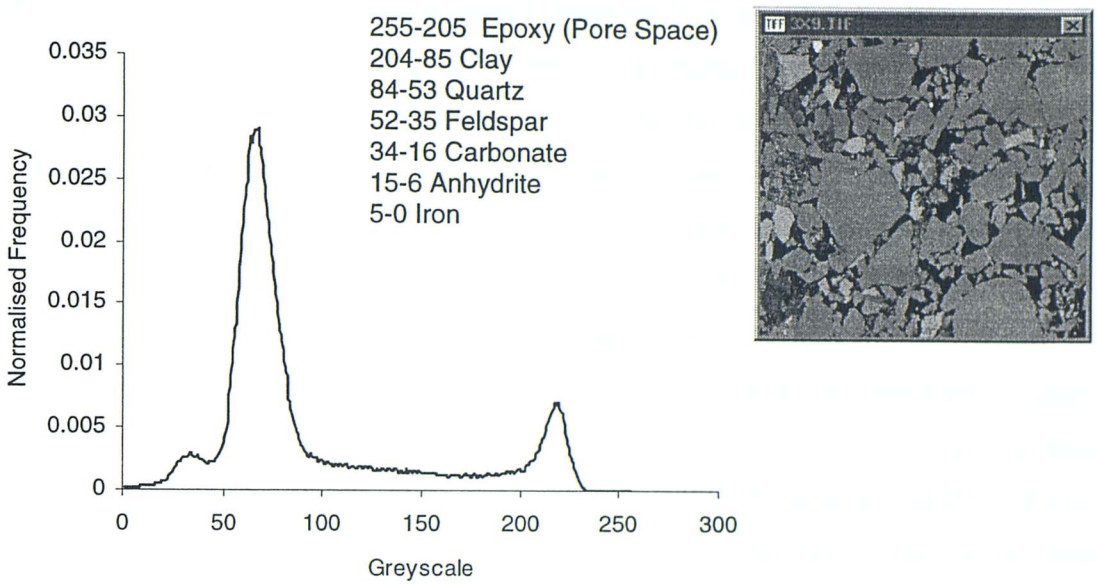

Figure 4.4.2 Illustration of a typical grey-level histogram for the Enterprise BSEI, complete with the complimentary set of suggested grey-level standards (courtesy of Applied Reservoir Technologies Ltd).

Ideally, for a given a set of mineral phases the grey-level histogram would be composed of a set of delta-type functions with heights proportional to the relative proportions of the phase in the field of view of the image. However, as the pixel size is finite, each pixel will not necessarily contain one mineral. This will have the effect of broadening the signals into Gaussian- or Lorenzian-type functions. In addition, there is an influence from the mineral grains not subtending the surface at right angles, so that the electrons do not reflect at the surface but at some small but finite depth. Thus, the energy of the reflection will already vary at the edges. Also, the surface is not flat, thereby creating additional dispersion. Depending on the degree of overlap between the broadened signals, it becomes increasingly difficult to ascertain the appropriate threshold for size measurements such as area, and also perimeter measurements, which are dependent on the location of feature boundaries. Image transform techniques that attempt to circumvent this problem operate by attenuating the grey-level gradients at the edges between neighbouring features. The overall effect of this operation is to change the energy distribution of the grey values in the image and thereby reduce the degree of overlap between adjacent peaks in the histogram (*Lu et al.*, 1994). Consequently, the

grey-level histogram allows a direct assessment of the impact of image transform procedures such as convolution on the energy distribution of grey-levels.

Weszka and Rosenfeld (1979) maintained that a reasonable methodology for choosing the threshold in a multimodal histogram is to locate the deepest point or valley between two overlapping Gaussian peaks. The idea behind this method is that in the vicinity of this dip, the histogram takes on relatively small values, implying that the area function changes slowly with threshold grey-level. Therefore, if we place the threshold grey-level at the dip, we minimise its effect on the boundary (*Castleman,* 1996), because of the relatively low number of pixels associated with these boundary features. Figure 4.4.3 below shows the response of the calculated porosity for three orthogonal thin sections to a range of thresholds where the histogram is not changing so rapidly. It can be seen that there is a plateau region, from 160-190 greyscale units, that corresponds with the local behavior of the area function of the histogram over the same region, where the change in calculated porosity is negligible.

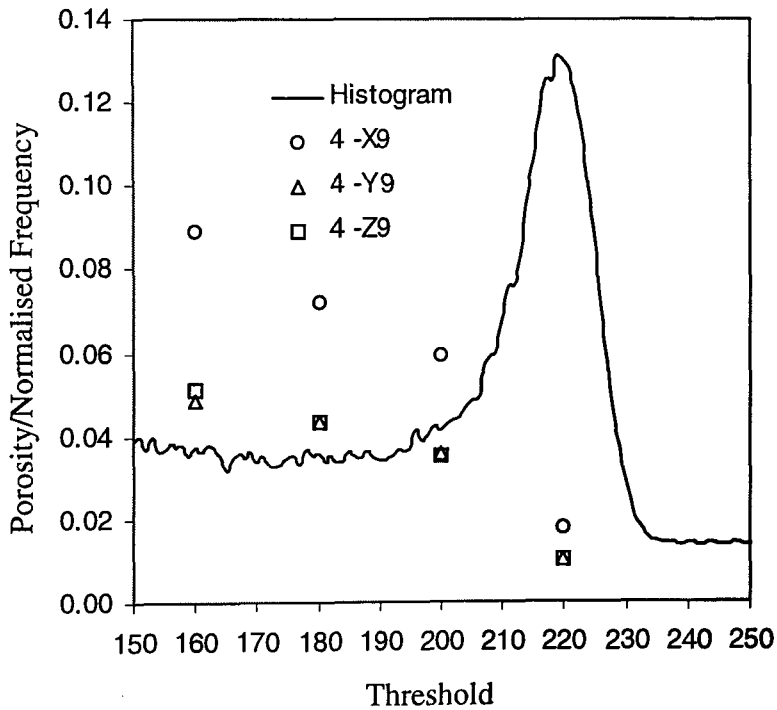

Figure 4.4.3 Illustration of the sensitivity of porosity to threshold selection for a set of three orthogonal BSE images of a North Sea Sandstone.

4.5 Global and Adaptive Approaches to Grey-level Thresholding

If the background grey-level is reasonably constant and the region(s) of interest has a consistent range of grey-levels, then the assignment of a threshold, applicable to the *whole* field of view of the image, may be applied. This method of segmentation is known as *global* thresholding, and was applied in the analysis of all BSEI used in this study.

Quite often, depending on the SEM response and the level of magnification, the illumination of the surface arising from the electron backscattering process may be nonuniform, so that the contrast of objects within the image varies from point to point, with the consequence of broadening the peaks in the histogram. Under these circumstances, the ideal approach is to use a threshold that correlates with the spatial variation of contrast across the image. The simplest implementation involves dividing the image into smaller segments and applying a *local* threshold that will discriminate between object(s) of interest and the local background. The approach, termed *adaptive* thresholding, then relies on a successful approach to treating the mean-grey-level in the neighbourhood of individual points in an image. *Weszka* (1978) reviewed the use of image processing techniques for establishing adaptive thresholding algorithims that would provide a consistent means of localised thresholding. From a practical point of view, however, the implementation of these methods in a commercial BSEI analysis may not be so straightforward, with each image requiring individual treatment, as the operational characteristics of the SEM may vary with running conditions.

4.6 Data Acquisition

4.6.1 Optical Calibration

This section is concerned with the process that allows the automated collection of the correspondent area and perimeter measurements. However, before any analysis can proceed, an assessment of the display characteristics of the software must be made, as this will dictate the reliability of the software to faithfully reproduce the energy distribution of the pixels that constitute the image and in turn, impart some effect to the segmentation or thresholding process.

An important display characteristic is the degree to which brightness of the display image remains in proportion to the input grey-level. We may test this using a grey-scale test target consisting of 256 squares ranging in grey-level from white (0) to black (255).

We can assess the linearity of this relation across the range of 256 grey-levels by examining the histogram of this test card. Noting that each square is identical in area, the pixels corresponding to a particular grey-level will contribute the same amount to the total optical density when the relationship is linear. The testcard in Figure 4.6.1 was created from PAINTSHOP PRO®, Version 4.10, by capturing its monochrome palette from the monitor display. This assessment therefore ensured the reliability of the software's pixel counting and greyscale identification, and introduces an initial robustness into the overall procedure of data gathering.

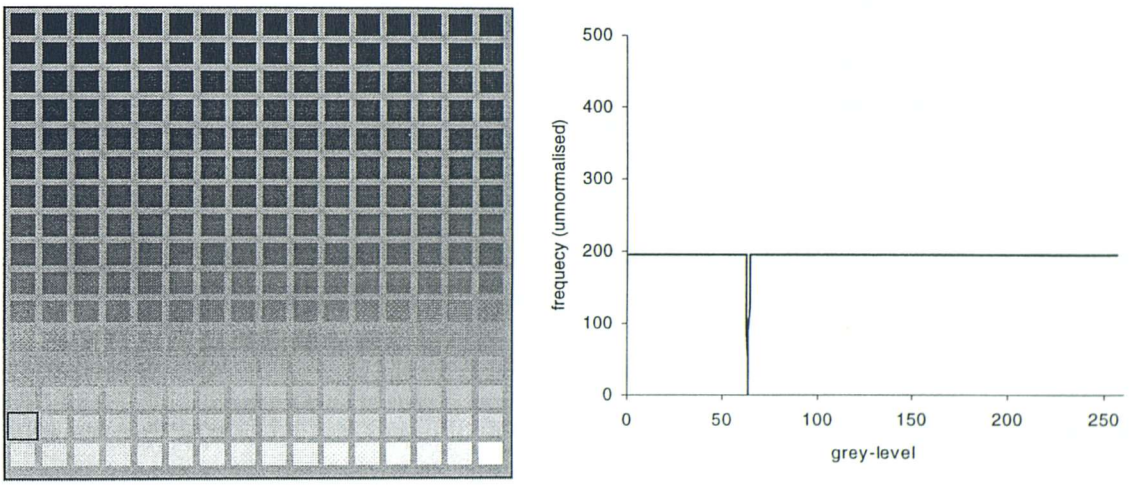

Figure 4.6.1 Illustration of the grey-level step card and the resulting grey-level histogram showing the linearity of the optical brightness with greyscale. The frame has a grey-level of 64 and was removed from the histogram; additionally, the histogram was truncated at 254 instead of 255 to exclude the contribution of the selection tool that resides permanently inside the palette. Note that each square contains 196 pixels.

4.6.2 Data Collection

The following protocol gives an outline of the stages involved in collecting the area and corresponding perimeter measurements commencing with image display and finishing with a final EXCEL file that is collected for subsequent calculation of the individual pore conductances.

1. Open image.

2. Go to Analysis menu and select "show histogram". This will display a plot showing the distribution of grey values within the selection. When the cursor is over the

histogram window, X (the grey value) and Y (the number of pixels with that grey value) are dynamically displayed in the information window (Figure 4.6.2).

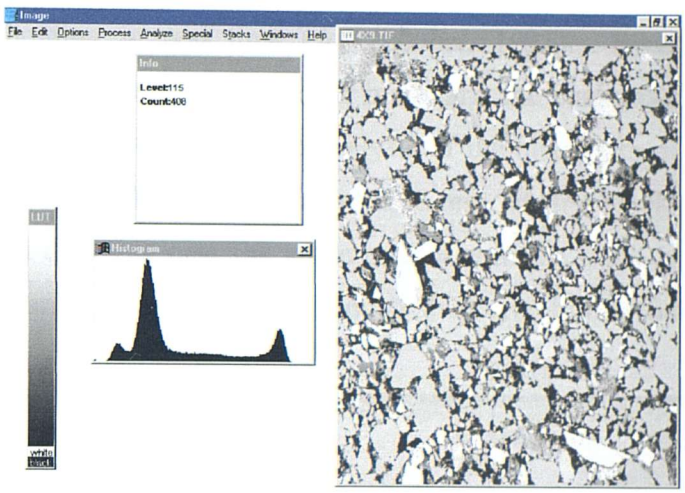

Figure 4.6.2 Scion desktop with BSEI 4-X9 opened in *.TIF format. Display contains Histogram Window, Information Window and Look Up Table (see step 5).

Both the histogram plot and the 256 data values can be copied to a Clipboard whenever the histogram window is active. The data values can also be saved to a text file using the Export command or into a graphics package such as EXCEL that is capable of permanently storing histogram information and the corresponding plots.

3. Set spatial calibration, including pixel aspect ratio.

4. Again, go to Analysis, then options and select "Area" and "Perimeter/Length". The maximum number of measurements should be allowed. The validity of these measurements in calculating the true dimensions of the pores was assessed by performing a feature analysis on images of regular shapes of known dimension. This was thought to be a necessary precaution as various image analysis programs may use some alternative definition of these parameters and so it is not always clear what is actually been measured. It was discovered however that the Scion program does return the true area and perimeters of these shapes.

5. Apply threshold/density slice using Weszka's methodology depending on the region of interest using the Look-Up Table. During the thresholding procedure, the digitised signal is altered in such a way that the grey-level of a given pixel is converted to a

binary value. Since their are 256 possible values for the input value it is quicker to recalculate a table of function results and look them up as each new pixel is considered, rather than to carry out the computation each time, consequently, the Look-Up Table can be used for thresholding in real time (*Joyce-Lobel,* 1985). When thresholding is enabled, the region of interest is displayed in black and the background in white. The threshold is automatically set based on an analysis of the histogram of the entire image current selection, or of a selection. To vary the threshold, the Look-Up Table tool is used by clicking and dragging near the white boundary in the Look-Up Table window. As the threshold is varied, its value is continuously displayed in the "Info" window.

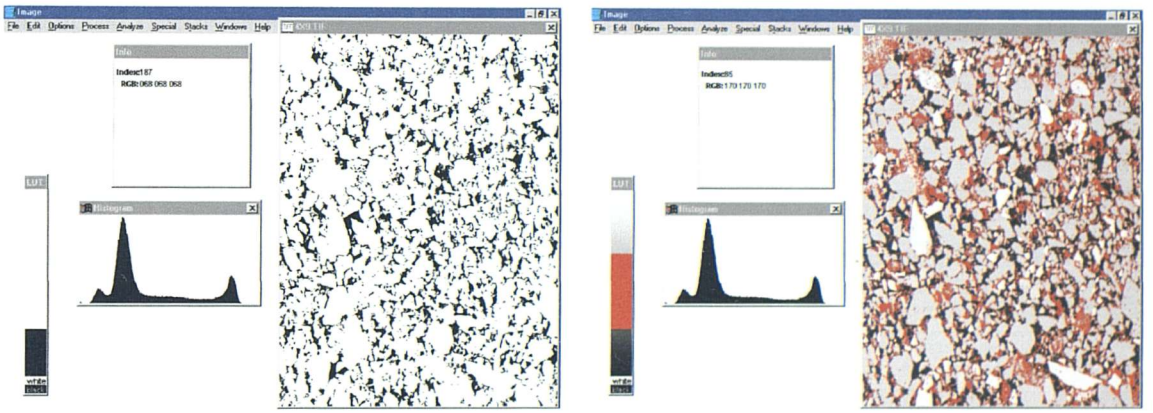

(a) (b)

Figure 4.6.3 Scion desktop with 4-X9 in (a) thresholding mode (T=187), and (b) during a density slice operation with lower and upper bounds of 85 and 180 greyscale units, respectively.

Density slicing was used on several occasions in this study, primarily to segregate the clay-type minerals form the rest of the mineral phases present in the 2D section (Figure 4.6.3), and like thresholding then allows objects that constitute the interior regions of the histogram to be segemented on the basis of grey-level. When Density slicing is enabled, objects are highlighted in red (for example) and background pixels are left unchanged. The upper and lower limits of the density slice as well as its location are varied by clicking and dragging in the Look-up Table window.

6. Return to the Analysis menu and go to analyse particles. Check only "Reset measurement counter", and Select "OK". At this stage the software visibly scans the

thresholded image and maps everything that falls *below* the selected threshold to a greyscale value of zero.

7. Go to options, and choose "Show results". This will display the collected area and perimeter measurements. Check "Export" from the "File" menu and export data into EXCEL.

8. Compute hydraulic radius and hence hydraulic conductivities of the individual pores.

4.7 Segmentation of the Clay Phase by Gaussian Deconvolution

The approximation of the histogram by least squares fitting routines has been previously attempted (*Chow and Kaneko,* 1972). According to *Otsu* (1979), this method involves laborious and unstable computations, and in many cases the peaks that emerge from these routines turn out to be insufficient approximations of the original histogram.

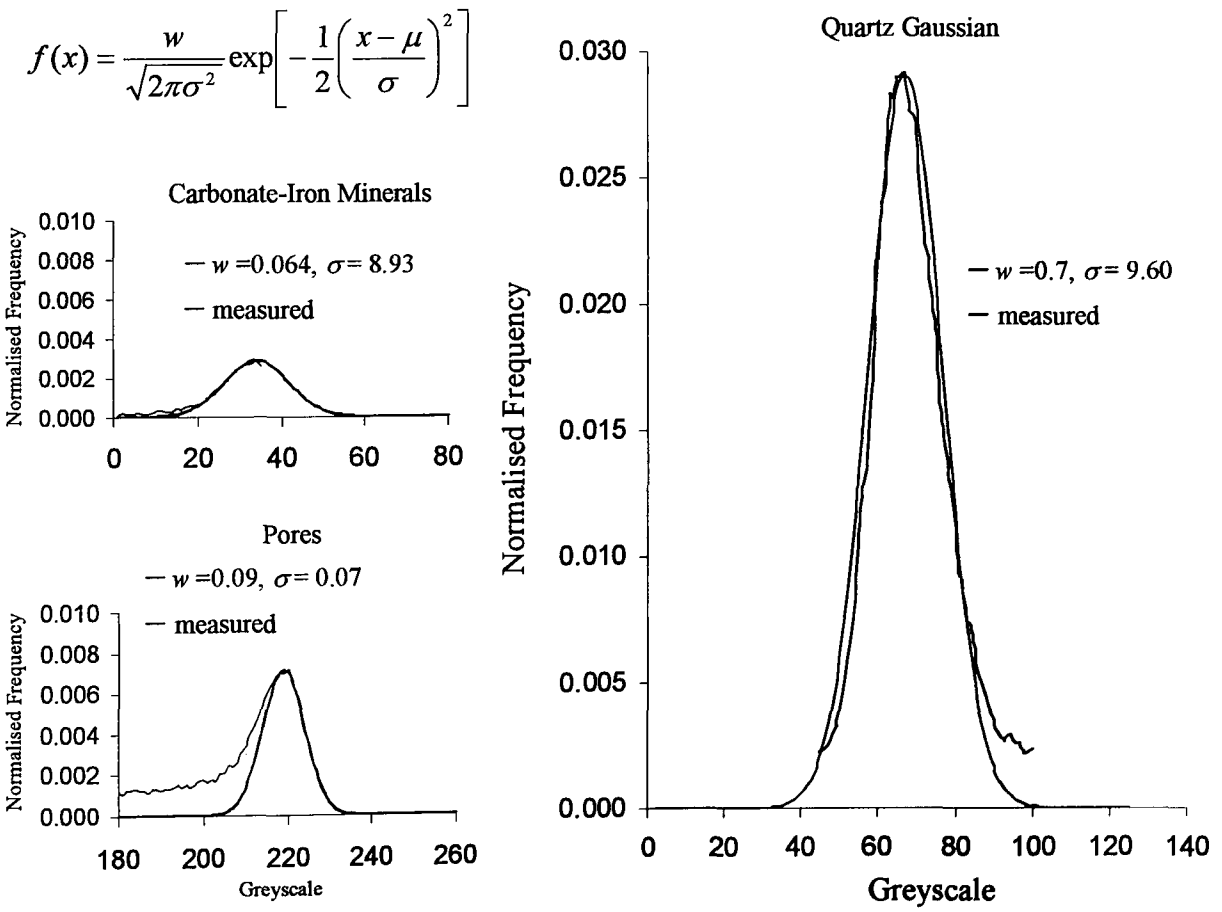

Figure 4.7.1 Illustration of the model fitting of the three chief Gaussians of Figure 4.4.2 using various weights, w, and variances, σ^2.

If the grey-level histogram is regarded as a sum of overlapping Gaussians, then an approximate form could be obtained by modelling the individual peaks separately and then adding them to obtain a representation of the original histogram. The procedure was successfully applied to the signals corresponding to the trace minerals, the major quartz peak and the pore-space (epoxy resin).

No reasonable Gaussian fit for the clay minerals in the intermediate region of the histogram was obtained, raising the question of whether or not this region is actually Gaussian in character. Consequently, if the reconstructed Gaussians are superimposed on the parent histogram, summed to obtain a merged signal and then subtracted from the parent, we are left with a region that can be can loosely identified as an area corresponding to the clay mineralogical standards defined by Applied Reservoir Technologies.

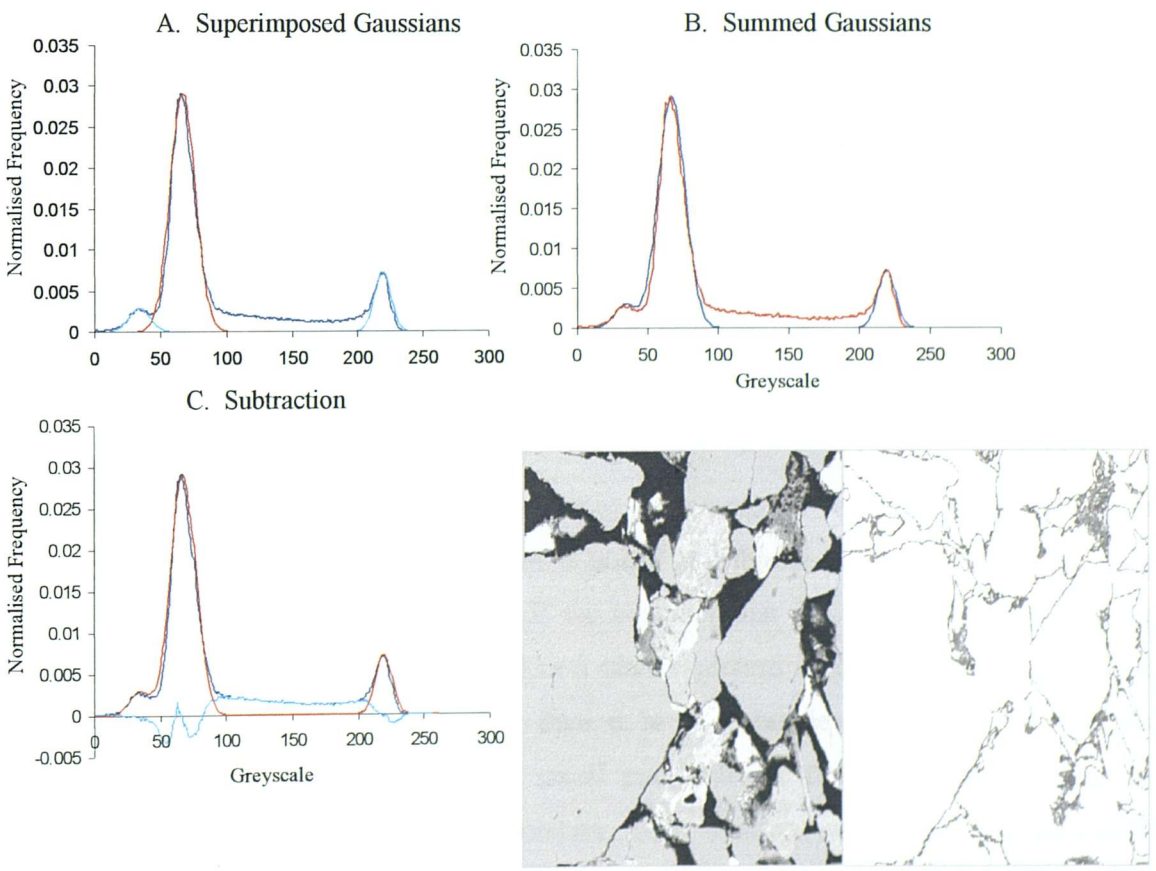

Figure 4.7.2 Superimposing the sum of the modelled Gaussians onto the original histogram and then subtracting gives an indication of the "non-Gaussian" elements of the grey-level distribution. A subsequent density slice between 100 and 200 greyscale units reveals the presence of tangentially-deposited pore perimeter lining illite and other

radial pore-lining clays that have developed in some regions into a pore-filling meshwork.

In studying Figure 4.7.2, it can be seen that there is a grey-level region between T = 100 and T = 200, that we could hopefully segment from the rest of the image by implementing the density slice tool mentioned in the last sections. Consequently, this would provide a spatial distribution of clays at the pore-scale and as such provide qualitative indications of their possible role in influencing permeability. For example, smectites and vermiculites are swelling clays that are widespread in soils and sedimentary rocks. The micropores of swelling clays are a major source of water in the earth's crust, and this will subsequently influence the formation, migration and trapping of natural gas and oil as a consequence of clay fluid interactions (*Skipper et al.,* 2000). Traditionally, this small void space has been associated with the clay content in the 2D section (*Basan, et al.*, 1997), but it may be construed that some proportion of this microporosity actually sits under the LH tail of the pore-space Gaussian in Figure 4.7.1, effectively rendering the clay and microporosity inseparable.

What remains intractable is a precise assignment of grey-level to the microporosity in the grey-level histogram. The present approach to threshold selection therefore remains inadequate in removing the microporosity component of the pore space Gaussian, since we cannot meaningfully allocate an absolute greyscale to this mineralogy.

4.8 Areal Thresholding and the Elimination of Microporosity

Despite the fact that microporosity may not be completely removed from the region of interest in the segmentation procedure, it is still possible to obtain a reliable estimate of the effective or transport porosity. If we consider that the procedure of collecting measurements from the pores observed in a planar section involves automated feature analysis over a wide range of scales, then it is conceivable that the measurements recorded for many of the single and small pixel cluster features corresponding to artefacts from the thresholding procedure will overlap with the microporosity component of the image. We can then define an additional thresholding procedure that eliminates these smaller non-conducting features, that sits on top of a visually determined greylevel threshold. If we then perform a "dual" thresholding procedure in this way, then we are effectively excluding the areal contribution of the small void space. The criterion used in our case was to choose an areal cutoff based on some

percentage of the area of the largest conducting feature, such that we do not lose more than 3% of the total hydraulic conductivity.

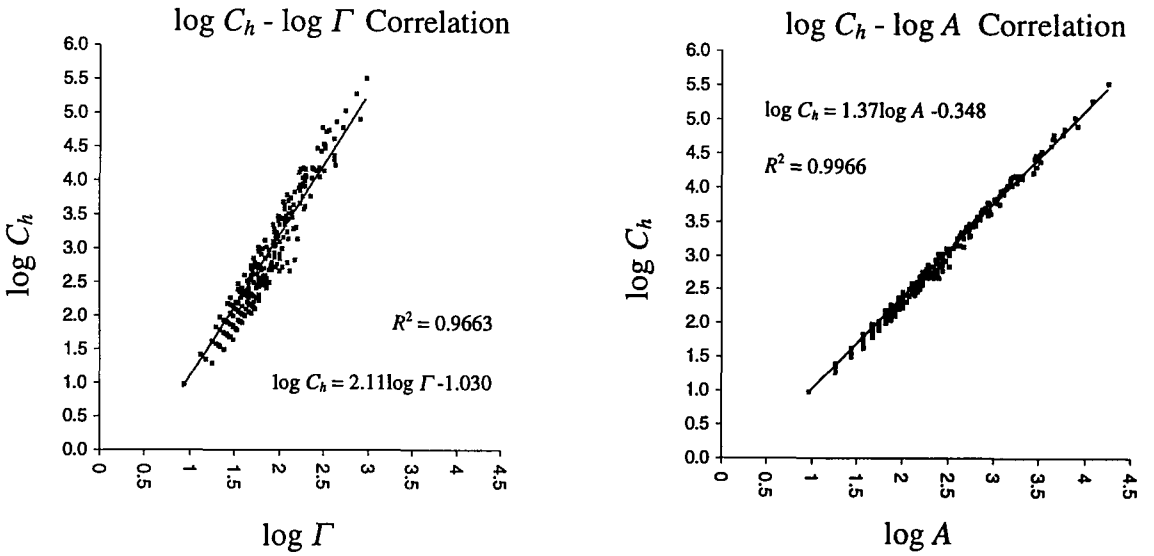

Figure 4.8.1 Log-log plots of hydraulic conductance against perimeter and area respectively.

Table 4.8.1 Compilation of the results obtained using a pixel based areal truncation for several North Sea sandstones.

Sample	Threshold	Area Largest Pore (μm^2)	1% Area Largest Pore (μm^2)	C_h (μm^4) Largest pore	% Cumulative C_h Lost
1 -X9	190	3006.44	30.64	158375.82	1.45
3 -X9	195	28695.80	286.96	2505401.59	1.69
4 -X9	190	9486.27	94.86	591410.16	0.60
A 64	190	17277.79	172.28	671.06	0.33

The justification for using an areal cutoff comes from the fact that the hydraulic radius correlates most strongly with area. Figure 4.8.1 shows how a linear regression analysis provides a comparitive indication of the strength of correlation of hydraulic conductance with perimeter and area respectively. The areal cutoff procedure was applied to BSEI originating from four different cores of various North Sea Sandstones. It was discovered

that removal of any feature whose area is less than 1% of the area of the largest feature accounts for the removal of not more than 3% of the total hydraulic conductance.

4.9 Influence of Pixel-Scale Roughness on Hydraulic Conductance

Berryman and Blair (1987) pointed out that use of too large a magnification would lead to the measurement of roughness on a scale too small to be of interest for laminar flow processes. For any method that uses the perimeter to estimate pore conductivity, such as the Kozeny-Carman method or the hydraulic radius approximation, Berryman and Blair proposed that the pixel size be approximately 1% of the size of an average pore radius. In our work, the magnification was X30, the pixel size approximately $6\,\mu m$, and the mean radius of those pores used in the UKCS study found to vary between 12 and 33 μm. The pixel length ranged from 3%-15% of the radii of the larger pores in our images, based on the calculation $r_p = \sqrt{A_p / \pi}$. The BEM calculations of *Sisavath et al.* (2000) however, have shown that in practice, pixel sizes up to 10% of the effective pore diameter can be used without noticeable influence on the computed hydraulic conductivities, suggesting that the criterion hypothesized by Berryman and Blair may be too conservative for our purposes.

4.10 Influence of Grey-level Thesholding on Hydraulic Conductance

A plot of the variation in areal porosity with grey-level threshold was shown in Figure 4.4.3. The permeability model developed in this study, however, relies primarily on the calculation of hydraulic conductance of the individual pores, and this parameter will carry the influence of the grey-level threshold on the areas and perimeters of the pores inside the image. Furthermore, the prediction of permeability relies on the number of features collected by the image analyser. Figure 4.10.1 reflects the fact that increasing threshold grey-level will begin to segment features into isolated objects, reducing connectivity and hence increasing the number of objects detected. In many ways, thresholding reflects the properties of erosion-dilation cycles in eliminating the throat-like connections between features (*Doyen*, 1988, *Ehrlich et al.*, 1991).

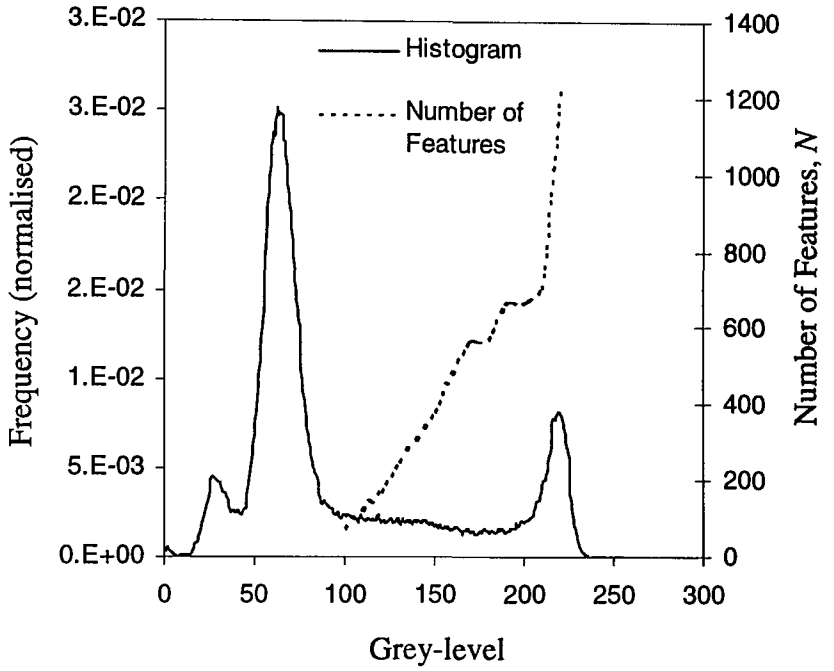

Figure 4.10.1 The plot shows the number of features collected by the image analyser truncated at 1% of the area of the largest pore as a function of grey-level, superimposed on the histogram.

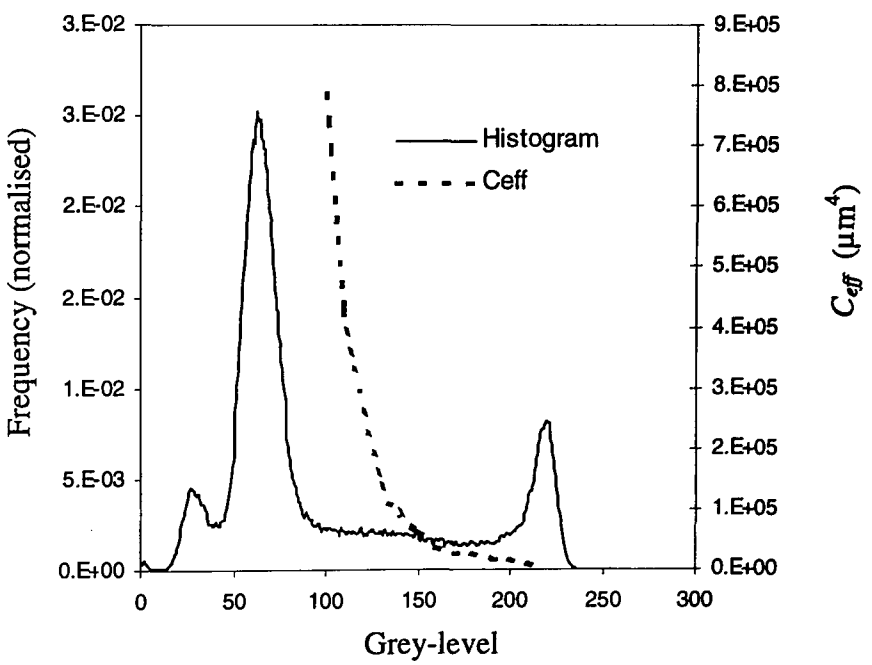

Figure 4.10.2 Variation in the effective hydraulic conductance with grey-level threshold, using a dataset that has been truncated at 1% of the area of the largest pore.

Similarly, Figure 4.10.2 serves to indicate the variation in hydraulic conductance with threshold grey-level. The effective conductance calculated using Kirkpatrick's equation exhibits a monotonic decay that is consistent with areal erosion across the entire threshold range. It may be hypothesised that smoother pores would be obtained upon raising the threshold level due to the erosion process, thereby increasing C_{eff}. However, owing to the strong correlation of hydraulic conductance with area, this hypothesis cannot be supported by the foregoing analysis.

5 STEREOLOGICAL CONSIDERATIONS

5.1 Introduction

An important issue in any 2D-section analysis is the determination of the true three-dimensional properties by a data set comprised only of planar sections. In 1848 the French geologist Delesse showed that the volume fraction of a given mineralogical phase was equal to the mean area fraction of the intersections of the planar sections with the phase. However, this is only valid for truly random materials, and can only be considered to be approximately true for "real" materials. The technique of reconstructing the characteristics of a three dimensional object from randomly orientated planar slices is known as *stereology*, a term coined by Hans Elias in 1961. The success of relating the geometry of the various two-dimensional features inside a planar section to the three-dimensional structure (*Underwood,* 1970; *Serra*, 1982) has led to the development of procedures that will lead to a correct estimate of pore-structure parameters. Such corrections are necessary, and have been implemented to account for the stereological errors that are introduced in attempting to reproduce the permeability characteristics of a three-dimensional porous material from planar sections.

5.2 Stereological Correction Factors for Hydraulic Conductance

5.2.1 The Need for a Correction Factor

The areas and perimeters of the individual pores, as measured from the BSEIs, will in general be *larger* than the actual values for the pore cross-sections. To see why this is true, consider a tubular pore of uniform cross-section, with radius r. If, during the sample preparation process, the pore so happened to be sliced perpendicularly to its axis, then its exposed cross-sectional image would be a circle of radius r. In general, however, the pore will be intersected at some arbitrary angle relative to its axis. In this case, it would appear in the SEM image as an ellipse, with a semi-minor axis equal to r, but with a semi-major axis larger than r. Both the area and the perimeter of the image would be therefore be *overestimations* of the actual area and perimeter of the pore. This effect must be accounted for before using the measured values of area and perimeter to predict the pore-tube conductances.

5.2.2 Derivation of an Expectation Value of the Hydraulic Conductance

If the rock is hydrologically isotropic, it is reasonable to assume that, on average, the angle between the pore tube axis and the image plane is a uniformly distributed random variable. To simplify the calculation, we assume a circular pore of radius r, intersected by an image plane that makes an angle θ with the plane perpendicular to the axis of the tube (Figure 5.2.1). The image of this pore would then be an ellipse whose axes are of lengths r and $a = r/\cos\theta$. The *apparent* cross-sectional area of the pore, which is to say its *measured* area, would be $\pi r^2/\cos\theta$. Hence, the relation between the actual and measured areas is

$$A_{actual} = A_{measured}\cos\theta\,. \tag{5.2.2.1}$$

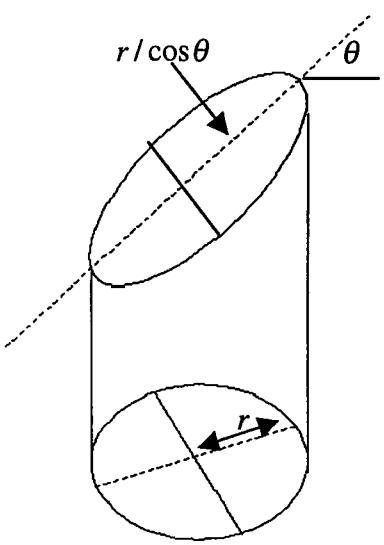

Figure 5.2.1 Illustration showing how the area of a slice through a single pore at some arbitrary angle θ will generally be larger than the true cross-sectional area.

The expectation value of the actual pore area is obtained by taking the average of A_{actual} over all possible angles of the slicing plane, in spherical polar coordinates:

$$\frac{<A_{actual}>}{A_{measured}} = <\cos\theta> = \frac{\int_0^{r=a}\int_0^{\pi/2}\int_0^{\pi/2}\cos\theta\sin\theta r^2 dr d\phi d\theta}{\int_0^{r=a}\int_0^{\pi}\int_0^{\pi/2}\sin\theta r^2 dr d\phi d\theta}$$

$$= \frac{\int_0^{\pi/2}\cos\theta\sin\theta d\theta}{\int_0^{\pi/2}\sin\theta d\theta} = \frac{\frac{1}{4}(1-\cos(\pi))}{1-\cos\theta(\pi/2)} = \frac{1}{2}, \tag{5.2.2.2}$$

and so $< A_{actual} >= 0.5 A_{measured}$.

A similar correction must be made for the perimeters of the pores. Whereas the actual perimeter of a circular pore of radius r is $\Gamma_{actual} = 2\pi r$, the measured perimeter is that of the perimeter of an ellipse with semi-major axes of lengths r and $a = r/\cos\theta$:

$$\Gamma_{measured} = 4r\int_0^{\pi/2} \sqrt{1 - \frac{a^2 - r^2}{a^2}\sin^2\theta}\, d\theta = 4rE(k,\theta), \qquad (5.2.2.3)$$

where the eccentricity of the ellipse is given by

$$k = 1 - \left(\frac{r}{a}\right)^2, \qquad (5.2.2.4)$$

and $E(k,\theta)$ is the elliptic integral of the second kind. As we eventually must integrate an expression containing the ratio $\Gamma_{meas}/\Gamma_{act}$, it is convenient to replace the elliptic integral with a simpler approximation, which is accurate to within 10% (*Beyer*, 1987):

$$\Gamma_{meas} \approx \pi\sqrt{2(a^2 + r^2)} = \pi a\sqrt{2(1 + \cos^2\theta)}\,. \qquad (5.2.2.5)$$

The expectation value of the actual perimeter is given by

$$\frac{< \Gamma_{actual} >}{\Gamma_{measured}} = \left\langle \frac{2\pi r}{\pi a\sqrt{2(1+\cos^2\theta)}} \right\rangle = \frac{\frac{2}{\sqrt{2}}\int_0^{\pi/2} \frac{\cos\theta\sin\theta}{\sqrt{1+\cos^2\theta}}\, d\theta}{\int_0^{\pi/2} \sin\theta d\theta}$$

$$= \frac{-\frac{2}{\sqrt{2}}\int_{x=1}^{x=0} \frac{x}{\sqrt{1+x^2}}\, dx}{1 - \cos(\pi/2)} = 0.59\,. \qquad (5.2.2.6)$$

Therefore, $< \Gamma_{actual} >= 0.59\Gamma_{measured}$.

Similarly, the measured hydraulic radius can be expressed as

$$[r_h]_{measured} = \frac{2A_{measured}}{\Gamma_{measured}} = \frac{2\pi r a}{\pi a\sqrt{2(1+\cos^2\theta)}}, \qquad (5.2.2.7)$$

so that the expectation value of the actual hydraulic radius is given by the following integration since $[r_h]_{actual} = r$ for a circular pore:

$$\frac{\langle [r_h]_{actual} \rangle}{[r_h]_{measured}} = \left\langle \frac{1}{\sqrt{2}} \sqrt{1+\cos^2\theta} \right\rangle = \frac{\frac{1}{\sqrt{2}} \int_0^{\pi/2} \sqrt{1+\cos^2\theta}\, \sin\theta d\theta}{\int_0^{\pi/2=} \sin\theta d\theta}$$

$$= \frac{\sqrt{2}}{4}\left[\sqrt{2} + \sinh^{-1}(1)\right] = 0.81, \qquad (5.2.2.8)$$

and so $< [r_h]_{actual} > = 0.81 [r_h]_{measured}$.

Finally, we derive an approximate expression for a stereological correction factor that converts the "measured" values of the hydraulic conductance, into "actual" values. To simplify the calculation, we again assume a circular pore where the conductance is given by

$$C_h = A\frac{A^2}{2\Gamma^2} = \frac{A}{8}\left[\frac{2A}{\Gamma}\right]^2 = \frac{A}{8} r_h^2 . \qquad (5.2.2.9)$$

The corresponding expression for the actual conductances in terms of equation (5.2.2.9) is

$$C_{actual} = \frac{A_{actual}}{8}\left[r_h^2\right]_{actual} = \frac{\pi r^2}{8}\left[\frac{2\pi r^2}{2\pi r}\right]^2 = \frac{\pi r^4}{8}. \qquad (5.2.2.10)$$

Using expression (5.2.2.5), the measured conductance is given by

$$C_{measured} = \frac{A_{measured}}{8}\left[r_h^2\right]_{measured} = \frac{1}{8}\frac{2\pi r^4}{\cos\theta(1+\cos^2\theta)}. \qquad (5.2.2.11)$$

Thus

$$\frac{C_{actual}}{C_{measured}} = \left\langle \frac{1}{2}\cos\theta(1+\cos^2\theta) \right\rangle, \qquad (5.2.2.12)$$

and so the expectation value of the actual hydraulic conductance is given by

$$\frac{< C_{act} >}{C_{meas}} = \frac{\frac{1}{2}\int_0^{\pi}\int_0^{\pi/2} \cos\theta(1+\cos^2\theta)\sin\theta\, d\theta\, d\phi}{\int_0^{\pi}\int_0^{\pi/2} \sin\theta\, d\theta\, d\phi} = \frac{1}{2}\int_0^{\pi/2} \cos\theta(1+\cos^2\theta)\sin\theta\, d\theta$$

$$= \frac{1}{2}\int_0^1 x(1+x^2)dx = \frac{3}{8}. \qquad (5.2.2.13)$$

We therefore multiply the conductances that are estimated from planar sections by 3/8 = 0.375 to calculate the true hydraulic conductance of the pores, *i.e.*

$$< C_{actual} > = 0.375 C_{measured}. \qquad (5.2.2.14)$$

5.3 Stereological Correction for Constrictivity

5.3.1 Constrictivity Concept

In general, the radius along the axis of a pore tube will be nonuniform. As a consequence of the continuously varying cross-sectional area, there will be an excess pressure drop associated with the constrictions as the fluid passes through the pore channel.

To calculate the total pressure drop, note that although r may vary with x, the volumetric flow rate Q must be the same through all cross-sections. For a "moderate" constriction the pressure drop may be approximated by integrating the Hagen-Poiseulle equation along the axis of the pore channel:

$$\Delta p = \int_0^L \frac{dp}{dx}dx = \frac{8\eta Q}{\pi}\int_0^L \frac{dx}{r^4(x)} \Delta p = \frac{8\eta Q}{\pi} L < r^{-4} >, \qquad (5.3.1.1)$$

which can be arranged to give

$$Q = \frac{\pi < r^{-4} >^{-1}}{8\eta} \frac{\Delta p}{L}. \qquad (5.3.1.2)$$

Equation (5.3.1.2) can be interpreted in terms of a tube in which all of the "resistive elements" of radius $r(x)$ and length dx are in series; the total resistance of a series connection of resistors is then found by summation (*i.e.*, by integration, when $dx \to 0$).

A planar section will gives an estimate of the constrictivity based on an arithmetic mean of the pore radii, and so from thin sections we have

$$Q = \frac{\pi < r >^4}{8\eta} \frac{\Delta p}{L}. \qquad (5.3.1.3)$$

In contrast, the integration shows how the flow is in fact controlled by the mean of r^{-4}. The hydraulic constriction factor can be defined as the ratio of these two quantities, and so

$$Q = \frac{\pi < r >^4}{8\eta} \frac{\Delta p}{L} f \,, \tag{5.3.1.4}$$

where

$$f = \frac{< r^{-4} >^{-1}}{< r >^4} \leq 1. \tag{5.3.1.5}$$

Hence, if C_h is estimated for a pore based on a single slice through that pore, the best estimate of the conductance of that pore would be found (on average, over an ensemble of such pores) by multiplying this conductance by f.

5.3.2 Estimation of the Constriction Factor

Zimmerman et al. (1991) developed a lubrication theory analysis of the permeability of rough walled fractures using a sinusoidal aperture variation model of the form

$$d(x) = d_m[1 + \delta \sin(2\pi x / \lambda)], \tag{5.3.2.1}$$

where d_m is the mean aperture, δ is the magnitude of the "roughness" and λ is the wavelength of the aperture oscillations. In order to relate f to a parameter that may be relatively simple to estimate, such as the ratio of minimum to maximum pore diameter along a given pore, *Schlueter* (1995) adopted a similar model to account for the radius variation in a tube of non-uniform cross sectional area:

$$r(x) = \langle r \rangle [1 + \varepsilon \sin(2\pi x / \lambda)], \tag{5.3.2.2}$$

where λ is the wavelength of the radius variations and ε is the amplitude. For convenience, we assume that an integral number of segments of length λ will fit into the total length L. Inserting this expression into the integral form of the Hagen-Poiseuille equation allows the hydraulic constriction factor to be expressed as

$$\frac{1}{f} = \frac{\langle r \rangle^4}{\langle r^{-4} \rangle^{-1}} = \frac{1}{\lambda} \int_0^{\lambda} [1 + \varepsilon \sin(2\pi x / \lambda)]^{-4} dx \,. \tag{5.3.2.3}$$

This integral can be evaluated by the residue theorem to yield (*Schlueter,* 1995)

$$f(\text{sinusoidal}) = \frac{256\rho^{7/2}}{(1+\rho)^4(5\rho^3+3\rho^2+3\rho+5)}, \qquad (5.3.2.4)$$

where $\rho = (1-\varepsilon)/(1+\varepsilon) = r_{\min}/r_{\max}$.

A similar analysis using a sawtooth variation in the radius shows that, except for very small values of $r_{\min}/r_{\max}$, the constriction factor curves are insensitive to the details of the radius variation. For example, if the $r(x)$ profile has a sawtooth form, which is to say that the radius varies piecewise-linearly with x, between $r_{\min}$ and $r_{\max}$, then $r(x) = r_{\min} + (r_{\max} - r_{\min}/L)x$, and

$$\frac{1}{f} = \frac{\langle r\rangle^4}{\langle r^{-4}\rangle^{-1}} = \frac{\langle r\rangle^4}{L}\int_0^L \frac{dx}{[r_{\min} + (r_{\max} - r_{\min}/L)x]^4}. \qquad (5.3.2.5)$$

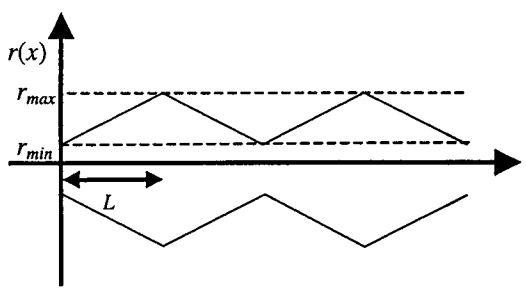

Figure 5.3.1 Pore tube with a sawtooth variation in the pore radius.

To evaluate the integral in (5.3.2.5), we put $s = x/L$, in which case $dx = Lds$, and so

$$\frac{1}{f} = \frac{<r>^4}{L}\int_0^1 \frac{Lds}{[r_{\min} + (r_{\max} - r_{\min})s]^4}$$

$$= \frac{<r>^4}{r_{\min}^4}\int_0^1 \frac{ds}{[1 + \{(r_{\max}/r_{\min}) - 1\}s]^4},$$

$$= \frac{<r>^4}{r_{\min}^4}\int_0^1 \frac{ds}{[1+as]^4}, \qquad (5.3.2.7)$$

where $\langle r\rangle = (r_{\min} + r_{\max})/2$ and $a = (r_{\max}/r_{\min}) - 1$. Evaluation of this last integral gives

$$f(\text{sawtooth}) = \frac{48a}{(a+2)^4}\left[\frac{(1+a)^3}{(1+a)^3 - 1}\right]. \tag{5.3.2.8}$$

The constant a may be rewritten in terms of ρ:

$$\rho = \frac{r_{\min}}{r_{\max}} = \frac{1}{1+a}, \tag{5.3.2.9}$$

in which case (5.3.2.8) can be written as

$$f(\text{sawtooth}) = \frac{48\rho^3}{(1+\rho)^4(1+\rho+\rho^2)}. \tag{5.3.2.10}$$

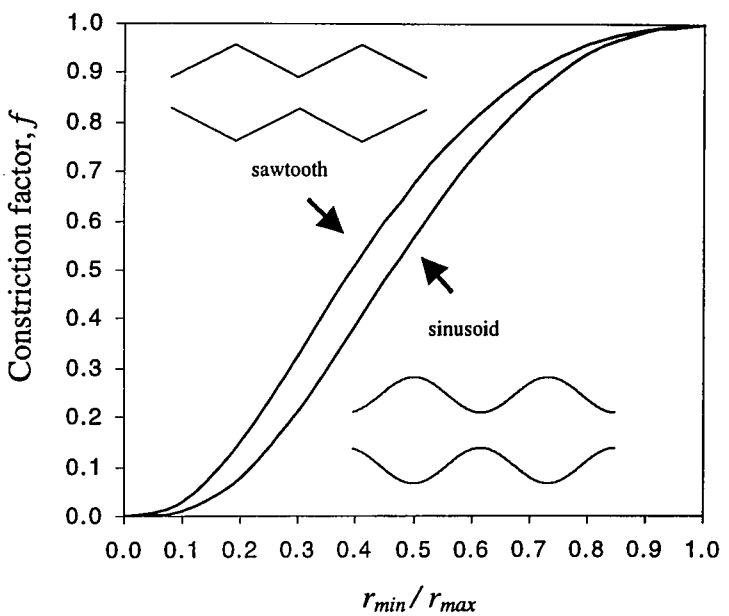

Figure 5.3.2 Constriction factor f as a function of r_{min}/r_{max} for sawtooth and sinusoidal profiles.

These constriction factors are strictly correct only for circular cross-sections, and would be difficult to calculate in the general case of irregular pore cross-sections. Furthermore, the procedure of imagining the tube to be composed of an in-series array of small conductive elements implicitly ignores local velocity components that are perpendicular to the pore axis (*van Dyke*, 1987), which will vanish only when the wavelength of the radius variation is very large. This method is therefore only a first-order perturbation approximation to the full Navier-Stokes equations, in terms of the

parameter $\lambda / < r >$. *Bernabé and Olson* (2000) showed that the higher-order corrections are negligible as long as $\lambda / < r >$ exceeds 0.15. For smaller wavelengths, the "integrated Hagen-Poiseuille" equation, (5.3.1.2), is no longer a good approximation to the more fundamental Navier-Stokes equations, and one would need to examine to higher-order perturbations (*Sisavath et al.*, 2001).

5.3.3 Choosing r_{min}/r_{max} to Calculate a Constriction Factor

A constriction factor f can be calculated from equations (5.2.3.4) or (5.3.2.10) using an estimate of the ratio $r_{\min} / r_{\max}$. In some previous network models, a parameter similar to $r_{\min} / r_{\max}$ has been interpreted as the "pore throat/pore body" ratio (*McCreesh et al.*, 1991), but we do not attach such an interpretation to this parameter. In our model, the flow network consists only of "pores", which meet at (volumeless) nodes. The variation in pore size (between nodes) is accounted for, within the context of laminar flow theory, by the constriction factor.

It is not clear if $r_{\min} / r_{\max}$ values can be estimated from two-dimensional images, so we appeal to other estimates of this parameter. *Cargill* (1984) examined the void space formed by a simple cubic arrangement of monodisperse spheres, and found a value of 0.57. *Bourbié et al.* (1987) acknowledge the geometric complexity of a random sphere packing but suggest that regularly packed systems of spheres offer a preliminary view of the interstitial void ratio. For more compact arrangements such as the simple hexagonal packing, $r_{\min} / r_{\max}$ may be as low as 0.29. Both cubic and hexagonal arrays have been previously used to make estimates of the constrictivity of monodisperse sphere packings as a function of particle size (*Graton and Fraser*, 1935). *Haines* (1930) explored the behavior of packed beds in a capillary suction experiment and showed that for an arbitrary packing the entry and re-entry pressures, as governed by the Laplace equation, covered a range bounded by the extreme values for the cubic and hexagonal packings.

Estimates of $r_{\min} / r_{\max}$ have also been obtained from pore casts (*Schlueter*, 1995), and complete void-size distributions have been obtained by a combination of mercury and image data (*Pittman*, 1984, *Basan et al.*, 1997), and also from 3-D reconstructions (*Lindquist and Venkatarangan*, 1999, *Lindquist et al.*, 2000). However, as our intention is to develop a permeability model that utilises no information other than from 2-D images, we will tentatively use the average value between the simple cubic and

hexagonal packings of 0.43 for all sandstones, in which case equations (5.2.3.4) and (5.2.3.10) give hydraulic constriction factors of 0.44 and 0.57, respectively.

5.4 Stereological Correction Factor for Pore Number Density

5.4.1 The Need for a Correction Factor

A consideration must be made of the overestimation in the areal number density of pores that occurs as a consequence of taking an arbitrary two-dimensional slice that probably does not lie in a plane perpendicular to a lattice direction. If we assume a hypothetical cubic lattice, then a slice taken perpendicular to a given lattice direction will only intersect those pores that lie along that direction. If, however, the slicing plane is not normal to the lattice direction, it will also intersect some pores that are orthogonal to that first lattice direction (Figure 5.4.1) leading to an overestimation in the number density of pores.

5.4.2 Derivation of an Expectation Value for Number Density

Consider a two-dimensional slice through the square lattice at an angle θ to the x-axis. Without loss of generality, the lattice parameter can be taken to be unity, in which case a slice of length L taken perpendicular to a lattice direction would intersect L pores. For a slice of length L at an angle θ to the x-axis, the number of intersected pores oriented in the y-direction will be $L\cos\theta$, and the number of intersected pores oriented in the x-direction will be $L\sin\theta$.

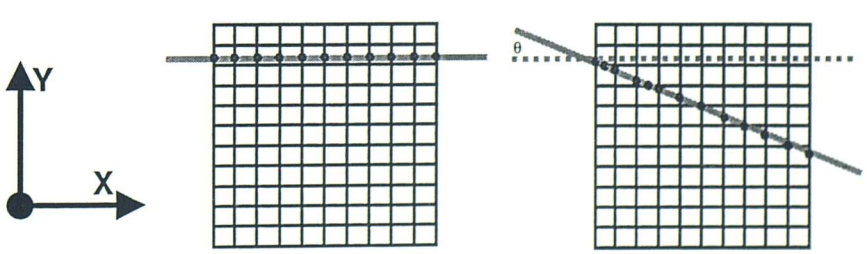

Figure 5.4.1 A two-dimensional illustration showing the number of additional pores bisected when a slice is taken at an angle θ that is not perpendicular to a lattice direction.

An arbitrary slice taken through a three-dimensional lattice may also be specified by its outward unit normal vector. As the angle between any two planes is equivalent to

that between their outward normals, we can specify the orientation of a random slice with respect to the faces of a cubic lattice in three-dimensions by means of the direction cosines of the outward unit normal vector of the slicing plane. The number density of pore intersections made by an arbitrary slice, is similarly related to the "true" number density (in a lattice direction) by

$$\rho_{slice} = (\cos\alpha + \cos\beta + \cos\gamma)\rho_{actual}. \tag{5.4.2.1}$$

We may then specify the orientation of an arbitrary slice taken through a cube by considering the angles between the plane the arbitrary slice generates and each separate face of the cube. More simply, this is achieved by considering the normal form of the plane and noting that the angle between any two planes will be equivalent to that between their outward normals $\mathbf{n_1}$ and $\mathbf{n_2}$. Thus, we may express the angle between any two planes as

$$\cos\theta = \frac{\mathbf{n}_1 \cdot \mathbf{n}_2}{|\mathbf{n}_1||\mathbf{n}_2|}, \tag{5.4.2.2}$$

For a slice through a cube, the angle between the plane and a lattice face is equivalent to the angle between the outward normal $\mathbf{n}$ and the axis perpendicular to the face. Thus, the angle between $\mathbf{n}$ and the z axis is given by the direction cosine

$$\cos\gamma = \frac{\mathbf{n}\cdot\mathbf{e}_z}{|\mathbf{n}||\mathbf{e}_z|}. \tag{5.4.2.3}$$

Similarly, the angle between the plane and the xz face is equivalent to that between the outward normal $\mathbf{n}$ and a vector directed perpendicular to xz plane (parallel to the y axis). This is the angle between $\mathbf{n}$ and the y axis, the direction cosine being

$$\cos\alpha = \frac{\mathbf{n}\cdot\mathbf{e}_y}{|\mathbf{n}||\mathbf{e}_y|}. \tag{5.4.2.4}$$

Finally, the angle between the plane and yz face is equivalent to that between the outward normal $\mathbf{n}$ and a vector directed perpendicular to yz plane (parallel to the z axis). This is the angle between $\mathbf{n}$ and the x axis, the direction cosine being

$$\cos\beta = \frac{\mathbf{n}\cdot\mathbf{e}_x}{|\mathbf{n}||\mathbf{e}_x|}. \tag{5.4.2.5}$$

We may write the equation for the outward normal in terms of the direction cosines as

$$\mathbf{n} = \mathbf{e}_x \cos\alpha + \mathbf{e}_y \cos\beta + \mathbf{e}_z \cos\gamma, \qquad (5.4.2.6)$$

where

$$\cos\alpha = \frac{x}{r}, \qquad \cos\beta = \frac{y}{r}, \qquad \cos\gamma = \frac{z}{r} \quad \text{and} \quad r = \sqrt{x^2 + y^2 + z^2}\,. \qquad (5.4.2.7)$$

The expectation value of the measured number density, ρ_{slice} is found from (5.4.2.1) by averaging the sum of the direction cosines over all possible angles of the slicing plane:

$$\frac{<\rho_{slice}>}{\rho_{actual}} = \langle \cos\alpha + \cos\beta + \cos\gamma \rangle. \qquad (5.4.2.8)$$

As we wish to obtain the average values of the direction cosines over all possible angles, we must convert the expressions (5.4.2.7) into spherical coordinates, where (Figure 5.4.2)

$$x = r\sin\theta\cos\phi \qquad y = r\sin\theta\sin\phi \qquad z = r\cos\theta, \qquad (5.4.2.9)$$

and from (5.4.2.7) and (5.4.2.9) we may write

$$\cos\alpha = \sin\theta\cos\phi, \qquad \cos\beta = \sin\theta\sin\phi \qquad \text{and} \qquad \cos\gamma = \cos\theta\,. \quad (5.4.2.10)$$

From the relations in (5.4.2.10), we may then write the sum of the direction cosines appearing in (5.4.2.1) in spherical polar co-ordinates as follows:

$$\frac{\rho_{slice}}{\rho_{actual}} = \sin\theta\cos\phi + \sin\theta\sin\phi + \cos\theta\,. \qquad (5.4.2.11)$$

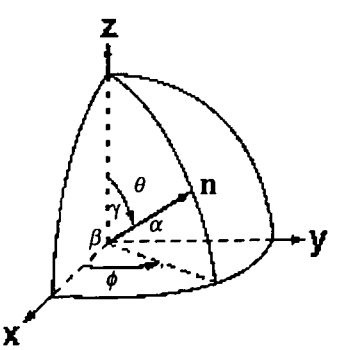

Figure 5.4.2 Illustration showing the relation between the angles that specify the outward normal **n**, $\{\alpha, \beta, \gamma\}$ and the azimuthal and polar angles θ and ϕ.

The expectation value (5.4.2.8) of this quantity is obtained by integrating over all possible angles of the slicing plane. Due to the symmetry of a cubic lattice, the integration can be taken between 0 and $\pi/4$ for both θ and ϕ:

$$\frac{<\rho_{slice}>}{\rho_{actual}} = \frac{\int_0^{\pi/4}\int_0^{\pi/4}\{\sin\theta\cos\phi + \sin\theta\sin\phi + \cos\theta\}\sin\theta d\theta d\phi}{\int_0^{\pi/4}\int_0^{\pi/4}\sin\theta d\theta d\phi}$$

$$= \frac{\left[\frac{\pi}{8} - \frac{1}{4}\right] + \frac{\pi}{16}}{\frac{\pi}{\sqrt{32}}\left[\sqrt{2}-1\right]} = \frac{1}{4\pi}\frac{(3\pi-4)}{\left(1-\sqrt{1/2}\right)} \approx 1.47. \qquad (5.4.2.12)$$

We therefore divide the number of pores that we estimate from the image by 1.47 to correct for the overestimation in the pore number density, and so

$$\rho_{actual} = \frac{\rho_{slice}}{1.47}. \qquad (5.4.2.13)$$

A similar integral can be derived in the case of two dimensions (Figure 5.4.1). In this case the expectation value is obtained by carrying out an integration of the direction cosines in plane polar co-ordinates as follows:

$$\frac{\langle\rho_{slice}\rangle}{\rho_{actual}} = \frac{\int_0^{\pi/4}\{\sin\theta + \cos\theta\}d\theta}{\int_0^{\pi/4}d\theta} = \frac{4}{\pi} \approx 1.27. \qquad (5.4.2.14)$$

It is interesting to note that the value in two dimensions is somewhat less than for the three-dimensional case, and suggests that in higher dimensions the expectation value increases since the number of lattice points becomes more "dense". Consequently, the probability of an arbitrary plane bisecting additional pores will increase accordingly.

6 NETWORK MODELLING OF PERMEABILITY

6.1 Introduction

This section is concerned with the methods used to estimate the overall conductance that is obtained by inputting a set of discretely-valued conductances into a network. Two approaches are employed: an effective-medium approximation that determines an "average" conductance based on the statistics of local conducting elements in a self-consistent manner, and explicit network calculations that we perform using the network simulation code NETSIM (*Jing,* 1990), which solves the flow equations in a cubic network of conductors.

6.2 Kirkpatrick's Effective-Medium Approximation

The purpose of an effective-medium approximation is to allow the replacement of each conductor C_i in a network by a conductor having some "effective value" C_{eff}. Figure 6.2.1 illustrates the transformation of a resistor network of discrete conductances into an equivalent, homogenous resistor network in which all the individual conductances have been mapped to the same effective value, while preserving the topology of the network.

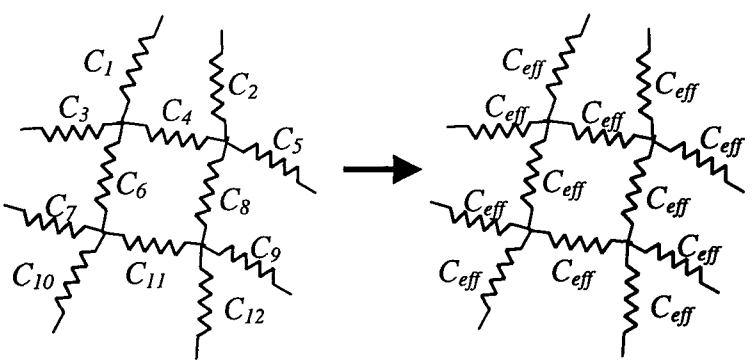

Figure 6.2.1 An illustration showing the replacement of a discrete network of conductances by a homogeneous network having the same topology.

The self-consistent procedure of *Kirkpatrick* (1973) leads to the construction of an effective conductance by the superposition principle in which the replacement of each single conductor C_i by a trial conductance is applied to each bond in the network, such that the resulting fluctuations in the potentials at the nearby nodes are minimised. This

procedure is repeated until the successive updating of the trial conductance eventually causes the fluctuations to average out to zero. The trial conductance has then reached an effective value throughout the network. This leads to the following equation that implicitly defines C_{eff} as the solution of the following equation:

$$f(C_{eff}) = \sum_{i=1}^{N} \frac{C_{eff} - C_i}{[(z/2)-1]C_{eff} + C_i} = 0, \qquad (6.2.1)$$

where the co-ordination number z represents the number of conductors that meet at each node, and the summation is taken over each individual physical conductor in the network. Kirkpatrick's equation (6.2.1) can be solved by using either the bisection algorithm, or a one-dimensional Newton-Raphson procedure. Either root-finding algorithm used the geometric mean of the input conductances as an initial guess to begin the iterative solution. Figure 6.2.2 shows the form of the Kirkpatrick function for a set of 21 conductances derived from a fracture network (*Priest*, 1992). The root is bracketed from below by the harmonic mean, corresponding to the limiting case of a serially connected network, and from above by the arithmetic mean, corresponding to the network being connected in parallel. The lower bound corresponds to a co-ordination number of $z = 2$, whereas the upper bound is approached as the co-ordination number becomes infinite. For $z = 6$, Kirkpatrick's equation is solved numerically for a given set of input conductances.

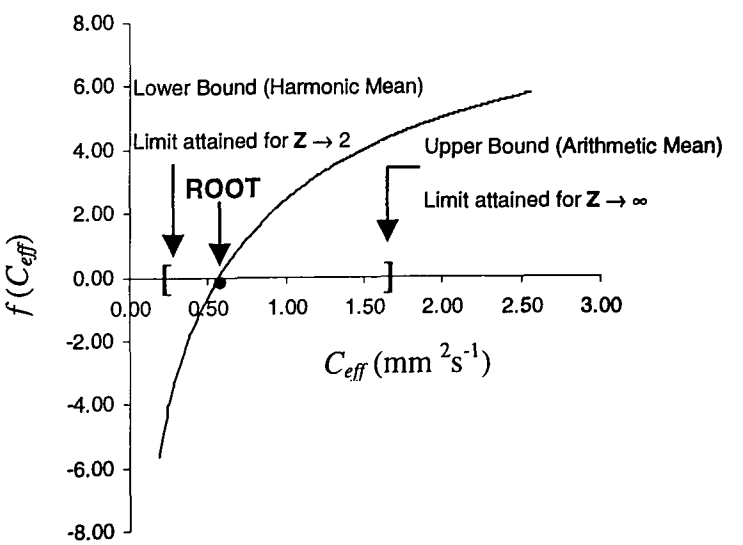

Figure 6.2.2 Kirkpatrick's function for the 21 conductance values used by *Priest* (1992). Note that Priest's definition of C has the factor of ηL incorporated into it.

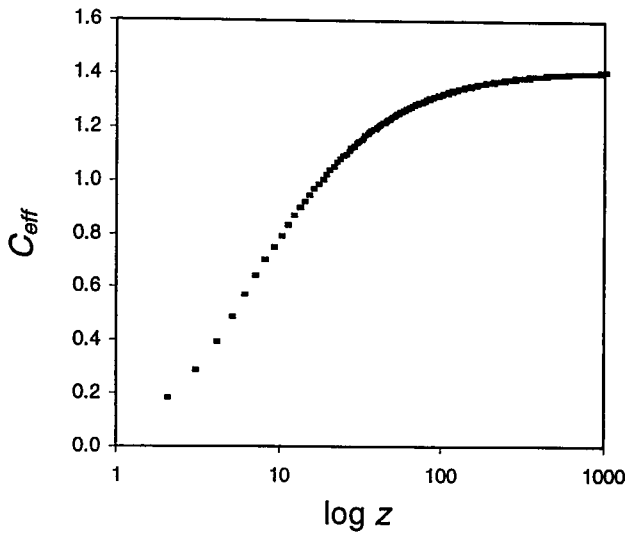

Figure 6.2.3 Sensitivity of C_{eff} to co-ordination number, using Priest's data set.

Kirkpatrick (1973) derived equation (6.2.1) under the assumption that the co-ordination number of each node was the same, although it has been shown (*Koplik*, 1982) that his result can be used for topologically irregular networks by defining z to be the *mean* co-ordination number of all the nodes in the network. In the present study we set $z = 6$, and hence model the transport on a hypothetical isotropic cubic lattice. *Doyen* (1988) chose a mean co-ordination number of six for a Fontainebleau sandstone on the assumption that the pore-space connectivity was similar to that of a close random packing of grains. *Koplik et al.* (1984) used $z = 3.49$, based on a connectivity analysis of ten sectionals of Massilon sandstone, and more recent work by *Lindquist et al.* (2000) gave average co-ordination numbers ranging between 3.37 to 3.75 for Fontainebleau sandstones using three-dimensional tomographic techniques. *Jerauld and Salter* (1990) reviewed the experimental evidence on co-ordination numbers of pore networks in sedimentary rocks, and concluded that z typically ranged from four to eight. *Schlueter* (1995) found that C_{eff} varies by only ± 20% when z ranges from 5-7, providing some justification for using a co-ordination number of six. This value is also consistent with a cubic lattice, whose simple topology allows a direct relationship between the effective conductances of the individual pore tubes, C_{eff}, and the overall conductance of the network, C_{eq}. We also note that a more accurate estimation of z would require three-dimensional imaging of some sort, which we aim to avoid.

One issue that arises is whether or not Kirkpatrick's equation will have one real solution. The physically meaningful solution to the conductance problem requires that the desired root lies between the bounds dictated by the harmonic and arithmetic mean of the conductances, and so it only becomes necessary to consider the uniqueness of the solution inside this interval. Kirkpatrick's function is continuous at every point in the closed interval defined by the harmonic and arithmetic means of the hydraulic conductances. Figure 6.2.3 shows that $f(C_{eff})$ is negative at the lower bound and positive at the upperbound, and so by the Intermediate Value Theorem, there must exist at least one point where the function crosses the C_{eff} axis: this is the basis of the bisection algorithm. We also recognise that this only occurs only once inside this interval, since the first derivative is positive everywhere for all values of z inside this interval, *i.e.*,

$$f'(C_{eff}) = \sum_{i=1}^{N} \frac{(z/2)C_i}{\{[(z/2)-1]C_{eff} + C_i\}^2} > 0. \qquad (6.2.2)$$

Consequently, we can expect only one real root within this interval.

6.3 The Anisotropic Effective-Medium Approximation

6.3.1 Introduction

The determination of an effective conductance by finding the bound root of Kirkpatrick's equation will solve the conductance problem for an isotropic network, and uses a root finding algorithm in one dimension. It would, however, be preferable to use an inherently anisotropic model such as that of *Bernasconi* (1974), which allows the calculation of the effective conductance in a given direction on an anisotropic network where data from three orthogonal directions is used, and so three directional conductances are computed in a coupled manner.

Depending on the number of lattice directions, the procedure involves the solution of d dimensional Kirkpatrick-type equations, where the conductances in a given direction are mapped to the same value to form the effective anisotropic network. Computionally, a root-finding algorithm is used to find the zeros of these coupled equations in d dimensions. Applying the procedure in three dimensions then requires the input of three sets of hydraulic conductance data.

6.3.2 Bernasconi's Equations in Two and Three Dimensions

Bernasconi's equations for flow on a square lattice are

$$f_1(C_{eff}^x, C_{eff}^y) = \sum_i^P \frac{C_{eff}^x - C_i^x}{C_i^x + \left[C_{eff}^x \left\{ \frac{\tan^{-1}(C_{eff}^y / C_{eff}^x)^{1/2}}{\tan^{-1}(C_{eff}^x / C_{eff}^y)^{1/2}} \right\} \right]} = 0 \qquad (6.3.2.1)$$

and

$$f_2(C_{eff}^y, C_{eff}^x) = \sum_j^Q \frac{C_{eff}^y - C_j^y}{C_j^y + \left[C_{eff}^y \left\{ \frac{\tan^{-1}(C_{eff}^x / C_{eff}^y)^{1/2}}{\tan^{-1}(C_{eff}^y / C_{eff}^x)^{1/2}} \right\} \right]} = 0 \qquad (6.3.2.2)$$

where C_{eff}^x and C_{eff}^y are the effective conductances in the x and y directions.

We wish to find the simultaneous zeros of equations (6.3.2.1) and (6.3.2.2). These functions each have zero contour boundary lines that divide the (x,y) plane into regions where the respective function changes sign. The solutions to the conductance problem in two dimensions are those points that are common to both the zero contours of both f_1 and f_2. In order to find all common points where there may be overlap of the zero contour boundaries, we can plot out the contours of each function and note the regions in the (x,y) plane where they bisect. Again, the issue of uniqueness of solution arises, since in general the zero contours will generally form an unknown number of disjoint closed curves.

To illustrate the form of the contour plots for Bernasconi's equation in two-dimensions, an anisotropic lattice containing two pores for each of the x and y directions was constructed using the following expressions by expanding the summations (6.3.2.1) and (6.3.2.2) for a two-pore system:

$$2A_x[C_{eff}^x]^2 + C_{eff}^x[C_1^x + C_2^x - A_x(C_1^x + C_2^x)] - 2C_1^x C_2^x = 0, \qquad (6.3.2.3)$$

and

$$2A_y[C_{eff}^y]^2 + C_{eff}^y[C_1^y + C_2^y - A_y(C_1^y + C_2^y)] - 2C_1^y C_2^y = 0, \qquad (6.3.2.4)$$

where

$$A_x = \frac{\tan^{-1}(C^y_{eff}/C^x_{eff})^{1/2}}{\tan^{-1}(C^x_{eff}/C^y_{eff})^{1/2}} \quad \text{and} \quad A_y = \frac{\tan^{-1}(C^x_{eff}/C^y_{eff})^{1/2}}{\tan^{-1}(C^y_{eff}/C^x_{eff})^{1/2}}. \qquad (6.3.2.5)$$

The use of a two-pore system makes the calculation simple. If we then plot these two functions for arbitary values of $\{C_1^x, C_2^x\}$ and $\{C_1^y, C_2^y\}$, we obtain a relatively simple contour diagram where a single bisection of the zero contours is identified in the x, y plane (Figure 6.3.1). This crossing of the two functions occurs at values of C^x_{eff} and C^y_{eff} that correspond to the values obtained by running a effective-medium simulation using Bernasconi's equation in two dimensions for the same values of $\{C_1^x, C_2^x\}$ and $\{C_1^y, C_2^y\}$.

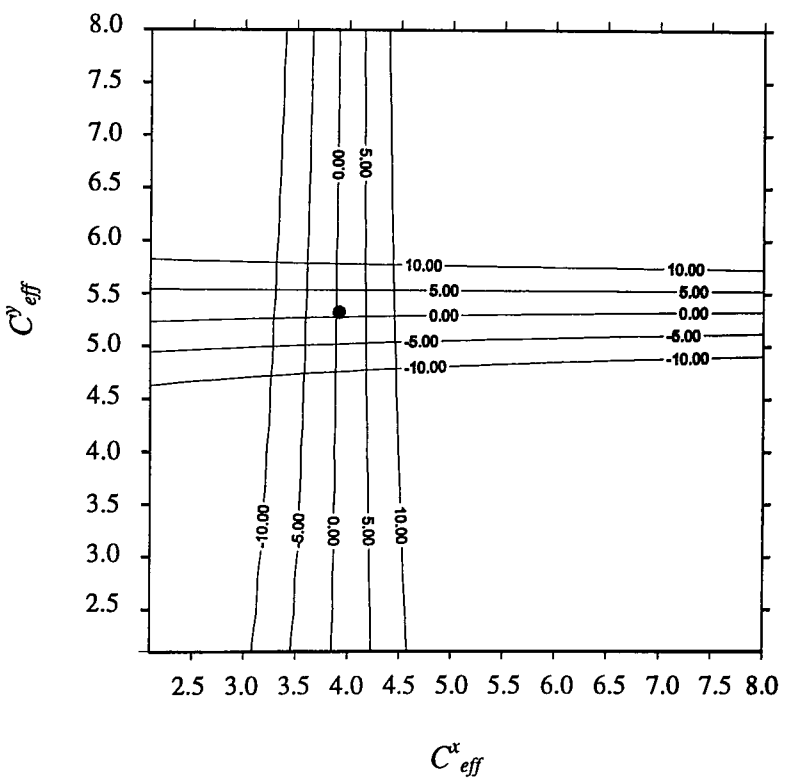

Figure 6.3.1 A contour plot for an anisotropic two-pore system.

As we are primarily concerned with the application of anisotropic effective medium theory to three dimensional porous media, we use the approximate equations of Bernasconi for flow on an effective anisotropic cubic lattice. The three equations are formed by a cyclic permutation of the $\{\nu\}=\{1,2,3\}$ indices of the following expressions:

$$f_v(C_{eff}^{v=1}, C_{eff}^{v=2}, C_{eff}^{v=3}) = \sum_{k=1}^{n} \frac{C_{eff}^{v} - C_k}{A_v\{C_{eff}^{v=1}, \ldots C_{eff}^{v=d}\} + C_k} = 0, \qquad (6.3.2.6)$$

where

$$A_v\{C_{eff}^{v=1}, C_{eff}^{v=2}, C_{eff}^{v=3}\} \approx C_{eff}^{v=1} \frac{\tan^{-1}\left\{\left[C_{eff}^{v=1}C_{eff}^{v=2} + C_{eff}^{v=2}C_{eff}^{v=3} + C_{eff}^{v=3}C_{eff}^{v=1}\right]^{1/2} / C_{eff}^{v=1}\right\}}{\tan^{-1}\left\{C_{eff}^{v=1} / \left[C_{eff}^{v=1}C_{eff}^{v=2} + C_{eff}^{v=2}C_{eff}^{v=3} + C_{eff}^{v=3}C_{eff}^{v=1}\right]^{1/2}\right\}}, \qquad (6.3.2.7)$$

and so

$$f_1(C_{eff}^{x}, C_{eff}^{y}, C_{eff}^{z}) = \sum_{i}^{P} \frac{C_{eff}^{x} - C_i^{x}}{C_i^{x} + \left[C_{eff}^{x}\left\{\frac{\tan^{-1}(C_{eff}^{x}C_{eff}^{y} + C_{eff}^{y}C_{eff}^{z} + C_{eff}^{z}C_{eff}^{x})^{1/2} / C_{eff}^{x}}{\tan^{-1}(C_{eff}^{x} / (C_{eff}^{x}C_{eff}^{y} + C_{eff}^{y}C_{eff}^{z} + C_{eff}^{z}C_{eff}^{x})^{1/2}}\right\}\right]} = 0, \qquad (6.2.3.8)$$

$$f_2(C_{eff}^{y}, C_{eff}^{z}, C_{eff}^{x}) = \sum_{j}^{Q} \frac{C_{eff}^{y} - C_j^{y}}{C_j^{y} + \left[C_{eff}^{y}\left\{\frac{\tan^{-1}(C_{eff}^{y}C_{eff}^{z} + C_{eff}^{z}C_{eff}^{x} + C_{eff}^{x}C_{eff}^{y})^{1/2} / C_{eff}^{y}}{\tan^{-1}(C_{eff}^{y} / (C_{eff}^{y}C_{eff}^{z} + C_{eff}^{z}C_{eff}^{x} + C_{eff}^{x}C_{eff}^{y})^{1/2}}\right\}\right]} = 0, \qquad (6.2.3.9)$$

$$f_3(C_{eff}^{z}, C_{eff}^{x}, C_{eff}^{y}) = \sum_{k}^{R} \frac{C_{eff}^{z} - C_k^{z}}{C_k^{z} + \left[C_{eff}^{z}\left\{\frac{\tan^{-1}(C_{eff}^{z}C_{eff}^{x} + C_{eff}^{x}C_{eff}^{y} + C_{eff}^{y}C_{eff}^{z})^{1/2} / C_{eff}^{z}}{\tan^{-1}(C_{eff}^{z} / (C_{eff}^{z}C_{eff}^{x} + C_{eff}^{x}C_{eff}^{y} + C_{eff}^{y}C_{eff}^{z})^{1/2}}\right\}\right]} = 0. \qquad (6.2.3.10)$$

The extension of the root finding procedure to three dimensions means that we seek points relating to the coincident bisection of the zero contours of three surfaces defined by equations (6.2.3.8-10).

The computational procedure we have used for calculating the effective conductances on both the square and cubic lattice is the generalised Newton-Raphson algorithm outlined by *Press et al.* (1992). The procedure for finding a root in one dimension relies on the fact that we can perform an iterative procedure to attain a real root based on the truncation of the Taylor series expansion of a function. The problem of multidimensional root finding is cast into a similar problem in which we have d equations in as many unknowns, and so we require

$$\begin{aligned} F_{i=1}(x_1, x_2, \ldots, x_d) &= 0 \\ F_{i=2}(x_1, x_2, \ldots, x_d) &= 0 \\ &\vdots \\ F_{i=d}(x_1, x_2, \ldots, x_d) &= 0 \end{aligned}, \qquad \text{for } i = 1, 2, \ldots, d. \qquad (6.3.2.11)$$

If we consider $\mathbf{x}$ to be a vector with components x_i and $\mathbf{F}$ to be a column vector with components F_i, then we can expand $\mathbf{F}$ as a Taylor series:

$$F_i(\mathbf{x}+\Delta\mathbf{x}) = F_i(\mathbf{x}) + \sum_{j=1}^{N} \frac{\partial F_i}{\partial x_i}\Delta x_i + \ldots \qquad (6.3.2.12)$$

Using matrix notation we may rewrite this expression in terms of the Jacobian as follows

$$\mathbf{F}(\mathbf{x}+\Delta\mathbf{x}) \approx \mathbf{F}(\mathbf{x}) + \mathbf{J}\Delta\mathbf{x}\,. \qquad (6.3.2.13)$$

Setting $\mathbf{F}(\mathbf{x}+d\mathbf{x}) = \mathbf{0}$ gives the linear system of equations $\mathbf{J}\Delta\mathbf{x} = -\mathbf{F}$. Inversion gives the corrections $\Delta\mathbf{x}$ which are added to the solution vector $\mathbf{x}_{n+1} = \mathbf{x}_n + \Delta\mathbf{x}$, and the process is iterated as in the one dimensional procedure to some prescribed tolerance, *i.e.*,

$$\mathbf{F}(\mathbf{x}+\Delta\mathbf{x}) \approx \mathbf{F}(\mathbf{x}) + \mathbf{J}\Delta\mathbf{x} = 0 \quad \Rightarrow \quad \Delta\mathbf{x} = -\mathbf{J}^{-1}\mathbf{F}(\mathbf{x}). \qquad (6.3.2.14)$$

The initial guesses for the components of the solution vector were taken to be the geometric means of the input hydraulic conductances for the x, y and z directions. Consequently, the most labourious part of the procedure is the implementation of the Jacobean matrix into the algorithm MNEWT (*Press et al.*, 1992).

6.3.3 Equivalence of Bernasconi and Kirkpatrick's EMA for Isotropic Systems

It can be shown that for an isotropic lattice the expressions given by equations (6.3.2.1) and (6.3.2.2) will give the same value for the effective conductance as the isotropic effective medium theory of Kirkpatrick. In this instance we recognise that the effective conductances along each lattice direction should be identical, *i.e.*,

$$\sum_{k=1}^{n} \frac{C_{eff}^{v} - C_k}{A_v\{C_{eff}^{v=1},\ldots,C_{eff}^{v=d}\} + C_k} = \sum_{k=1}^{n} \frac{C_{eff} - C_k}{[(z/2)-1]+C_k}\,. \qquad (6.3.3.1)$$

For the square lattice, $z = 4$ and so when $C_{eff}^{1} = C_{eff}^{2}$ we have

$$A_v = \frac{\tan^{-1}(1)}{\tan^{-1}(1)} = 1 \equiv \frac{z}{2} - 1. \qquad (6.3.3.2)$$

For the cubic lattice, we similarly equate the dimensionless expression A_v with [(z/2)-1] for $z = 6$. Hence, for $C_{eff}^{1} = C_{eff}^{2} = C_{eff}^{3}$ we have, from equation (6.3.2.7),

$$A_v = \frac{\tan^{-1}[(3C_{eff})^{1/2}/C_{eff}]}{\tan^{-1}[C_{eff}/(3C_{eff})^{1/2}]} = \frac{\tan^{-1}\sqrt{3}}{\tan^{-1}\sqrt{1/3}} = \frac{\pi/3}{\pi/6} = 2, \qquad (6.3.3.3)$$

which shows the equivalence of Bernasconi's anisotropic effective medium approximation with Kirkpatrick's equation when the lattice is isotropic.

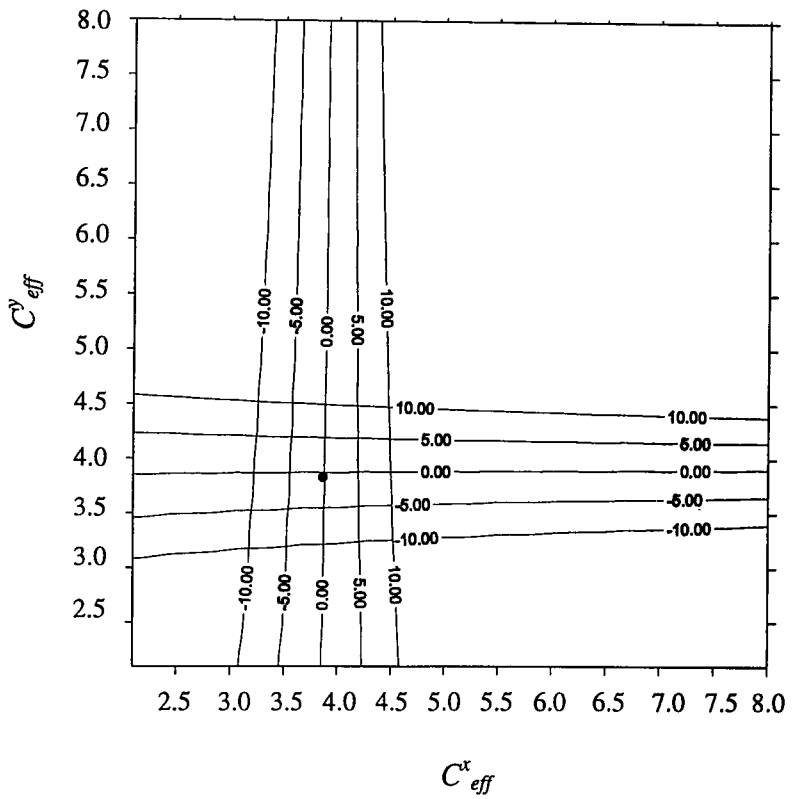

Figure 6.3.2 A countour plot for an isotropic two-pore system.

If we return to the two-pore system and input two identical sets of conductances for the x and y directions, we can verify that we also obtain a common point at which the zero contours bisect. Isotropy ensures that this point will lie along the line $C^x_{eff} = C^y_{eff}$, as verified in Figure 6.3.3.

6.3.4 Convergence of the Newton-Raphson Procedure in Higher Dimensions

The one-dimensional Newton-Raphson iteration in general exhibits extremely poor global convergence (*Finney and Thomas*, 1994), and the success of locating a root of a function depends on the quality of the initial guess. This is also true of the Newton-Raphson procedure in higher dimensions. Fortunately, we can again use the fact that we

expect the desired root to be located close to the geometric mean of the input conductances, and therefore rely on the local convergence characteristics of the algorithm. *Press et al.* (1992) suggest alternative methods that are designed to improve the global convergent characteristics of the basic algorithm. The implementation that we used was found to be adequate in finding the common zeros in both two and three dimensions, and to be the most rapidly convergent when using identical input files of conductances, that is when checking the output of the Bernasconi implementation against Kirkpatrick's isotropic effective medium approximation. The rate of convergence decreased when using data obtained from thin sections orientated in different directions, however, the effect was not sufficient for the algorithm to fail to converge. The use of the geometric means of the input data as initial guesses for iteration to the effective conductances corresponding to the different lattice directions was found to be sufficient in all simulations, and a consideration of the more advanced treatments of the Newton-Raphson technique in higher dimension was deemed to be unnecessary.

6.4 "Exact" Network Solutions using NETSIM

6.4.1 Introduction

NETSIM is a network simulation code that models transport phenomena in porous media on a cubic lattice of pore tubes. Two versions of NETSIM are discussed in this chapter, ISONETSIM, the code listing of which may be found in Appendix G, and ANISONETSIM, the code listing of which may be found in Appendix H. In the former, an exact network calculation for the conductance is performed in three dimensions on an *isotropic* cubic lattice by using a single input file to populate the network in each of the three principal directions. In ANISONETSIM, a similar calculation is performed, however, the main feature that distinguishes this program from ISONETSIM is that three input files containing conductance data from three mutually orthogonal directions are used, each decorating the lattice in one specific direction only. Consequently, this allows flow simulations to be performed on an *anisotropic* cubic lattice. Permuting the order in which the three external sets of data are fed into the lattice allows the interchange of the flow directions so that the potential can be applied consecutively along each direction. The differences in the two programs are therefore attributable only to the method in which the data is input and their intrinsic character is essentially the

same. Either version of the original code NETSIM (*Jing,* 1990) can be described as consisting of five major blocks:

1. A cubic lattice is specified in terms of nodes that connect bonds, and the latter are subsequently decorated with conductances from an external file in a random manner.
2. The boundary conditions are then specified, with a fixed pressure gradient in one direction only, and no-flow boundaries along the remaining orthogonal faces.
3. The flowrate is calculated for the given potential using the Successive Over Relaxation technique of *Young* (1971).
4. An output conductance is then calculated by dividing the net flow rate coming out of the cubic network by the total potential.

David et al. (1990) showed that a conductance C_o adopted by all bonds in a regular homogenised network is given by the following expression (Section 2.4.4):

$$C_o = \frac{C_{eq}}{C[1]}, \tag{6.4.1.1}$$

where C_{eq} is the net conductance of the individual pores, and $C[1]$ represents the overall conductance of the equivalent homogeneous network with the same topology, when the individual conductances are set to unity. The following expression for $C[1]$ on the square lattice, as a function of the number of nodes, p, has been given by *David et al.* (1990) as

$$C[1]_{square} = \frac{p}{p+1}. \tag{6.4.1.2}$$

A similar expression for $C[1]$ can be derived for a cubic network by again considering the topology of the three-dimensional lattice:

$$C[1]_{cubic} = \frac{p^2}{p+1}. \tag{6.4.1.3}$$

5. As a final step in the network calculation, the net conductance C_{eq} is normalised to $C[1]$ using eq. 6.4.1.3 in eq. 6.4.1.1 to give the equivalent conductance of the homogeneous network. The values of C_o calculated explicitly by this means allow validation of the values C_{eff} obtained using the effective medium technique of

Kirkpatrick, since we can directly assess the difference between C_0 and C_{eff} obtained from the two simulations.

6.4.2 Running Isotropic Simulations with ISONETSIM

The development of a consistent means of preprocessing input data, and the subsequent running of each simulation, is necessary in order to form a methodology that can be applied confidently to any dataset.

The first issue that must be addressed is: at what lattice size should the network simulations be performed, and what number of realisations of the single input file will be necessary to ensure solution convergence? To investigate this, a set of 30 realisations of a preprocessed datafile were input into lattices ranging in size from 5 to 40 nodes, sizes increasing in increments of 5. The realisations were generated sequentially, using a library random number generator, to randomise the conductances from an external source, with the added modification that each conductance was selected only once for the outfile to ensure that it contained uniquely randomised data. To monitor the fluctuations in the output of the network code, an average percent difference was used, by comparing the effective-medium solution provided by Kirkpatrick's equation for the same set of conductances.

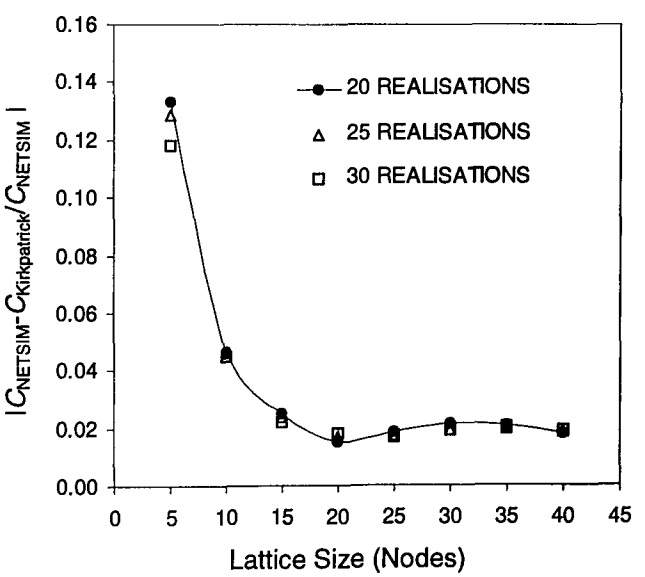

Figure 6.4.1 A plot of absolute difference between the outputs obtained for simulations on ISONETSIM and Kirkpatrick's equation as a function of lattice size at 20-30 realisations.

It was found that the average levelled out to a constant value after the twentieth realisation for all the lattice sizes, with the overall error at this realisation being 10% on a 5^3 lattice. This difference gradually fell with increasing lattice size, until it reached a consistent 2% error on the 30^3 lattice, with virtually no improvement for simulations run on a lattice containing 40^3 nodes. The processing time for this size of lattice was of the order of a few minutes, and in view of this it was considered reasonable to run the isotropic simulations of the UKCS and St. Bees data with 20 realisations for each dataset on a 30^3 lattice, using the average at the twentieth realisation as the final value.

Additional issues relating to the prescribed lattice size, although relatively minor, are the various operational factors concerning the preprocessing of the initial datafile before it can be inputted into the network code. In general, the external input file will not contain enough data to decorate a cubic lattice specified by 30^3 nodes. Consequently, these files need to be expanded to a sufficient number of conductances. As each file contains a different amount of data, it was decided not to expand these input files by multiplying the amount of data by a constant factor, since it was uncertain if this number would be sufficient to account for a particularly sparse file entering the analysis. Instead the file was expanded by an amount equal to

$$\lambda = \left\lceil \frac{3n^2(n+1)}{N} \right\rceil, \qquad (6.4.2.1)$$

where $3n^2(n + 1)$ is the number of *bonds* on the lattice, as a function of n, the number of nodes per lattice direction, and N the number of conductances in a given file. The "$\lceil \cdot \rceil$" notation refers to the rounding up of this quotient to the next highest integer ensuring there are just a sufficient number of conductances to decorate the lattice. The expansion of the initial text file by the factor λ is straightforward and entails inputting the data into a routine that outputs the data λ times. Before this file can be input into a network simulation, it is randomised using a library routine to create a first realisation.

The effect of this preprocessing was found not to generate differences greater than 1% when the initial file was expanded by a multiplier other than the λ factor. However, in the spirit of developing a computationally efficient procedure that avoids unnecessary data handling, and to develop a constant methodology, it was decided that the procedure of using a λ factor should remain part of the preprocessing.

6.4.3 Isotropic Network Models and a Generalised Perturbation Ansatz

Gelhar and Axness (1983) suggested the following expression for the isotropic effective permeability for a heterogeneous aquifer with a lognormal permeability distribution in three dimensions:

$$K_{eff} = K_{geo} e^{\sigma^2_{\ln K}/6}, \tag{6.4.3.1}$$

where K_{geo} is the geometric mean of the permeability distribution, and $\sigma^2_{\ln K}$ denotes the log permeability variance. This equation has been called the Generalised Perturbation Ansatz (GPA). No rigorous proof for its validity is available, although a perturbation expansion to the second order exists (*Dagan,* 1979) that agrees with the Taylor series expansion of (6.4.3.1) to the first term:

$$K_{eff} \approx K_{geo}\left[1+\frac{\sigma^2_{\ln K}}{6}\right]. \tag{6.4.3.2}$$

Hristopulos and Christakos (1999) also argued for the validity of (6.4.3.1), using a diagrammatic analysis of the permeability distribution.

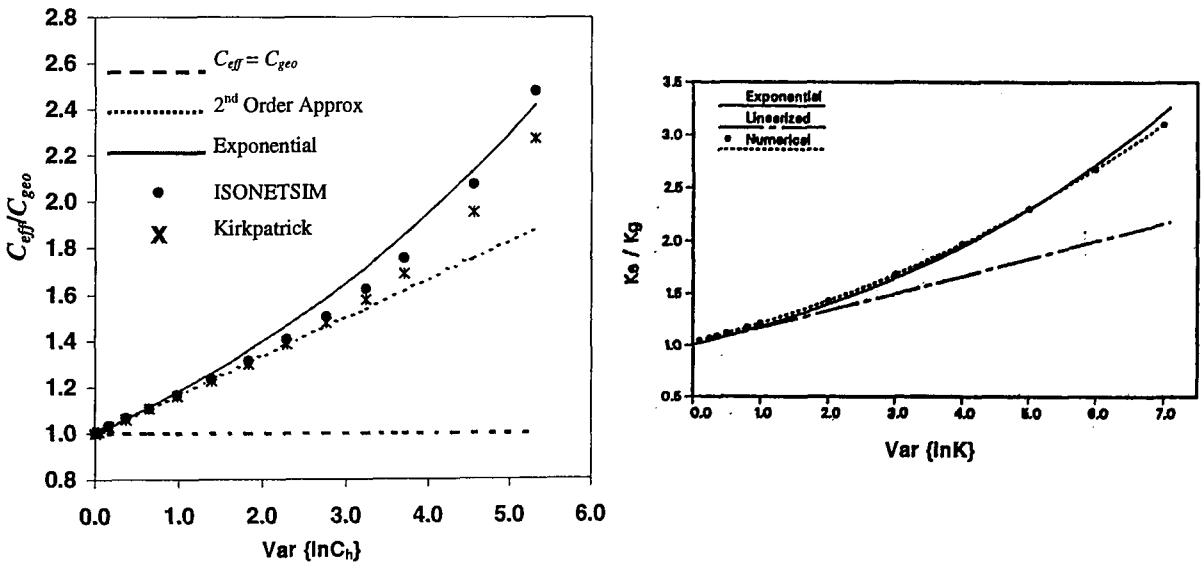

Figure 6.4.2 A comparison of ISONETSIM and Kirkpatrick's effective-medium approximation against the GPA (left); comparison of GPA with the finite-difference simulations of *Neuman et al.* (1992), shown right.

Neuman et al. (1992) conducted flow simulations on a finite-element grid for a set of lognormal permeability distributions with successively increasing variance, and discovered that the exponential expression (6.4.3.1) agreed very well with the numerical results for variances up to 7.0. The second-order approximation, however, rapidly became invalid for variances much greater than 2.0 (Figure 6.4.2).

It was decided to similarly assess the accuracy of the effective conductance obtained for lognormal distributions of different variances using Kirkpatrick's isotropic effective medium equation, ISONETSIM, and the GPA given by (6.4.3.1). The procedure for conducting the simulations has been outlined in the previous section. Lognormal distributions generated for variances ranging from 0 to 5.31 were made by modification to a library routine that outputs a normal distribution for a user-defined mean and variance (*Press et al.,* 1992). Figure 6.4.2 compares the results obtained with those of *Neuman et al.* (1992). The agreement between ISONETSIM and Kirkpatrick's equation is reasonable for sufficiently low variances. However, the difference approaches 10% after a log variance of 5.0. As it is expected that ISONETSIM will provide an essentially exact solution to the conductance problem, the "drift" in the output from the effective medium simulations can be attributable to the increasing broadness of the distribution, since the self-consistent solution is valid when network perturbations are averaged out over a sufficiently narrow range of conductance values. The close proximity of the GPA with the ISONETSIM simulations is in agreement with the findings of *Neuman et al.* (1992) using finite element simulation.

Finally, plotting the linearised version of the GPA (*i.e.*, eq. 6.4.3.2) shows similar behaviour in our comparisons with ISONETSIM and Neuman's comparisons using finite-grid simulations, where the proximity of the linearised solution to the essentially exact solution becomes progressively worse as the log variance increases.

6.5 Simulation of Anisotropic Networks using ANISONETSIM

The flow simulations performed thus far with ISONETSIM only require successive realisations of a *single* input file to populate a cubic network of pore tubes. Consequently, the program has been used as a model of flow in isotropic media which we would like to extend to modelling flow which will reflect the directional properties of the input data. In order to achieve this, we prepare three input files containing the data of directional hydraulic conductances for each of the lattice directions. The

boundary conditions specified are identical with those defined during the isotropic simulations. However, the order (or direction) in which the input files are assigned to the lattice are interchanged to provide output conductances for the x, y, and z directions, respectively.

The major operational issues have already been dealt with in developing a robust procedure for running isotropic network simulations, but nevertheless some slight modifications must be made to the method to allow its application to anisotropic systems. Equation (6.4.2.1) defined a λ factor, based on the total number of nodes on a cubic lattice, that allowed the appropriate expansion of an initial file so that it contains sufficient data to decorate a 30^3 lattice. This factor may be reduced, since the input files now only have to be large enough to decorate the bonds lying along a specified direction. Consequently, λ is then based on a third of the total number of nodes on the lattice, so this factor for an anisotropic simulation becomes $\lambda/3$. This modification was applied to a single input file, in which three random realisations were generated for three different directions. These were then expanded according to the factor $\lambda/3$ for a 30^3 node lattice, and then 20 sequential realisations of this expanded file generated for output into the anisotropic network code, ANISONETSIM. For comparison against the solution obtained using ISONETSIM, the same set of input data was similarly pre-processed, using an expanding factor of $\lambda/3$ to generate three independent inputs. It was found that the final average outputs using ANISONETSIM differed by no more than 0.5% from the isotropic simulations. Also, the outputs obtained when applying the pressure potential in each of the x, y and z directions in the anisotropic simulations were found to differ by less than 0.2%.

7 CALCULATIONAL PROCEDURE AND RESULTS

7.1 Introduction

The various stages of the permeability estimation procedure that have already been discussed are now collected, and applied to some thin section data. The final step in the analysis involves estimating the permeability of the continuous medium from the effective conductance of the individual conductors.

As all the simulations are based on flow on a cubic lattice, consider a plane that slices the lattice perpendicular to one of the principal lattice directions, containing N pores in a region of cross-sectional area A. The total flowrate through this region will be given by

$$Q = \frac{NC_{eff}\Delta p}{\eta L}. \tag{7.1.1}$$

Darcy's law, on the other hand, expresses the flowrate as

$$Q = \frac{kA\Delta p}{\eta L}. \tag{7.1.2}$$

Equating (7.1.1) and (7.1.2) then gives the permeability as

$$k = \frac{NC_{eff}}{A_{total}}. \tag{7.1.3}$$

7.2 Overall Procedure for Estimating the Effective Permeability

The first step in the analysis is the estimation of the apparent area and perimeter of each individual pore that can be recognised in the image. The application of the stereological correction factor of 3/8 (eq. 5.2.2.13) yields the actual area and perimeter values, from which the pore conductivity can be determined. The sinusoidal hydraulic constriction factor of 0.44 (eq. 5.3.2.4) is then applied to account for variations in pore radius along the pore length. The resulting set of conductances is truncated to eliminate the contribution of features that are thought to represent either artefacts of the image processing, or isolated micropores. As each set of data is composed of five BSEIs, the five truncated sets of hydraulic conductance data are then combined, provided that each truncation does not result in the loss of more than 3% of the total hydraulic conductance of that individual datafile. If this criterion is not met, the datafile is rejected. The

combined data is considered to form a statistically representative set of pores for each core, and is input into a network model to produce an effective pore conductance, C_{eff}. When using an intrinsically isotropic network model, data only from that face of the cubic sample that is normal to the flow is used as input. When running an anisotropic simulation, data from three orthogonal faces are used.

The permeability is then calculated, after using another stereological correction to convert the apparent number density of pores in the field of the image to the actual density perpendicular to the flow direction by dividing equation (7.1.3) by the factor 1.47. The complete procedure can be summarised as follows:

- Take BSEI photographs of polished sections
- Digitise pore images
- Apply gray-level thresholding procedure to identify the "pores"
- Compute perimeter and area of each pore with image analyser
- Apply stereological correction and hydraulic constriction factors to estimate the hydraulic conductivity C_i of the individual pores
- Employ areal thresholding procedure to truncate the data set
- Obtain C_{eff} using the effective-medium approximation
- Compute the areal density of pores inside the image
- Assuming a cubic lattice, calculate k using

$$k = \frac{NC_{eff}}{1.47A_{total}}. \tag{7.2.1}$$

7.3 Isotropic Network Theories

Permeabilities were estimated for each set of orientated thin sections belonging to each of the separate cores, using Kirkpatrick's effective-medium approximation in accordance with the procedure outlined above. Table 7.3.1 lists the predicted permeabilities of the UKCS and St. Bees data, compared with the values measured in the laboratory.

Table 7.3.1 Compilation of results for the UKCS and St. Bees cores.

CORE	C_{eff} (m^4)	No. of pores	No. of images	Total area (m^2)	k_{pred} (mD)	$k_{measured}$ (mD)	Error (%)
1X	1.14×10^{-21}	3495	2	1.52×10^{-5}	29	18	59
1Y	2.42×10^{-21}	7397	5	3.80×10^{-5}	52	18	191
2X	41.16×10^{-21}	1843	5	3.80×10^{-5}	222	137	62
2Y	34.43×10^{-21}	1244	3	2.28×10^{-5}	209	119	76
2Z	57.26×10^{-21}	1579	5	3.80×10^{-5}	265	109	143
3X	29.25×10^{-21}	2310	5	3.80×10^{-5}	198	202	-2
3Y	22.56×10^{-21}	2652	5	3.80×10^{-5}	175	196	-11
3Z	23.53×10^{-21}	2600	5	3.80×10^{-5}	179	222	-19
4X	9.17×10^{-21}	3229	5	3.80×10^{-5}	87	83	4
4Y	5.28×10^{-21}	2876	4	3.04×10^{-5}	56	72	-23
4Z	2.66×10^{-21}	1785	2	1.52×10^{-5}	35	28	25
5X	39.43×10^{-21}	1656	4	3.04×10^{-5}	239	470	-49
5Z	51.28×10^{-21}	1829	5	3.80×10^{-5}	275	500	-45
6X	26.75×10^{-21}	2394	5	3.80×10^{-5}	188	275	-32
6Z	27.77×10^{-21}	1854	4	3.04×10^{-5}	189	228	-17
7X	9.08×10^{-21}	3605	5	3.80×10^{-5}	96	109	-12
7Y	10.62×10^{-21}	2448	4	3.04×10^{-5}	95	109	-13
7Z	14.43×10^{-21}	2179	4	3.04×10^{-5}	115	69	66
XB	26.54×10^{-22}	1632	4	10.38×10^{-5}	507	674	-25
XT	11.72×10^{-22}	2726	5	12.93×10^{-5}	300	674	-56
YB	34.12×10^{-22}	1850	5	12.93×10^{-5}	593	1377	-57
YT	16.57×10^{-22}	2605	5	12.93×10^{-5}	405	1377	-71
ZT	37.50×10^{-22}	1642	5	12.93×10^{-5}	576	1046	-45
ZB1	44.97×10^{-22}	1368	5	12.93×10^{-5}	576	1046	-45
ZB2	20.33×10^{-22}	2159	5	12.93×10^{-5}	411	1046	-61

The first eighteen entries correspond to the UKCS samples, the notation giving a core identifier and thin section number, where the "X,Y,Z" labels refer to the direction that lies perpendicular to the slice of the thin section. The remaining entries belong to the St. Bees dataset, where again the "X,Y,Z'' notation refers to the direction that lies

perpendicular to the thin section. The additional "B" or "T" denotes ''top'' and ''bottom'' respectively, and indicates the end of the core plug from which the endtrim was taken with respect to the drilling tool. There are two ZB endtrims, because extra material was recovered in the drilling process, and it was decided to admit this into the analysis. Permeabilities are given in Darcy units, defined by 1 Darcy = 0.987 x 10^{-12} m^2.

The predictions are within a factor of two of the measured values in almost every case. There seems to be a slight trend of overprediction in the low permeability range, and underprediction in the high permeability range, although this bias may be due to the small number of samples. If absolute values are considered, the average error is 48%. Figure 7.3.1 shows a cross-plot of the predicted permeability against the laboratory measurements, for both the UKCS and St. Bees data, with lines that indicate errors of a factor of two in either direction.

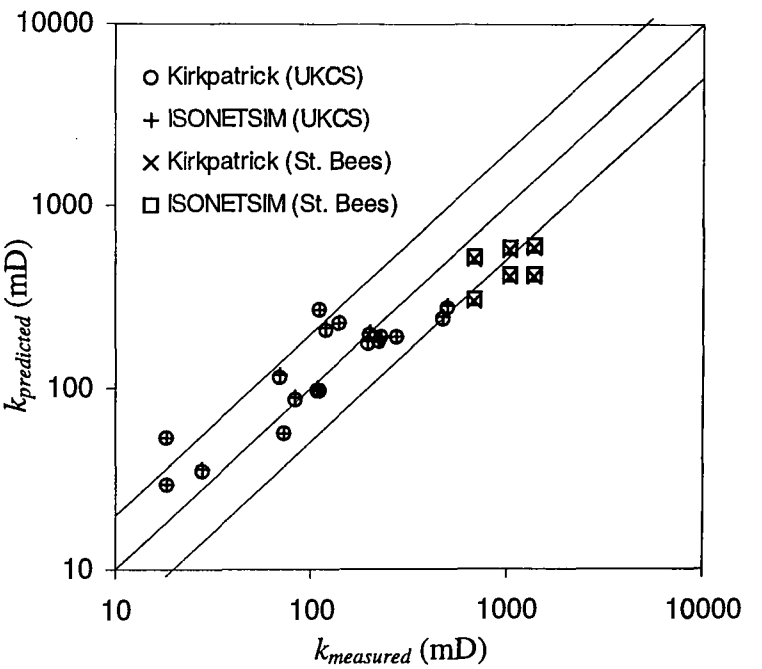

Figure 7.3.1 Measured permeabilities plotted against predicted values for both UKCS and St. Bees data. The upper and lower lines correspond to errors of a factor of two in either direction.

The method, although based on an inherently isotropic model, gives qualitative indications of anisotropy, provided that the measured anisotropy is large enough to exceed the "error bars" of the measurements. If we assume that each permeability measurement has an error of about 30%, two orthogonal permeability measurements

should differ by at least 60% in order for the core to be considered unambiguously anisotropic. By this criterion, the only unambiguously anisotropic core is 4-XYZ, which has a measured anisotropy of about {6:5:2}, and a predicted anisotropy of {5:3:2}. In this case, not only were each of the three principal permeabilities predicted to within 25%, but the ordering of the permeabilities was also predicted quite accurately. The permeability anisotropy ratio of the St. Bees sample, based on the measured permeabilities, is {2:4:3}, which is probably insufficient to indicate that the sample is indeed anisotropic. For comparison, it should be noted that previous isotropic network models that utilised two-dimensional imaging, such as that of *Koplik et al.* (1984), overpredicted the permeability by about a factor of ten.

The use of the Kirkpatrick equation to estimate the effective conductivity was tested against the network simulation code ISONETSIM (*Jing,* 1990). This test was thought to be necessary, because previous studies of the validity of the Kirkpatrick equation have all been based on idealised conductivity distributions (*David et al.*, 1990). Reassuringly, we found that the effective medium predictions agreed to within a few percent with the exact network calculations. If the permeablity predictions for the UKCS and St. Bees data using ISONETSIM are plotted against the predictions using Kirkpatrick's eqution, the agreement between them is clearly indicated (Figure 7.3.2).

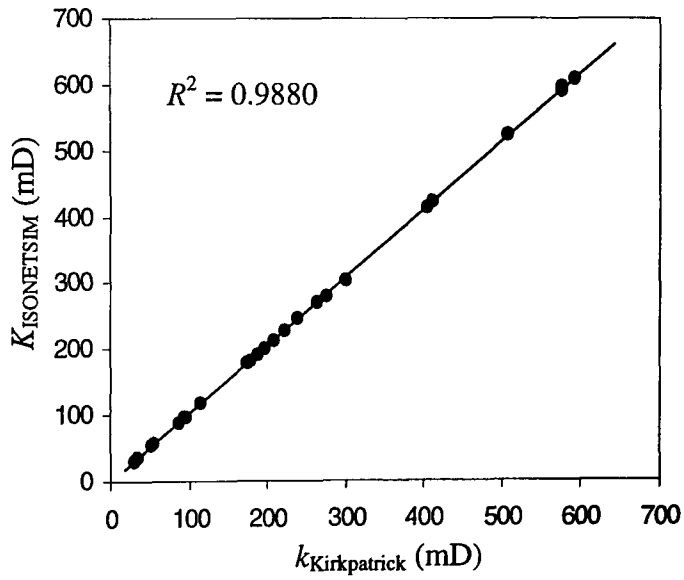

Figure 7.3.2 A cross-plot of the permeability calculated using ISONETSIM against the permeability calculated using Kirkpatrick's equation.

This result is somewhat surprising, in that Kirkpatrick's equation seems to be capable of yielding values comparable to those obtained using an exact network calculation, for sets of individual conductances whose values typically ranges over at least two orders of magnitude, whereas it is usually considered that effective-medium approximations are valid only for a narrow range of conductances. However, if we recall the comparison of ISONETSIM, Kirkpatrick's equation and the Generalised Perturbation Ansatz (Section 6.4.3) using idealised lognormal distributions, the agreement between ISONETSIM and Kirkpatrick's equation was reasonable for logvariances approaching 5.0, beyond which a "drift" in the effective-medium value became gradually more significant. The relationship between the variance in the hydraulic conductivity σ_C^2 of mean μ_C, and the log hydraulic conductance variance, $\sigma_{\ln C}^2$ for a lognormal distribution is (*Till*, 1974)

$$\frac{\sigma_C^2}{\mu_C^2} = [e^{\sigma_{\ln C}^2} - 1]. \qquad (7.3.1)$$

An examination of the statistics for UKCS datasets 1X and 5Z from the low permeability and high permeability ranges of the entire data set show σ_C^2 / μ_C^2 values of 18.62 and 9.59, respectively. From equation (7.3.1), these variances correspond to $\sigma_{\ln C}^2$ values of 2.36 and 2.98.

A histogram of the conductances of the individual pores from one thin section is shown in Figure 7.3.3. This figure not only illustrates the wide range of values over which the effective conductance must be derived, but also indicates that the data is distributed approximately in a lognormal form. If the data follows a lognormal distribution, it can be seen from Figure 7.3.2 that the difference between an exact network calculation and Kirkpatrick's equation, for values of the logvariance in the range 2-3, is only a few percent. Consequently, it is to be expected that the effective-medium approximation is fairly accurate for these distributions. In fact, if we study the comparison of the effective medium approximation against ISONETSIM and the Generealised Pertubation Ansatz (*Gelhar and Axness*, 1983) that was undertaken in Section 6.4.3, it can be considered that Kirkpatrick's equation remains valid for idealised distributions with log variances up to 5.0, when the difference between Kirkpatrick's prediction and ISONETSIM remain within 10%. This in effect quantifies the meaning of "sufficiently narrow distributions".

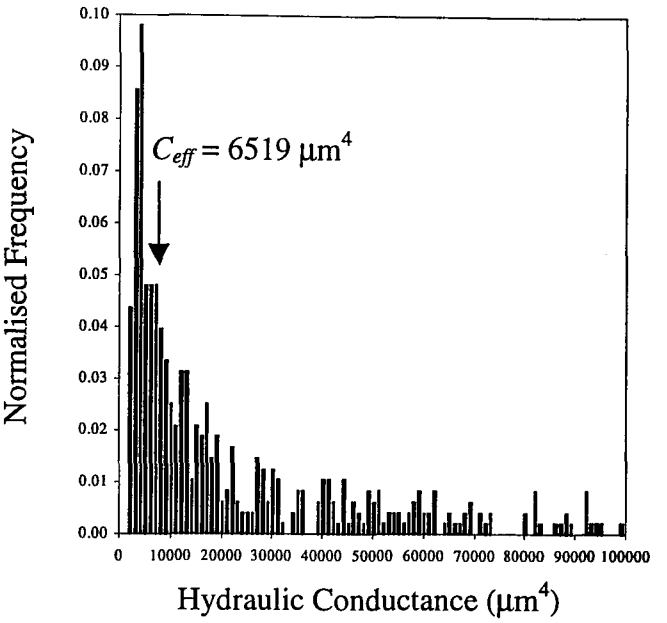

Figure 7.3.3 A histogram of hydraulic conductances obtained for a single thin section *after* filtering the data using the areal truncation described in Section 4.8. Note that the individual conductances C_i range over two orders of magnitude.

7.4 Anisotropic Network Approaches

It was thought that the use of an inherently *anisotropic* effective-medium model such as that of *Bernasconi* (1974) might lead to an improvement in the permeability predictions. The three-dimensional version of the anisotropic effective-medium theory was then applied to fifteen samples that had data corresponding to three orthogonal directions (Table 7.4.1). The results show that the permeability estimations made using the Bernasconi model were only slightly different from those using the Kirkpatrick equation. Furthermore, an "exact" anisotropic calculation using ANISONETSIM failed to make any substantial changes to the predictions made using Kirkpatrick's isotropic effective-medium approximation.

Table 7.4.1 Tabulation showing the permeabilities calculated using Bernasconi's EMA.

CORE	C_{eff} (m^4)	No. of pores	No. of images	Total area (m^2)	k_{pred} (mD)	$k_{measured}$ (mD)	Error (%)
2X	42.03×10^{-21}	1843	5	3.80×10^{-5}	227	138	65
2Y	37.51×10^{-21}	1244	3	2.28×10^{-5}	228	119	92
2Z	51.06×10^{-21}	1579	5	3.80×10^{-5}	236	109	117
3X	27.60×10^{-21}	2310	5	3.80×10^{-5}	187	203	-8
3Y	23.54×10^{-21}	2652	5	3.80×10^{-5}	183	196	-7
3Z	24.08×10^{-21}	2600	5	3.80×10^{-5}	184	222	-18
4X	7.40×10^{-21}	3229	5	3.80×10^{-5}	70	83	-16
4Y	5.28×10^{-21}	2876	4	3.04×10^{-5}	56	72	-23
4Z	3.48×10^{-21}	1785	2	1.52×10^{-5}	46	28	63
7X	9.99×10^{-21}	3605	5	3.80×10^{-5}	104	109	-4
7Y	10.85×10^{-21}	2448	4	3.04×10^{-5}	97	109	-11
7Z	13.16×10^{-21}	2179	4	3.04×10^{-5}	105	69	51
XB	29.07×10^{-22}	1632	4	10.38×10^{-5}	555	674	-18
YB	33.44×10^{-22}	1850	5	12.93×10^{-5}	581	1377	-58
ZT	35.18×10^{-22}	1642	5	12.93×10^{-5}	541	1046	-48

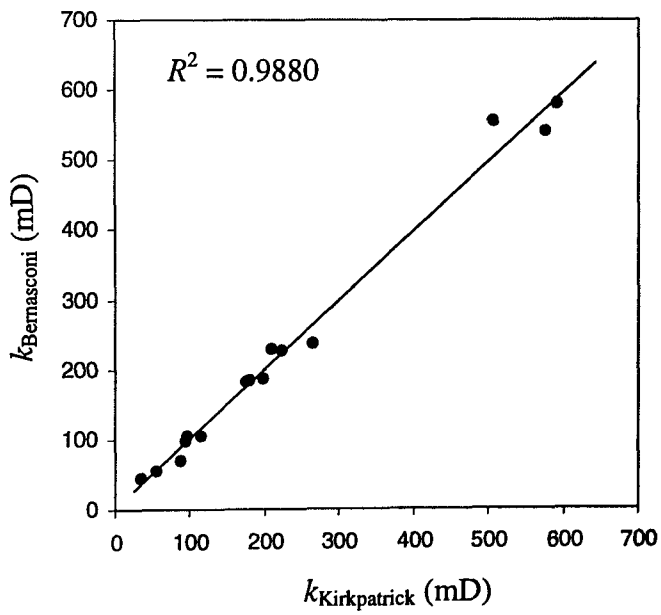

Figure 7.4.1 A crossplot of permeability calculated using Bernasconi's equation against permeability obtained using Kirkpatrick's isotropic model.

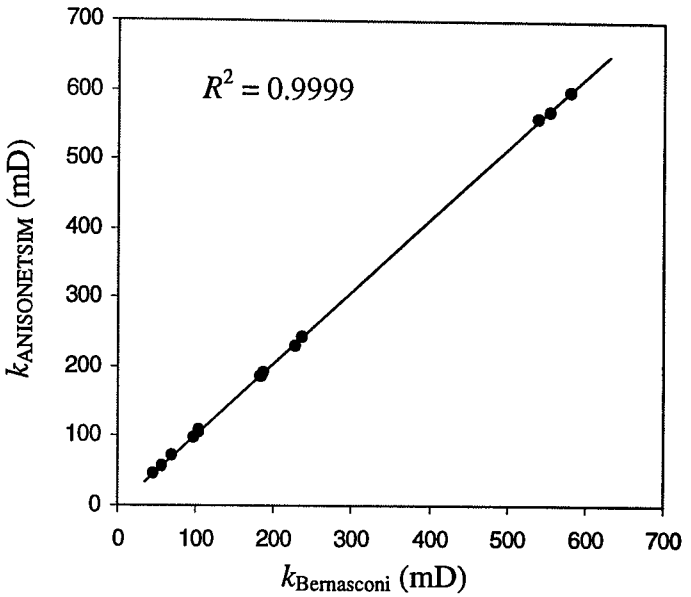

Figure 7.4.2 A crossplot of permeability calculated using ANISONETSIM against permeability calculated using Bernasconi's equation.

A comparison of the simulations using Kirkpatrick's isotropic EMA, Bernasconi's anisotropic EMA, and ANISONETSIM was made using the square of Pearson's R coefficient to assess the correlation between two sets of predictions. The average absolute error in the isotropic effective medium prediction for these fifteen samples is 38%. A comparison of the absolute errors from the anisotropic effective medium approximation and ANISONETSIM gave errors of 39% and 38%, respectively, indicating that the use of more sophisticated simulation methods beyond that of Kirkpatrick fails to produce any systematic improvements of the predictions.

The above analysis indicates that there is no systematic improvement in the predictions obtained using an anisotropic network model in place of Kirkpatrick's inherently isotropic effective-medium approximation, with the predictions remaining within a factor of two of the laboratory measurements. Furthermore, the lack of any systematic improvement when using an anisotropic network model is also reflected in the failure to improve on the indications of anisotropy that were obtained using the isotropic effective-medium approximation. The differences in the directional permeabilities amongst the cores, especially the UKCS core 4-XYZ, in fact appear to become smaller. This reduction of the anisotropy ratio is attributable to the fact that

simulations performed using either Bernasconi's effective-medium or the ANISONETSIM scheme couple data taken at different orientations and so the prediction of permeability in one direction will include the influences of the pore conductances in the other two directions and vice-versa.

Table 7.4.2 Permeabilities obtained using ANISONETSIM.

CORE	C_{eff} (m^4)	No. of pores	No. of images	Total area (m^2)	k_{pred} (mD)	$k_{measured}$ (mD)	Error (%)
2X	42.76×10^{-21}	1843	5	3.80×10^{-5}	231	138	68
2Y	37.91×10^{-21}	1244	3	2.28×10^{-5}	230	119	94
2Z	52.57×10^{-21}	1579	5	3.80×10^{-5}	243	109	123
3X	28.24×10^{-21}	2310	5	3.80×10^{-5}	191	203	-6
3Y	23.99×10^{-21}	2652	5	3.80×10^{-5}	187	196	-5
3Z	24.49×10^{-21}	2600	5	3.80×10^{-5}	187	222	-16
4X	7.65×10^{-21}	3229	5	3.80×10^{-5}	72	83	-13
4Y	5.39×10^{-21}	2876	4	3.04×10^{-5}	57	72	-22
4Z	3.47×10^{-21}	1785	2	1.52×10^{-5}	45	28	63
7X	9.96×10^{-21}	3605	5	3.80×10^{-5}	105	109	-3
7Y	11.02×10^{-21}	2448	4	3.04×10^{-5}	99	109	-9
7Z	13.49×10^{-21}	2179	4	3.04×10^{-5}	108	69	55
XB	29.81×10^{-22}	1632	4	10.38×10^{-5}	569	674	-16
YB	34.53×10^{-22}	1850	5	12.93×10^{-5}	600	1377	-57
ZT	36.48×10^{-22}	1642	5	12.93×10^{-5}	561	1046	-46

The permeabilities obtained using Bernasconi's EMA and those obtained from an exact network calculation using ANISONETSIM are plotted in Figure 7.4.3, along with the predictions obtained using Kirkpatrick's equation, against the laboratory measurements.

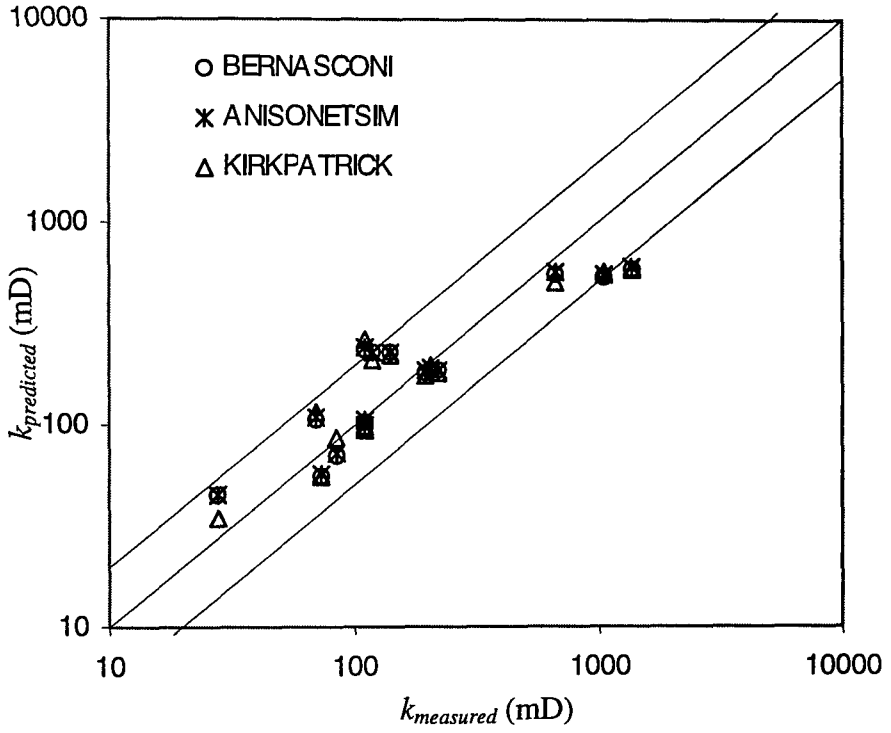

Figure 7.4.3 A comparison of the permeability predictions using Kirkpatrick's isotropic EMA, Bernasconi's EMA, and exact network calculations using ANISONETSIM.

8 CONCLUSIONS AND SUGGESTIONS FOR FUTURE WORK

In this thesis, a methodology has been developed that allows predictions of the hydraulic permeability of consolidated sedimentary rocks such as sandstones, based on image analysis of polished sections of a rock core sample. For the rocks analysed in this study, the method sometimes overpredicts and sometimes underpredicts the measured permeability, with an (absolute value) error that is on average only 48%. To put this in perspective, we should compare this to the errors inherent in the measured values. *McPhee and Arthur* (1994) reported the results of a series of gas permeability measurements on a Clashach quarried sandstone, with an average permeability of 693 mD, and found an "error" of 32%, based on the standard deviation of all the measurements. Although these values are not directly comparable, the mean (absolute) relative error in our measurements seems to be comparable to the error inherent in the laboratory measurements.

It should be emphasized that our model is based entirely on measured attributes of the pore space. Although there are adjustable parameters in our algorithm, such as co-ordination number and the ratio of minimum-to-maximum pore radius, these have been taken to have the same values for all cores. Likewise, the various stereological corrections are performed in the same manner for all cores. Hence, the numerical values of the permeability predictions contain no adjustable parameters whatsoever.

The question may be raised as to why our estimates are so much more accurate than those made by Koplik *et al.* (1984), using a broadly similar procedure. There are, however, several differences between the two methods. For example, they estimated pore conductances using the concept of "equivalent ellipse", whereas we used the hydraulic radius approximation. Based on comparisons with BEM simulations (*Koplik et al.*, 1984; *Sisavath et al.*, 2000), however, it seems that this difference may account for at most an error of about 10-50% in their predictions. The main difference seems to be our inclusion of the constriction factor and the stereological correction factors for pore size and number density, each of which lower the estimated pore conductance by about a factor of two. Taken together, the absence of these corrections may explain why their estimates were too high by about an order of magnitude.

Although the estimates of k nearly always fall within a factor of two of the measured values, there is a tendency to overpredict permeability at the lower range, and underpredict for the more permeable cores. Any errors in estimating the conductivity of individual pores should be independent of the absolute permeability, so these factors cannot explain the trend. One possible explanation may involve our use of a co-ordination number of six for all cores. The recent work by *Lindquist et al.* (2000) implies that we might expect a positive correlation between permeability and co-ordination number. At the high permeability range, the underprediction may be attributable to an insufficiently high co-ordination number in our permeability model. Conversely, at the low permeability range of the data, the overprediction may be a result of using too high a co-ordination number. It is therefore possible that a more accurate estimation of co-ordination number would further improve the accuracy of our permeability model.

The use of essentially *exact* isotropic network calculations fail to produce any systematic improvement on the predictions obtained using the isotropic effective medium theory of Kirkpatrick since the logvariance of the conductance distributions are not sufficient to produce a substantial difference in the predictions obtained by the two simulation methods. Furthermore, the lack of any systematic improvement when using an anisotropic network model, for example consider the UKCS core 4-XYZ, reflects the fact that the cases studied here are perhaps insufficiently anisotropic for either Bernasconi's equation or anisotropic NETSIM to make a notable difference in the predictions.

The inability to find sufficiently anisotropic samples to test the inherently anisotropic network codes highlights the fact that anisotropy variations are not likely to be pronounced at the pore scale, but become increasingly significant as the scale of the measurement is increased. Permeability anisotropy will become a significant issue at the field scale, where directional preferences for fluid flow are attributable to heterogeneities such as sand/shale sequences *Bernabé* (1992). The manufacture of a synthetic porous material with a large degree of permeability anisotropy may be possible, and allow a more extensive test of the anisotropic network models used in this study. Presently, however it would seem that a permeability model based on Kirkpatrick's isotropic effective-medium approximation suffices to give a permeability prediction to within a factor of two, with a qualitative indication of anisotropy.

The method developed has thus far only been applied to predictions of single-phase permeabilities in relatively homogeneous materials such as sandstones. An extension of the model to predicting the single-phase permeability characteristics in other rock types would be worthwhile. Carbonates, known for their heterogeneity, are of particular interest to the petroleum industry, as a significant amount of the world's hydrocarbon reserves are located in carbonate formations. To extend the present method to such rock types would require a reconsideration of the data acquisition and image analysis procedures. Owing to the relatively more complex pore structure of carbonates, with features extending over a wider range of scales, BSEIs would have to be collected from a range of magnifications in order to capture all the relevant characteristics of the pore space. Combining the data to obtain a valid representation of the flow characteristics would probably require modifications to the areal thresholding procedure that has been developed, and also inclusion of statistical analyses exceeding that performed in this study. The heterogeneity might produce hydraulic conductance distributions with variances large enough to introduce substantial differences between network simulations using the isotropic effective medium approximation and NETSIM.

A natural extension of this work is the development of an effective medium model for two-phase flow through reservoir rocks, using data obtained from thin sections. *Levine and Cuthiell* (1986) developed an effective-medium model of two-phase flow on a cubic lattice by assuming a water-wet rock that could be described by an *idealised* pore-size distribution which was partitioned so that pores below a certain size would only allow the presence of a water film. Above this "threshold", the pores will admit the oil phase, flowing on top of the pre-existing water film. Hence, the work of *Levine and Cuthiell* (1986) on two-phase flow using the effective medium approximation of Kirkpatrick seeks to obtain two-phase relative permeabilities by separating the flow tubes according to a pre-defined size criterion to account for wettability. However, the method does not consider the simultaneous flow of oil and water through the pores. Although the theory was extended to include the possible dependence of the relative permeabilities on the ratio of the viscosity of fluids that can co-exist inside a pore tube, no numerical results were presented. The use of greyscale identification of the pore wall mineralogy could provide a direct method for determining the initial wettability state of the rock, and possibly lead to the development of a method that could successfully consider simultaneous flow of oil and water, under conditions of mixed wettability.

REFERENCES

Adler, P. M., Transport processes in fractals VI. Stokes flow through Sierpinski carpets, *Phys. Fluids*, Vol. 29, pp. 15-22, 1986.

Adler, P. M., *Porous Media: Geometry and Transports,* Butterworth–Heinemann, Boston, 1992.

Adler, J., Jacquin, C. G., and Quiblier J. A., Flow in Simulated Porous Media, *Int. J. Multiphase Flow*, Vol. 16, pp. 691-712, 1990.

Al-Harthy, S. S., *Laboratory Investigation of Petrophysical Properties of Sandstone Rocks Under True Triaxial Stress*, Ph.D. Thesis, Imperial College, University of London, 1999.

Ambegaokar, V., Halperin, B. I., and Langer, J. S., Hopping conductivity in disordered systems, *Phys. Rev. B*, Vol. 4, pp. 2612-2620, 1971.

Basan, P. B., Whattler, P. R., Lowden, B. D., and Attard. J. J., Pore-size data in petrophysics: a perspective on the measurement of pore geometry, in *Developments in Petrophysics*, Geological Society Special Publication 122, pp. 47-67, edited by M. A. Lovell and P. K. Harvey, Geological Society, London, 1997.

Bear, J., *Dynamics of Flow in Porous Media,* Elsevier, New York, 1972.

Bentz, D. P., and Martys, N. S., Hydraulic radius and transport in reconstructed model three-dimensional porous media, *Transp. Porous Media,* Vol. 17, pp. 221-238, 1994.

Berkowitz, B., and Balberg, I., Percolation theory and its application to groundwater hydrology, *Water Resour. Res.*, Vol. 29, pp. 775–794, 1993.

Berkowitz, B., and Ewing, R. P., Percolation theory and network modeling. Applications in soil physics, *Surv. Geophys.*, Vol. 19, pp. 23–72, 1998.

Bernabé, Y., On the measurement of permeability in anisotropic rocks, in *Fault Mechanics and Transport Properties in Rocks: a Festschrift in honour of W. F. Brace*, pp. 148-167, edited by B. Evans and T. -F., Wong, Academic Press, London, 1992.

Bernabé, Y., and Olson, J. F., The hydraulic conductance of a capillary with a sinusoidally varying cross-section, *Geophys. Res. Lett.*, Vol. 27, pp. 245-248, 2000.

Bernasconi, J., Conduction in anisotropic disordered systems: effective medium theory, *Phys. Rev. B*, Vol. 9, pp. 4575-4579, 1974.

Berryman, J. G., Relationship between specific surface area and spatial correlation functions for anisotropic porous media, *J. Math. Phys.*, Vol. 28, pp. 244-245, 1987.

Berryman, J. G., and Blair, S. C., Use of digital image analysis to estimate fluid permeability of porous materials, *J. Appl. Phys.*, Vol. 60, pp. 1930-1938, 1986.

Berryman, J. G., and Blair, S. C., Kozeny-Carman relations and image processing methods for estimating Darcy's constant, *J. Appl. Phys.*, Vol. 62, pp. 2221-2228, 1987.

Beyer, W. H., *CRC Standard Mathematical Tables*, 28th ed., CRC Press, Boca Raton, Florida, 1987.

Birks, L. S., *X-Ray Spectrochemical Analysis*, Interscience, London, 1959.

Briggs, D., and Seah, M. P., *Practical Surface Analysis by Auger and X-ray Photoelectron Spectroscopy*, Wiley, Chichester, 1983.

Bourbié, T., Coussy, C., and Zinszner, B., *Acoustics of Porous Media*, Gulf Publishing Company, Houston, 1987.

Boyle, K., Jing, X. D., and Worthington, P. F., Petrophysics, in *Modern Petroleum Technology,* Vol. 1, 6th ed., pp. 131-206, edited by R. A. Dawe, Institute of Petroleum, Wiley, Chichester, 2000.

Broadbent, S. R., and Hammersley, J. M., Percolation processes. I. Crystals and mazes, *Proc. Camb. Phil. Soc.*, Vol. 53, pp. 629–641, 1957.

Cargill, G. S., Radial distribution functions and microgeometry of dense random packings of hard spheres, in *Physics and Chemistry of Porous Media,* pp. 20-36, edited by D. L. Johnson and P. N. Sen, AIP Conference Proceedings, no. 107, American Institute of Physics, New York, 1984.

Carman, P. C., Capillary rise and capillary measurement of moisture in fine sands, *Soil Sci.*, Vol. 52, pp. 1-14, 1941.

Case, C. M., and Cochran, G. F., Transformation of the tensor form of Darcy's law in inhomogeneous and anisotropic soils, *Water Resour. Res.*, Vol. 8, pp. 728-733, 1972.

Castleman, K. R., *Digital Image Processing,* Prentice-Hall, NewYork, 1996.

Chatzis, I., *Network Approach to Analye and Model Capillary and Transport Phenomena in Porous Media*, PhD. Thesis, University of Waterloo, Waterloo, Ontario, 1980.

Chatzis, I., and Dullien, F. A. L., Modelling pore structure by 2–D and 3–D networks with application to sandstones, *J. Canad. Pet. Tech.*, Vol 16, pp. 97-108, 1977.

Chow, C. K., and Kaneko, T., Automatic boundary detection of the left ventricle from cineangiograms, *Comput. Biomed. Res.*, Vol. 5, pp, 388-410, 1972.

Collins, R. E., Determination of the permeabilities of large core samples from petroleum reservoirs, *J. Appl. Phys.*, Vol. 23, pp. 681-684, 1952.

Dagan, G., Models of groundwater flow in statistically homogeneous porous formations, *Water Resour. Res.*, Vol. 15, pp. 47-63, 1979.

Dagan, G., Statistical theory of groundwater flow and transport: pore to laboratory, laboratory to formation and formation to regional scale, *Water Resour. Res.*, Vol. 22, pp. S120-S134, 1986.

Daily, W. D., and Lin, W., Laboratory-determined transport properties of Berea sandstone, *Geophys.*, Vol. 50, pp. 775-784, 1985.

David, C., Gueguen, Y., and Pampoukis, G., Effective medium theory and network theory applied to the transport properties of rock, *J. Geophys. Res.*, Vol. 95, pp. 6993-7005, 1990.

de Gennes, P. G., On a relation between percolation theory and the elasticity of gels, *J. Phys. Lett.*, Vol. 37, pp. L1-L3, 1976.

de Marsily, G., *Quantitative Hydrogeology,* Academic Press, San Diego, 1986.

Debye, P., Anderson, H. R. Jr., and Brumberger, H. J., Scattering by an inhomogeneous solid II. The correlation function and its application, *Appl. Phys.*, Vol. 28, pp. 679-683, 1957.

Delannay, R., *Dispersion de Taylor en Milieux Poreux Fractals* (Taylor Dispersion in Fractal Porous Media), Ph.D. Thesis. Univ. de Paris-IV, Paris, 1990.

Doyen, P. M., Permeability conductivity, and pore geometry of sandstone, *J. Geophys. Res.*, Vol. 93, pp. 7729-7740, 1988.

Dranchuk, P. M., and Tait, R. J., The determination of transverse permeabilities in anisotropic porous media, *J. Canad. Pet. Tech.*, Vol. 20, pp. 100-104, 1981.

Dullien, F. A. L., *Porous Media-Fluid Transport and Structure*, 2nd ed., Academic Press, New York, 1992.

Dullien, F. A. L., and Dhawan, G. K., Bivariate pore-size distributions of sandstones, *J. Interface Colloid. Sci.*, Vol. 52, pp. 129-135, 1975.

Ehrlich, R., Crabtree, S. J., Horkowitz, K. O., and Horkowitz, J. P., Petrography and reservoir physics I: Objective classification of reservoir porosity, *AAPG Bull.*, Vol. 75, pp. 1547-1562, 1991.

Fatt, I., The network model of porous media. I. Capillary pressure characteristics, *Pet. Trans. AIME*, Vol. 207, pp. 144-159, 1956a.

Fatt, I., The network model of porous media. II. dynamic properties of a single size tube network, *Pet. Trans. AIME*, Vol. 207, pp. 160-163, 1956b.

Ferrandon, J., The laws of filtration flow, *Génie Civil.*, Vol. 125, pp. 24-28, 1948.

Ferréol, B., and Rothman, D. H., Lattice-Boltzmann simulations of flow through Fontainebleau sandstone, *Transp. Porous Media,* Vol. 20, pp. 3-20, 1995.

Finney, R. L., and Thomas, G. B., *Calculus,* 2nd ed., Addison-Wesley, Reading, Massachusetts, 1994.

Friedman, S. P., and Seaton, N. A., Critical path analysis of the relationship between permeability and electrical conductivity of three dimensional pore networks, *Water Resour. Res.*, Vol. 34, pp. 1703-1710, 1998a.

Friedman, S. P., and Seaton, N. A., On the transport properties of anisotropic networks of capillaries, *Water Resour. Res.*, Vol. 32, pp. 339-347, 1998b.

Friedman, S. P., and Seaton, N. A., Percolation thresholds and conductivities of a uniaxial anisotropic simple cubic lattice, *Transp. Porous Med.*, Vol. 30, pp. 241-250, 1998c.

Frisch, H. L., and Hammersley, J. M., Percolation processes and related topics, *J. Soc. Ind. Appl. Math.*, Vol. 11, pp. 894-918, 1963.

Gelhar, L. W., and Axness, C. L., Three-dimensional stochastic analysis of macrodispersion in aquifers, *Water Resour. Res.*, Vol. 19, pp. 161-180, 1983.

Gingold, D. B., and Lobb, C., Percolative conduction in three dimensions, *Phys. Rev. B*, Vol. 42, pp. 8220-8224, 1990.

Goggin, D. J., Thrasher, R. L., and Lake, L. W., A theoretical and experimental analysis of minipermeameter response including gas slippage and high velocity flow effects, *In Situ*, Vol. 12, pp. 79-116, 1988.

Graton, L. C., and Fraser, H. J., Systematic packing of spheres - with particular relation to porosity and permeability, *J. Geol.*, Vol. 43, pp. 785-909, 1935.

Guin, J. A., Kessler, D. P., and Greenkorn, R. A., The permeability tensor for anisotropic nonuniform porous media, *Chem. Eng. Sci.*, Vol. 26, pp. 1475-1478, 1971.

Hailwood, E., and Bowen, D., Directional permeability – how important is it and can it be measured reliably?, *Dialog, London Petrophysical Society Newsletter*, Vol. 7, Issue 3, 1999.

Haines, W. H., Studies in the physical properties of soil, 5: The hysteresis effect in capillary properties and the modes of moisture distribution associated therewith, *J. Agr. Sci.*, Vol. 20, pp. 97-116, 1930.

Haring, R. E., and Greenkorn, R. A., A statistical model of a porous medium with non uniform pores, *AIChE J.*, Vol. 16, pp. 477-483, 1970.

Harris, C. C., Lattice square as a network model of random packing, *Nature*, Vol. 205, pp. 353-346, 1965.

Harris, C. K., Application of generalised effective-medium theory to transport in porous media, *Transp. Porous Med.*, Vol. 5, pp. 517-542, 1990.

Harris, C. K., Effective-medium treatment of flow through anisotropic fracture systems-improved permeability estimates using a new lattice mapping, *Transp. Porous Med.*, Vol. 9, pp. 287-295, 1992.

Hatfield, K. L., *Pore Morphology and the Characterisation of North Sea Sandstones*, Ph.D. Thesis, University of Leicester, 1999.

Hestir, K., and Long, J. C. S., Analytical expressions for the permeability of random two-dimensional Poisson fracture networks based on regular lattice percolation and equivalent media theories, *J. Geophys. Res.*, Vol. 95, pp. 21,565-21,581, 1990.

Hristopulos, D. T., and Christakos, G., Renormalisation group analysis of permeability upscaling, *Stochastic Envir. Res. Risk Assessment*, Vol. 13, pp. 131-160, 1999.

Hubbert, M. K., Darcy's law and the field equations of the flow of underground fluids, *Pet. Trans. AIME*, Vol. 207, pp. 222-232, 1956.

Jerauld, G. R., and Salter, S. J., The effect of pore structure on hysteresis in relative permeability and capillary pressure: pore-level modeling, *Transp. Porous Med.*, Vol. 5, pp. 103-151, 1990.

Jezek, J., and Hrouda, F., The relationship between the Lisle orientation tensor and the susceptability tensor, *Phys. Chem. Earth A*, Vol. 25, pp. 469-474, 2000.

Jing, X. D., *The Effect of Clay, Pressure and Temperature on the Electrical and Hydraulic Properties of Real and Synthetic Rocks*. Ph.D. Thesis, Imperial College, University of London, 1990.

Johnson, W. E., and Hughes, R. V., Directional permeability measurements and their significance, *Producers Monthly*, Vol. 13, pp. 17-25, 1948.

Johnson, D. L., and Sen, P. N., Dependence on the conductivity of a porous medium on electrolyte conductivity, *Phys. Rev. B*, Vol. 37, pp. 3502-3510, 1988.

Joyce-Lobel, *Image Analysis, Principles and Practice*, Joyce-Lobel, A Vickers Company, Gateshead, 1985.

Katz, A. J., and Thompson, A. H., Quantitative prediction of permeability in porous rock, *Phys Rev. B*, Vol. 34, pp. 8179-8181, 1986.

Kelton, F. C., Analysis of fractured limestone cores, *Pet. Trans. AIME*, Vol. 189, pp. 225-234, 1950.

Kim, C. S., and Lee, M. H., Monte Carlo renormalisation group studies of anisotropic bond percolation, *Inter. J. Mod. Phys.*, Vol. B6, pp. 1505-1515, 1992.

Kirkpatrick, S., Classical transport in disordered media: Scaling and effective medium theories, *Phys. Rev. Lett.*, Vol. 27, pp. 1722-1725, 1971.

Kirkpatrick, S., Percolation and conduction, *Rev. Mod. Phys.*, Vol. 45, pp. 574-588, 1973.

Koplik, J., Creeping flow in two-dimensional networks, *J. Fluid Mech.*, Vol. 119, pp. 219-247, 1982.

Koplik, J., Lin, C., and Vermette, M., Conductivity and permeability from microgeometry, *J. Appl. Phys.*,Vol. 56, pp. 3127-3131, 1984.

Kruyer, S., The penetration of mercury and capillary condensation in packed spheres. *Trans. Faraday Soc.*, Vol. 54, pp.1758-1767, 1958.

Ksenzhek, O. S., Capillary equilibrium in porous media with intersecting pores, *Russ. J. Phys. Chem.*, Vol. 37, pp. 691-694, 1963.

Landauer, R., The electrical resistance of binary metallic mixtures, *J. Appl. Phys.*, Vol. 23, pp. 779-784, 1952.

Lemaitre, R., and Adler, P. M., Fractal porous media IV. Three-dimensional stokes flow through random media and regular fractals, *Transp. Porous Med.*, Vol. 5, pp. 325-340, 1990.

Levine, S., and Cuthiell, D. L., Relative permeabilities in two-phase flow through porous media: an application of effective medium theory, *J. Canad. Pet. Tech.*, Vol 5, pp. 74-84, 1986.

Lindquist, W. B., and Venkatarangan, A., Investigating 3D geometry of porous media from high resolution images, *Phys. Chem. Earth A*, Vol. 24, pp. 593-599, 1999.

Lindquist, W. B., Venkatarangan, A., Dunsmuir, J., and Wong, T. -F., Pore and throat size distributions measured from synchrotron X-ray tomographic images of Fontainebleau sandstones, *J. Geophys. Res.*, Vol. 105, pp. 21,509-21,527, 2000.

Lisle, R. J., The statistical analysis of orthogonal orientation data, *J. Geol.*, Vol. 97, pp. 2360-364, 1989.

Lu, J., Healy, D. M., and Weaver, J. B., Contrast enhancement of medical images using multiscale edge representation, *Opt. Eng.*, Vol. 33, pp. 1251-2161, 1994.

Mandelbrot, B. B., The *Fractal Geometry of Nature,* Freeman, Oxford, 1982.

Macmullin, R. B., and Muccini, M. A., Characteristics of porous beds and structures, *AIChE J.*, Vol. 2, pp. 393-403, 1956.

Mayer, R. P., and Stowe, R. A., Mercury porosimetry: Breakthrough pressure for penetration between packed spheres, *J. Colloid Sci.*, Vol. 20, pp. 893-911, 1965.

Mayer, R. P., and Stowe, R. A., Mercury porosimetry: Filling of toroidal void volume following breakthrough between packed spheres, *J. Phys. Chem.*, Vol. 70, pp. 3867-3873, 1966.

McCreesh, C. A., Ehrlich, R. and Crabtree, S. J. J., Petrography and reservoir physics II: Relating thin section porosity to capillary pressure, the association between pore types and throat size, *AAPG Bull.*, Vol. 75, pp. 1563-1578, 1991.

McPhee, C. A., and Arthur, K. G., Relative permeability measurements: an inter-laboratory comparison, *SPE paper 28826*, presented at the European Petroleum Conference, London, 1994.

Meyer, H. I., Pore distribution in porous media, *J. Appl. Phys.*, Vol. 24, pp. 510-514, 1953.

Mukhopadhyay, S., and Sahimi, M., Scaling behavior of permeability and conductivity anisotropy near the percolation threshold, *J. Stat. Phys.*, Vol. 74, pp. 1301-1308, 1994.

Neuman, S. P., Orr, S., Levin, O., and Paleogos, E., Theory and high-resolution finite element analysis of 2-D and 3-D effective permeabilities in strongly heterogeneous porous media, in *Computational Methods in Water Resources IX*. Vol. 2, pp. 117-136, edited by T. F. Russell, R. E. Ewing, C. A. Brebbia, W. G. Gray, and G. F. Pinder, Elsevier Applied Science, New York, 1992.

Nicholson, D., and Petropoulos, J. H., Capillary models for porous media III. Two–phase flow in a three dimensional network with Gaussian radius distribution, *J. Phys. D*, Vol. 4, pp. 181-189, 1971.

Normand, J. M., Herrmann, H. J., and Hajjar, M., Precise calculation of the dynamical exponent of two-dimensional percolation, *J. Stat. Phys.*, Vol. 52, pp. 441-451, 1988.

Nutting, P. G., Physical analysis of oil sands, *Bull. Amer. Ass. Petrol. Geol.*, Vol. 14, pp. 1337-1349, 1930.

Nye, J. F., *Physical Properties of Crystals: Their Representation by Tensors and Matrices*, Clarendon Press, Oxford, 1957.

Øren, P. E., and Bakke, S., Process based reconstruction of sandstones and prediction of transport properties, in *Upscaling Downunder: a Symposium and Workshop on Upscaling Reservoir Properties and Related Issues,* pp. 1-33, 7-10 Feb, 2000, Australian Petroleum Cooperative Research Centre, Melbourne, Australia, 2000.

Otsu, N., A threshold selection method from gray-level histograms, *IEEE Trans. Syst. Man. Cyb.*, Vol. 9, pp. 62-66, 1979.

Petruk, W., *Short Course on Image Analysis Applied to Mineral and Earth Sciences,* Mineralogical Association of Canada, Ottowa, May, 1989.

Pilotti, M., Generation of realistic porous media by grains sedimentation, *Transp. Porous Media,* Vol. 33, pp. 257-278, 1998.

Pittman, E. D., The pore geometries of reservoir rocks, in *Physics and Chemistry of Porous Media,* pp. 1-19, edited by D. L. Johnson and P. N. Sen, AIP Conference Proceedings, no. 107, American Institute of Physics, New York, 1984.

Pfleiderer, S., and Halls, H. C., Magnetic susceptibility anisotropy of rocks saturated with ferrofluid: A new method to study pore fabric?, *Phys. Earth Planet. Inter.*, Vol. 65, pp. 158-164, 1990.

Prats, M., The influence of orientated arrays of thin impermeable shale lenses or of highly conductive natural fractures on apparent permeability anisotropy, *J. Pet. Tech.*, pp. 1219-1221, 1972.

Press, W. H., Teukolsky, S. A., Vetterling, W. T., and Flannery, B. P., *Numerical Recipes in Fortran 77*, 2nd ed., Cambridge University Press, 1992.

Priest, S. D., *Discontinuity Analysis for Rock Engineering*, Chapman and Hall, London, 1992.

Purcell, W. R., Capillary pressures-their measurement using mercury and the calculation of permeability therefrom, *Trans. AIME*, Vol.186, pp. 39-48, 1949.

Redner, S., and Stanley, H. E., Anisotropic bond percolation, *J. Phys.* A, Vol. 12, pp. 1267-1283, 1979.

Rice, P. A., Fontugne, D. J., Latini, R. G., and Barduhn, A. J., Anisotropic permeability in porous media, in *Flow Through Porous Media*, pp. 48-56, edited by R. Nunge, American Chemical Society, Washington, D. C., 1970.

Rink, M., and Schopper, J. R., On the application of image analyisis to formation evaluation, *The Log Analyst*, Vol. 19, pp. 12-22, 1978.

Rose, W., A new method to measure directional permeability, *J. Pet. Tech.*, pp. 1142-1144, 1982.

Rothman, D. H., and Zaleski, S., *Lattice-Gas Cellular Automata: Simple Models of Complex Hydrodynamics,* Cambridge University Press, Cambridge, 1997.

Rumpf, H., and Gupte, A. R., Einflüsse der porosität und korngroßenverteilung im widerstandsgesetz der porenströmung (The influence of porosity and particle size distribution in the resisitance law of porous flow), *Chem. Ing. Tech.*, Vol. 43, pp. 367-375, 1971.

Ruzyla, K., Characterisation of pore space by quantitative image analysis, *SPE Paper 93133*, presented at the 59th Annual Technical Conference and Exhibition, Houston, Texas, 1986.

Sahimi, M., *Flow and Transport in Porous Media and Fractured Rock,* VCH Publishers, Weinheim, 1995.

Sahimi, M., Hughes, B. D., Scriven, L. E., and Davis, H. T., Real-Space Renormalisation and effective medium approximation to the percolation conduction problem, *Phys. Rev. B*, Vol. 62, pp. 307-311, 1983.

Sarychev, A. K., and Vinogradoff, A. P., Percolation conductivity in anisotropic systems, *J. Phys. C*, Vol. 16, pp. L1073-L1077, 1983.

Scheidegger, A. E., *The Physics of Flow Through Porous Media,* 3rd ed., Oxford University Press, London, 1963.

Schlueter, E. M., *Predicting the Transport Properties of Sedimentary Rocks from Microstructure*, Ph.D. Thesis, University of California, Berkeley, 1995.

Scott, V. D., and Love, G., *Quantitative Electron-probe Microanalysis*, Ellis Horwood, Chichester, 1983.

Seeburger, D. A., and Nur, A., Pore space model for rock permeability and bulk modulus, *J. Geophys. Res.*, Vol. 89, pp. 527-536, 1984.

Selyakov, V. I., and Kadet, V. V., *Percolation Models for Transport in Porous Media with Applications to Reservoir Engineering*, Kluwer, Dordrecht, 1996.

Serra, J., *Image Analysis and Mathematical Morphology*, Academic Press, London, 1982.

Shankland, T. J., and Waff, H. S., Conductivity in fluid-bearing rocks, *J. Geophys. Res.* Vol. 79, pp. 4863-4868, 1974.

Shante, V. K. S., and Kirkpatrick, S., An introduction to percolation theory, *Adv. Phys.*, Vol. 20, pp. 325-357, 1971.

Shklovskii, B. I., Anisotropy of percolation conduction. *Phys. Stat. Sol. B*, Vol. 85, pp. K111-K114, 1978.

Sisavath, S., Jing, X. D., and Zimmerman, R. W., Effect of stress on the hydraulic conductivity of rock pores, *Phys. Chem. Earth A*, Vol. 25, pp. 163-168, 2000.

Sisavath, S., Jing, X. D., and Zimmerman, R. W., Creeping flow through a pipe of varying radius, *Phys. Fluids*, Vol. 13, pp. 2762-2772, 2001.

Skipper, N. T., Williams, G. D., de Siqueira, A. V. C., Lobban, C., and Soper, A. K., Time-of-flight neutron diffraction studies of clay-fluid interactions under basin conditions, *Clay Minerals*, Vol. 35, pp. 287-294, 2000.

Stanley, E. H., *Introduction to Phase Transitions and Critical Phenomena,* Oxford Science Publications, 1971.

Stauffer, D., and Aharony, A., *Introduction to Percolation Theory*, 2nd ed., Taylor and Francis, London, 1992.

Straley, J. P., Dimension-dependent scaling relations for conduction exponents. *J. Phys. C*, Vol. 13, pp. 819-822, 1980.

Stinchcombe, R. B., and Watson, B. P., Renormalisation group approach for percolation threshold conductivity, *J. Phys. C*, Vol. 9, pp. 3221-3347, 1976.

Sullivan, R. R., Specific surface measurements on compact bundles of parallel fibres, *J. Appl. Phys.*, Vol. 13, pp. 725-730, 1942.

Sykes, M. F., and Essam, J. W., Some exact critical percolation probabilities for bond and site problems in two dimensions, *Phys. Rev. Lett.*, Vol. 10, pp. 3-4, 1963.

Szabo, B. A., Permeability of orthotropic porous mediums, *Water Resour. Res.*, Vol. 4, pp. 801-808, 1968.

Tartakovsky, D. M., Moulton, D. J., and Zlotnik, V. A., Kinematic structure of minipermeameter flow, *Water Resour. Res.*, Vol. 36, pp. 2433-2442, 2000.

Till, R., *Statistical Methods for the Earth Scientist: An Introduction*, London, Macmillan, 1974.

Toledo, P. G., Davis, H. T., and Scriven, L. E., Transport properties of anisotropic media: effective medium theory, *Chem. Eng. Sci.*, Vol. 47, pp. 391-405, 1992.

Tsakiroglou, C. D., and A. C. Payatakes, Characterisation of the pore structure of reservoir rocks with the aid of serial sectioning analysis, mercury porosimetry and network simulation, *Adv. Water Resour.*, Vol. 23, pp. 773-789, 2000.

Underwood, E. E., *Quantitative Stereology,* Addison–Wesley, Reading, Massachusetts, 1970.

van der Pol, B., and Bremmer, H., *Operational Calculus,* Cambridge University Press, London, 1950.

van Dyke, M., Slow variations in continuum mechanics, *Adv. Appl. Mech.*, Vol. 25, pp. 1-45, 1987.

Walsh, J. B., and Brace, W. F., The effect of pressure on the transport properties of rock, *J. Geophys. Res.*,Vol. 89, pp. 9425-9431, 1984.

Weszka, J. S., A survey of threshold selection techniques, *Comput. Graph. Imag. Proc.*, Vol. 7, pp. 259-265, 1978.

Weszka, J. S., and Rosenfield, A., Histogram modification for threshold selection, *IEEE Trans. Syst. Man. Cyber.*, Vol. SMC -9, pp. 38-52, 1979.

Wilke, S., Bond percolation thresholds in the simple cubic lattice, *Phys. Lett. A*, Vol. 96, pp. 344-346, 1983.

Wyllie, M. R. J., and Spangler, M. B., Applications of electrical resistivity measurements to problem of fluid flow in porous media, *Bull. AAPG*, Vol. 36, pp. 359-403, 1952.

Young, D. M., *Iterative Solution of Large Linear Systems*, Academic Press, New York, 1971.

Young, G. R., Determining permeability anisotropy from a core plug using a minipermeameter, M. S. Thesis, University of Texas, Austin, 1989.

Zhang, L., and Seaton, N. A., Prediction of the effective diffusivity in pore networks close to a percolation threshold, *AIChE J.*, Vol. 38, pp. 1816-1824, 1992.

Zimmerman, R. W., Kumar, S., and Bodvarsson, G. S., Lubrication theory analysis of the permeability of rough-walled fractures, *Int. J. Rock Mech.*, Vol 28, pp. 325-331, 1991.

APPENDICES: CODE LISTING

A Isotropic Effective-Medium Approximation

B Anisotropic Effective-Medium Approximation in Two Dimensions

C Anisotropic Effective-Medium Approximation in Three Dimensions

D Program for Increasing the Size of Input files for NETSIM

E Program for Random Pore Selection

F Program for the Random Generation of Lognormal Deviates

G ISOTROPIC NETSIM, adapted from *Jing* (1990)

H ANISOTROPIC NETSIM, adapted from *Jing* (1990)

All programs were written and compiled using DIGITAL visual Fortran for Windows, version 5a.

A Isotropic Effective-Medium Approximation

```
      PROGRAM NEWTONKIRKPATRICK

C     GIVES THE ROOT TO KIRKPATRICK'S EQUATION USING THE NEWTON-
C     RAPHSON PROCEDURE

C     COMPUTES THE DERIVATIVE ANALYTICALLY

C     USES DOUBLE PRECISION ARITHMETIC TO ALLOW MORE STRINGENT AND
C     CONSISTENT CONVERGENCE CRITERIA

      IMPLICIT NONE
      REAL G, L, Z, ALPHA, GMAX, RMAX, GMIN
      DOUBLE PRECISION A, B, SQ, SER, DER, FX, RATIO,SUM,GGEO, X
      DIMENSION G(10000)
      INTEGER I, J, K
      PARAMETER(L=7397.)
      PARAMETER(Z=6)
      K=INT(L)

C     OPEN EXTERNAL DATAFILE AND READ IN THE CONDUCTIVITIES
      OPEN(UNIT=3,FILE='1YCOMPILED.txt', STATUS='OLD')
      REWIND(3)
      DO 10 I=1, K
        READ(3,*) G(I)
10    END DO

C     CALCULATE BOUNDS FOR GEFF, ALONG WITH THE GEOMETRIC MEAN, Ggeo
      Ggeo = 1.0
      Gmax = 0.0
      Rmax = 0.0
      DO 20 I=1, K
        Ggeo = Ggeo*(G(I))**(1/L)
        Gmax = Gmax + G(I)
      Rmax = Rmax + 1.0/G(I)
20    CONTINUE
      Gmax = Gmax/L
      Rmax = Rmax/L
      Gmin = 1.0/Rmax

      PRINT*, 'NO OF INPUT CONDUCTANCES:' , K
      PRINT*,'Gmin=', Gmin
      PRINT*,'Ggeo=', Ggeo
      PRINT*,'Gmax=', Gmax

      ALPHA=(Z/2)-1

C     INITIALISE OUR GUESS FOR X
      X = GGEO
C     DO LOOP FOR N-R ITERATION
      DO 30 J=1, 200
C       INITIALISE FUNCTION VALUES
        FX = 0.0
        SUM= 0.0
C       DO LOOP FOR CALCULATING FUNCTION VALUES
        DO 40 I=1, K
            FX = FX + (X-G(I))/(ALPHA*X+G(I))
C     COMPUTE DERIVATIVE USING QUOTIENT RULE AND SUM
```

```
            A=(ALPHA*X+G(I))
            B=ALPHA*(X-G(I))
            SER=A-B
            SQ=(ALPHA*X+G(I))**2
            DER=SER/SQ
            SUM=SUM+DER
40      CONTINUE
        RATIO=FX/SUM
C       UPDATE SOLUTION FOR ROOT
        X = X - RATIO
C       TEST TO SEE IF X HAS JUMPED OUTSIDE OF RANGE
            IF((GMIN-X)*(X-GMAX) .LT.0) THEN
            PAUSE 'X JUMPED OUT OF BRACKETS'
            ENDIF
C       TEST(S) FOR CONVERGENCE
        IF(ABS(RATIO) .LT. 0.0000001 .AND. ABS(FX) .LT. 0.0000001)THEN
        PRINT*,'N-R HAS CONVERGED TO', X
        STOP
        ENDIF
30      CONTINUE

        END
```

B Anisotropic Effective-Medium Approximation in Two Dimensions

```
      PROGRAM TWO DIMENSIONAL EMA

C     COMPUTES THE EFFECTIVE CONDUCTANCE IN TWO DIMENSIONS ON THE
C     SQUARE LATTICE BASING THE INITIAL GUESS FOR THE ROOT TO
C     BERNASCONI'S EQUATION (I.E., THE SOLUTION VECTOR) ON THE
C     GEOMETRIC MEANS OF TWO SETS OF INPUT DATA

C     THE GEOMETRIC MEANS ARE CALCULATED IN THE MAIN PROGRAM BY
C     READING IN THE CONDUCTANCES FROM THE EXTERNAL DATAFILES WHILE
C     SUCCESSIVELY RECALCULATING THE 1/Nth ROOT OF THE PRODUCT; THIS
C     METHOD OF CALCULATING A GEOMETRIC MEAN ELIMINATES THE OVERFLOW
C     PROBLEMS THAT ARISES WITH THE INCREASING PRODUCT

C     THE METHOD OF COMPUTING THE ROOT TO BERNASCONI'S EQUATION USES
C     THE GENERALISED NEWTON-RAPHSON PROCEDURE BASED ON THE SUBROUTINE
C     MNEWT GIVEN BY PRESS ET AL. (1992), AND IS WRITTEN AS A MAIN
C     BLOCK PROGRAM THAT RETURNS THE FUNCTION VALUES F AND THE 2X2
C     JACOBIAN MATRIX OF DERIVATIVES

C     THE ELEMENTS OF THE JACOBIAN ARE COMPUTED ANALYTICALLY TO
C     ELIMINATE THE POTENTIAL SENSITIVITY OF THE PROCEDURE TO
C     ARTEFACTS THAT MAY ARISE IN COMPUTING THE DERIVATIVE
C     NUMERICALLY, I.E., BY FINITE DIFFERENCES

C     NTRIAL ITERATIONS ARE PERFORMED FROM THE INITIAL GUESS TO THE
C     SOLUTION VECTOR AND THE SUCCESSIVE APPROXIMATIONS UPDATED BY
C     SOLVING THE RESULTING LINEAR EQUATIONS USING AN LU MATRIX
C     DECOMPOSITION WITH THE CONSECUTIVE SUBROUTINES LUDCMP AND
C     LUBSKB IN MNEWT AS SUGGESTED BY PRESS ET AL, (1992). THE
C     ITERATIVE PROCESS STOPS IF EITHER THE MAGNITUDE OF THE
C     FUNCTION VECTOR F IS LESS THAN SOME TOLERANCE TOLF,
C     OR IF THE SUM OF THE ABSOLUTE VALUES OF THE CORRECTIONS TO THE
C     ROOT IS LESS THAN SOME TOLERANCE TOLX

C     DOUBLE PRECISION ARITHMETIC IS USED TO MAINTAIN NUMERICAL
C     ACCURACY WITHIN THE RANGE OF INTEREST

      IMPLICIT NONE
      INTEGER   MA, DUM(2), N, M
      PARAMETER (MA=2)
      DOUBLEPRECISION XGGEO, XGMAX, XRMAX, XGMIN, YGGEO, YGMAX
      DOUBLEPRECISION YRMAX, YGMIN, CX, CY
      DOUBLEPRECISION C(2), CC(2), FVEC(2), FJAC(2,2), A, B
      INTEGER I,J, K, NTRIAL
      DOUBLEPRECISION TOLF, TOLX
      DOUBLEPRECISION D, ERRF, ERRX
      DOUBLEPRECISION P(2)

C     ENTER NUMBER OF ITERATIONS, NTRIAL
      PARAMETER (NTRIAL=100)
      DIMENSION CX(10000), CY(10000)
C     ENTER NUMBER OF CONDUCTANCES FOR X DIRECTION:
      PARAMETER (A=2.)
C     ENTER NUMBER OF CONDUCTANCES FOR Y DIRECTION:
      PARAMETER (B=2.)
      N=INT(A)
      M=INT(B)
```

```
C     GIVEN AN INITIAL GUESS FOR THE ROOT IN TWO DIMENSIONS, TAKE
C     NTRIAL NEWTON-RAPHSON STEPS TO IMPROVE THE ROOT. STOP IF THE
C     ROOT CONVERGES IN EITHER SUMMED ABSOLUTE VALUE INCREMENTS,
C     TOLX OR SUMMED ABSOLUTE VALUES OF THE FUNCTION, TOLF
      TOLF=1.0E-12
      TOLX=1.0E-12

C     READ IN DATA FOR 'X' AND 'Y' DIRECTIONS
      OPEN(UNIT=11,FILE='GEO1.txt',STATUS='OLD')
      OPEN(UNIT=12,FILE='GEO2.txt',STATUS='OLD')
      REWIND(11)
      REWIND(12)

C     READ IN THE CONDUCTIVITIES FOR THE 'X' DIRECTION
      XGGEO=1.0
      XGMAX=0.0
      XRMAX=0.0
      DO 5 I=1, N
        READ(11,*) CX(I)
C     CALCULATE THE GEOMETRIC MEAN, XGGEO
            XGGEO = XGGEO*(CX(I))**(1.0/A)
C     CALCULATE UPPER AND LOWER BOUNDS
            XGMAX=XGMAX+CX(I)
            XRMAX=XRMAX+ 1.0/CX(I)
5     CONTINUE
      XGMAX=XGMAX/A
      XGMIN=1.0/XRMAX
      PRINT*, 'XGGEO=', XGGEO

C     READ IN THE CONDUTIVITIES FOR THE Y DIRECTION
      YGGEO=1.0
      YGMAX=0.0
      YRMAX=0.0
      DO 8 J=1, M
        READ(12,*) CY(J)
C     CALCULATE THE GEOMETRIC MEAN, YGGEO
            YGGEO = YGGEO*(CY(J))**(1.0/B)
C     CALCULATE UPPER AND LOWER BOUNDS
            YGMAX=YGMAX+CY(J)
            YRMAX=YRMAX+ 1.0/CY(J)
8     CONTINUE

      YGMAX=YGMAX/B
      YGMIN=1.0/YRMAX
      PRINT*, 'YGGEO=', YGGEO

C     ************************************************************
      PRINT*, '      '
      PRINT*, '&&&&&&&&&&&&&&&&&&&&&&&&&&&&&'
      PRINT*, '      '

C     INITIALISATIONS TO N-R PROCEDURE
C     INPUTS X AND Y (GEOMETRIC MEANS OF RESPECTIVE INPUT DATA)
      C(1)=XGGEO
      C(2)=YGGEO
      DO 10 K=1, NTRIAL
C     CALL USRFUN; A USER-WRITTEN SUBROUTINE THAT SUPPLIES FUNCTION
C     VALUES AT X IN FVEC AND JACOBIAN MATRIX IN FJAC
```

```
            CALL USRFUN(C, FVEC,FJAC, N,M, CX, CY)
            ERRF=0.0
C       CHECK ERROR CONVERGENCE
            DO 20 I=1, 2
                  ERRF=ERRF + ABS(FVEC(I))
20          CONTINUE
        IF(ERRF .LE. TOLF)THEN
        PRINT*, '     '
        PRINT*, 'N-R HAS CONVERGED TO ROOT'
        GO TO 24
        END IF
            DO 30 I=1, 2
                  P(I)=-FVEC(I)
30          CONTINUE

C       SOLVE LINEAR EQUATIONS BY LU DECOMPOSTION USING THE SUBROUTINES
C       LUDCMP AND LUBKSB (PRESS ET AL., 1992)
        CALL  LUDCMP(FJAC, MA,MA,DUM, D)
        CALL  LUBKSB(FJAC,MA,MA,DUM, P)

C       CHECK ROOT CONVERGENCE
        ERRX=0.0
        DO 40 I=1, 2
C       UPDATE SOLUTION
          ERRX=ERRX+ABS(P(I))
          C(I)=C(I)+P(I)
40      CONTINUE

        PRINT*, 'NUMBER OF ITERATIONS:',  K
        IF (ERRX .LE. TOLX)THEN
        PRINT*, 'N-R HAS CONVERGED TO ROOT'
        GO TO 24
        ELSE
        PRINT*, ' OUTPUTS FOR SOLUTION VECTOR X1=',C(1)
        PRINT*, ' OUTPUTS FOR SOLUTION VECTOR X2=',C(2)
        END IF
10      CONTINUE

24      PRINT*, '      '
        PRINT*, 'FINAL OUTPUT FOR SOLUTION VECTOR X1=',C(1)
        PRINT*, 'FINAL OUTPUT FOR SOLUTION VECTOR X2=', C(2)
        PRINT*,  '              '
        PRINT*, '     END    '
        PRINT*, '    '

        END
C       ***************************************************************
C       END OF MAIN PROGRAM
C       ***************************************************************
C       SUBROUTINES ARE:
C       SUBROUTINE USRFUN(L,FVEC,FJAC, N, M, CX, CY)
C                         SUBROUTINE JJ(L, N, SUMXX,SUMXY, FX, CX)
C                         SUBROUTINE JK(L, M, SUMYX,SUMYY, FY, CY)
C       SUBROUTINE LUDCMP(A, N,NP,INDX,D)
C       SUBROUTINE LUBKSB(A,N,NP,INDX,B)
C       ***************************************************************
        SUBROUTINE USRFUN(L, FVEC,FJAC, N, M, CX, CY)
        IMPLICIT NONE
        DOUBLEPRECISION L(2),SUMXX,SUMXY,SUMYX,SUMYY
```

```
      DOUBLE PRECISION FX,FY,FVEC,FJAC,CX,CY
      INTEGER I, J, N, M
      DIMENSION CX(N), CY(M), FJAC(2,2),FVEC(2)

C     LOOP TO CALCULATE FUNCTION FVEC(1) AND DERIVATIVES WRT X AND
C     Y, FJAC(1,1) AND FJAC(1,2)
      CALL JJ(L, N, SUMXX,SUMXY, FX, CX)

C     LOOP TO CALCULATE FUNCTION FVEC(2) AND DERIVATIVES WRT X AND
C     Y, FJAC(2,1) AND FJAC(2,2)
      CALL JK(L, M, SUMYX,SUMYY, FY, CY)

      FVEC(1)=FX
      FVEC(2)=FY
      FJAC(1,1)=SUMXX
      FJAC(1,2)=SUMXY
      FJAC(2,1)=SUMYX
      FJAC(2,2)=SUMYY

      PRINT*, 'FJAC(1,1)', SUMXX
      PRINT*, 'FJAC(1,2)', SUMXY
      PRINT*, 'FJAC(2,1)', SUMYX
      PRINT*, 'FJAC(2,2)', SUMYY
      PRINT*, 'FVEC(1)=', FVEC(1), '    ', 'FVEC(2)=', FVEC(2)
      RETURN

      END

      SUBROUTINE LUDCMP(A, N,NP,INDX,D)

      INTEGER N, NP, INDX(N), NMAX
      DOUBLEPRECISION D, A(NP,NP), TINY
      PARAMETER (NMAX=500, TINY=1.0E-20)
      INTEGER I, IMAX, J,K
      DOUBLEPRECISION AAMAX,DUM,SUM,VV(NMAX)

      D=1
      DO 12 I=1, N
        AAMAX=0
          DO 11 J=1, N
          IF (ABS (A(I,J)). GT. AAMAX) AAMAX=ABS(A(I,J))
11    CONTINUE
        IF (AAMAX. EQ. 0) PAUSE 'SINGULAR MATRIX IN LU
     +DECOMPOSITION SUBROUTINE'
      VV(I)=1/AAMAX
12    CONTINUE
      DO 19 J=1, N
        DO 14 I=1, J-1
          SUM=A(I,J)
            DO 13 K=1, I-1
              SUM=SUM-A(I,K)*A(K,J)
13          CONTINUE
              A(I,J)=SUM
14      CONTINUE
            AAMAX=0
              DO 16 I=J, N
                SUM=A(I,J)
                  DO 15 K=1, J-1
                    SUM=SUM-A(I,K)*A(K,J)
```

```
15                CONTINUE
                    A(I,J)=SUM
                    DUM=VV(I)*ABS(SUM)
                      IF (DUM. GE. AAMAX) THEN
                        IMAX=I
                        AAMAX=DUM
                      ENDIF
16              CONTINUE
                  IF (J. NE. IMAX) THEN
                    DO 17 K=1, N
                      DUM=A(IMAX, K)
                        A(IMAX,K)=A(J,K)
                        A(J,K)=DUM
17                CONTINUE
      D=-D
      VV(IMAX)=VV(J)
                ENDIF
      INDX(J)=IMAX
        IF(A(I,J). EQ. 0) A(I,J)=TINY
          IF(J. NE.N)THEN
            DUM=1/A(J,J)
              DO 18 I=J+1, N
                A(I,J)=A(I,J)*DUM
18            CONTINUE
          ENDIF
19    CONTINUE
      RETURN

      END
      SUBROUTINE LUBKSB(A,N,NP,INDX,B)

      INTEGER N, NP, INDX(2)
      INTEGER I, II, J,LL
      DOUBLEPRECISION TOTAL
      DOUBLEPRECISION B(2), A(2,2)

            II=0
         DO 45 I=1, N
             LL=INDX(I)
             TOTAL=B(LL)
             B(LL)=B(I)
             IF (II. NE. 0) THEN
                   DO 50 J=II, I-1
                TOTAL=TOTAL-A(I,J)*B(J)
50    CONTINUE
             ELSE IF (TOTAL. NE. 0) THEN
               II=1
             ENDIF
             B(I)=TOTAL
45    CONTINUE
       DO 55 I=N, 1,-1
             TOTAL=B(I)
               DO 60 J=I+1, N
                 TOTAL =TOTAL-A(I,J)*B(J)
60    CONTINUE
             B(I)=TOTAL/A(I,I)
55    CONTINUE
      RETURN
```

```
      END
C     ************************************************************
      SUBROUTINE JJ(L, N, SUMXX,SUMXY, FX, CX)
C     OUTPUTS THE FUNCTION FX, J(1,2), AND J(1,1)

      IMPLICIT NONE
      INTEGER N, I
C     PARAMETERS REQUIRED FOR ALL THREE CALCULATIONS
      DOUBLEPRECISION CX(N),L(2)
C     PARAMETERS REQUIRED FOR THE ELEMENT J(1,1)
      DOUBLEPRECISION A,B,C,D,E,F, ANALYA, ANALYB, ANALYC, XX, SUMXX
C     PARAMETERS REQUIRED FOR THE ELEMENT J(1,2)
      DOUBLEPRECISION  NUMC, NUMD, NUME, NUMF, NUMG, NUMH, DD,SUMXY
C     PARAMETERS REQUIRED FOR THE FUNCTION FX
      DOUBLEPRECISION FX,SX

      REWIND(11)
C     INITIALISATIONS
      SUMXX=0.0
      SUMXY=0.0
      FX=0.0
      DO 200 I=1, N
      F=-0.5*((L(2)**0.5)/(L(1)**1.5))*(1/(1+(L(2)/L(1))))
      C=ATAN(SQRT(L(1)/L(2)))*F
      D=ATAN(SQRT(L(2)/L(1)))*(0.5*SQRT(1/(L(1)*L(2))))*(1/(1+(L(1)/L(2
     +))))
      E=(ATAN(SQRT(L(1)/L(2))))**2.0
      B=(C-D)/E
      A=(ATAN(SQRT(L(2)/L(1)))/(ATAN(SQRT(L(1)/L(2)))))

C     COMPUTES THE 'A' AND 'B' PARTS OT THE DERIVATIVE J(1,1)
      ANALYA=CX(I)+L(1)*(ATAN(SQRT(L(2)/L(1)))/ATAN(SQRT(L(1)/L(2))))
      ANALYB=(CX(I)+L(1)*(ATAN(SQRT(L(2)/L(1)))/ATAN(SQRT(L(1)/L(2)))))
     +**2
      ANALYC=(L(1)-CX(I))*(A+L(1)*B)

C     COMBINE THESE THREE MAJOR COMPONENTS AS
C     XX=(ANALYA-ANALYC)/ANALYB:
      XX=(ANALYA-ANALYC)/ANALYB
      SUMXX=SUMXX+XX

C     NOW REPEAT FOR SECOND ELEMENT OF JACOBIAN
      NUMC=(ATAN(SQRT(L(1)/L(2))))*(0.5*SQRT(1.0/(L(1)*L(2))))
     +*(1.0/(1.0+L(2)/L(1)))
      NUMD=(ATAN(SQRT(L(2)/L(1))))*(-0.5*((L(1)**0.5)/L(2)**
     +1.5))*(1.0/(1.0+(L(1)/L(2))))
      NUME=(NUMC-NUMD)
      NUMF=(ATAN(SQRT(L(1)/L(2))))**2.0
      NUMH=(CX(I)+L(1)*(ATAN(SQRT(L(2)/L(1)))/ATAN(SQRT(L(1)/L(2))))
     +)**2
      NUMG=L(1)*(L(1)-CX(I))*(NUME/NUMF)
      DD=(-NUMG)/NUMH
      SUMXY=SUMXY+DD

C     NOW PRODUCE THE FUNCTION
      SX=L(1)*((ATAN(SQRT(L(2)/L(1))))/(ATAN(SQRT(L(1)/L(2)))))
      FX= FX +(L(1)-CX(I))/(CX(I)+SX)
200   CONTINUE
      RETURN
```

```
      END

      SUBROUTINE JK(L, M, SUMYX,SUMYY, FY, CY)
C     OUTPUTS THE FUNCTION FY, J(2,1) AND J(2,2)

      IMPLICIT NONE
      INTEGER M, J
C     PARAMETERS REQUIRED FOR ALL THREE CALCULATIONS
      DOUBLEPRECISION CY(M), L(2)
C     PARAMETERS REQUIRED FOR THE ELEMENT J(2,2)
      DOUBLEPRECISION F,C,D,E,B,A,ANALYA,ANALYB,ANALYC,YY,SUMYY
C     PARAMETERS REQUIRED FOR THE ELEMENT J(2,1)
      DOUBLEPRECISION ALPHA,DD,EE,FF,SUMYX, ANALYD,ANALYE, J21
C     PARAMETERS REQUIRED FOR THE FUNCTION FY
      DOUBLEPRECISION SY, FY

C     OPEN(UNIT=12, FILE='YDATA.txt', STATUS='OLD')
      REWIND(12)
C     INITIALISATIONS
      SUMYY=0.0
      SUMYX=0.0
      FY=0.0
      DO 10 J=1, M
C     READ(12,*) CY(J)
C     J(2,2)
      F=-0.5*((L(1)**0.5)/(L(2)**1.5))*(1/(1+(L(1)/L(2))))
      C=ATAN(SQRT(L(2)/L(1)))*F
      D=ATAN(SQRT(L(1)/L(2)))*(0.5*SQRT(1/(L(2)*L(1))))+*(1/(1+(L(2)/L(
     +1))))
      E=(ATAN(SQRT(L(2)/L(1))))**2.0
      B=(C-D)/E
      A=(ATAN(SQRT(L(1)/L(2)))/(ATAN(SQRT(L(2)/L(1)))))

C     COMPUTES THE 'A' AND 'B' PARTS OT THE DERIVATIVE J(2,2)
      ANALYA=CY(J)+L(2)*(ATAN(SQRT(L(1)/L(2)))/ATAN(SQRT(L(2)/L(1)))
     +)
      ANALYB=(CY(J)+L(2)*(ATAN(SQRT(L(1)/L(2)))/ATAN(SQRT(L(2)/L(1)))))
     +**2
      ANALYC=(L(2)-CY(J))*(A+L(1)*B)

C     COMBINE THESE THREE MAJOR COMPONENTS AS
C     YY=(ANALYA-ANALYC)/ANALYB:
      YY=(ANALYA-ANALYC)/ANALYB
      SUMYY=SUMYY+YY
C     COMPUTE J(2,1)
     DD=(ATAN(SQRT(L(2)/L(1))))*(1/(1+(L(1)/L(2))))*(0.5*SQRT(1/(L(1)*
    +L(2))))
      EE=(ATAN(SQRT(L(1)/L(2))))*(1/(1+(L(2)/L(1))))*(0.5*(SQRT(L(2))
     +/(L(1)**1.5))))
      FF=(ATAN(SQRT(L(2)/L(1))))**2.0

C     COLLECT TERMS TO GIVE PART B
      ALPHA=L(2)*(L(2)-CY(J))
      ANALYD=(ALPHA*(DD-EE)/FF)

C     NOW A=0 SO WE JUST NEED THE FORM OF C
      ANALYE=(CY(J)+L(2)*(ATAN(SQRT(L(1)/L(2)))))/(ATAN(SQRT(L(2)/L(1))
     +))**2.0
      J21= -ANALYD/ANALYE
```

```
      SUMYX =SUMYX+J21
C     CALCULATE FUNCTION
      SY=L(2)*((ATAN(SQRT(L(1)/L(2))))/(ATAN(SQRT(L(2)/L(1)))))
      FY= FY+(L(2)-CY(J))/(CY(J)+SY)
10    CONTINUE
      RETURN

      END
```

C Anisotropic Effective-Medium Approximation in Three Dimensions

```
      PROGRAM THREE DIMENSIONAL EMA

C     COMPUTES THE EFFECTIVE CONDUCTANCE IN THREE DIMENSIONS ON THE
C     CUBIC LATTICE BASING THE INITIAL GUESS FOR THE ROOT TO
C     BERNASCONI'S EQUATION (I.E., THE SOLUTION VECTOR) ON THE
C     GEOMETRIC MEANS OF THREE SETS OF INPUT DATA

C     THE GEOMETRIC MEANS ARE CALCULATED IN THE MAIN PROGRAM BY
C     READING IN THE CONDUCTANCES FROM THE EXTERNAL DATAFILES WHILE
C     SUCCESSIVELY RECALCULATING THE 1/Nth ROOT OF THE PRODUCT; THIS
C     METHOD OF CALCULATING A GEOMETRIC MEAN ELIMINATES THE OVERFLOW
C     PROBLEMS THAT ARISES WITH THE INCREASING PRODUCT

C     THE METHOD OF COMPUTING THE ROOT TO BERNASCONI'S EQUATION USES
C     THE GENERALISED NEWTON-RAPHSON PROCEDURE BASED ON THE SUBROUTINE
C     MNEWT GIVEN BY PRESS ET AL. (1992), AND IS WRITTEN AS A MAIN
C     BLOCK PROGRAM THAT RETURNS THE FUNCTION VALUES F AND THE 3X3
C     JACOBIAN MATRIX OF DERIVATIVES

C     THE ELEMENTS OF THE JACOBIAN ARE COMPUTED ANALYTICALLY TO
C     ELIMINATE THE POTENTIAL SENSITIVITY OF THE PROCEDURE TO
C     ARTEFACTS THAT MAY ARISE IN COMPUTING THE DERIVATIVE
C     NUMERICALLY, I.E., BY FINITE DIFFERENCES

C     NTRIAL ITERATIONS ARE PERFORMED FROM THE INITIAL GUESS TO THE
C     SOLUTION VECTOR AND THE SUCCESSIVE APPROXIMATIONS UPDATED BY
C     SOLVING THE RESULTING LINEAR EQUATIONS USING AN LU MATRIX
C     DECOMPOSITION WITH THE CONSECUTIVE SUBROUTINES LUDCMP AND
C     LUBSKB IN MNEWT AS SUGGESTED BY PRESS ET AL, (1992). THE
C     ITERATIVE PROCESS STOPS IF EITHER THE MAGNITUDE OF THE
C     FUNCTION VECTOR F IS LESS THAN SOME TOLERANCE TOLF,
C     OR IF THE SUM OF THE ABSOLUTE VALUES OF THE CORRECTIONS TO THE
C     ROOT IS LESS THAN SOME TOLERANCE TOLX

C     DOUBLE PRECISION ARITHMETIC IS USED TO MAINTAIN NUMERICAL
C     ACCURACY WITHIN THE RANGE OF INTEREST

      IMPLICIT NONE
      INTEGER MA, TUM(3), HH, II, JJ
      PARAMETER (MA=3)
      DOUBLEPRECISION XGGEO,XGMAX,XRMAX,XGMIN
      DOUBLEPRECISION YGGEO,YGMAX,YRMAX,YGMIN
      DOUBLEPRECISION ZGGEO,ZGMAX,ZRMAX,ZGMIN
      DOUBLEPRECISION CX, CY, CZ
      DOUBLEPRECISION C(3), FVEC(3), FJAC(3,3)
      DOUBLE PRECISION AA, BB, CC
      INTEGER H, I, J, K, NTRIAL
      DOUBLEPRECISION TOLF, TOLX
      DOUBLEPRECISION D, ERRF, ERRX
      DOUBLEPRECISION P(3), G(3)
      DIMENSION CX(10000), CY(10000), CZ(1000)

C     ENTER NUMBER OF CONDUCTANCES FOR THE X DIRECTION:
      PARAMETER (HH= 1843.)
C     ENTER NUMBER OF CONDUCTANCES FOR THE Y DIRECTION:
      PARAMETER (II= 1244.)
C     ENTER NUMBER OF CONDUCTANCES FOR THE Z DIRECTION:
```

```
      PARAMETER (JJ= 1579.)
      AA=REAL(HH)
      BB=REAL(II)
      CC=REAL(JJ)

      PRINT*, 'ENTER NUMBER OF NEWTON-RAPHSON STEPS'
      READ*, NTRIAL

C     GIVEN AN INITIAL GUESS FOR THE ROOT IN TWO DIMENSIONS, TAKE
C     NTRIAL NEWTON-RAPHSON STEPS TO IMPROVE THE ROOT. STOP IF THE
C     ROOT CONVERGES IN EITHER SUMMED ABSOLUTE VALUE INCREMENTS,
C     TOLX OR SUMMED ABSOLUTE VALUES OF THE FUNCTION, TOLF
      TOLF=1.0E-12
      TOLX=1.0E-12

C     READ IN DATA FOR 'X', 'Y', AND 'Z' DIRECTIONS
      OPEN(UNIT=11,FILE='2XCOMPILED.txt',STATUS='OLD')
      OPEN(UNIT=12,FILE='2BCOMPILED.txt',STATUS='OLD')
      OPEN(UNIT=13,FILE='2CCOMPILED.txt',STATUS='OLD')
      REWIND(11)
      REWIND(12)
      REWIND(13)

C     READ IN THE CONDUCTIVITIES FOR THE 'X' DIRECTION
      XGGEO=1.0
      XGMAX=0.0
      XRMAX=0.0
      DO 5 H=1, HH
            READ(11,*) CX(H)
C     CALCULATE THE GEOMETRIC MEAN, XGGEO
            XGGEO = XGGEO*(CX(H))**(1.0/AA)
C     CALCULATE UPPER AND LOWER BOUNDS
            XGMAX=XGMAX+CX(H)
            XRMAX=XRMAX+ 1.0/CX(H)
5     CONTINUE
      XGMAX=XGMAX/AA
      XRMAX=XRMAX/AA
      XGMIN=1.0/XRMAX

C     READ IN THE CONDUCTIVITIES FOR THE 'Y' DIRECTION
      YGGEO=1.0
      YGMAX=0.0
      YRMAX=0.0
      DO 6 I=1, II
            READ(12,*) CY(I)
C     CALCULATE THE GEOMETRIC MEAN, YGGEO
            YGGEO = YGGEO*(CY(I))**(1.0/BB)
C     CALCULATE UPPER AND LOWER BOUNDS
            YGMAX=YGMAX+CY(I)
            YRMAX=YRMAX+ 1.0/CY(I)
6     CONTINUE
      YGMAX=YGMAX/BB
      YRMAX=YRMAX/BB
      YGMIN=1.0/YRMAX

C     READ IN THE CONDUCTIVITIES FOR THE Z DIRECTION
      ZGGEO=1.0
      ZGMAX=0.0
      ZRMAX=0.0
```

```
      DO 7 J=1, JJ
            READ(13,*) CZ(J)
C           CALCULATE THE GEOMETRIC MEAN, ZGGEO
            ZGGEO = ZGGEO*(CZ(J))**(1.0/CC)
C     CALCULATE UPPER AND LOWER BOUNDS
            ZGMAX=ZGMAX+CZ(J)
            ZRMAX=ZRMAX+ 1.0/CZ(J)
7     CONTINUE
      ZGMAX=ZGMAX/CC
      ZRMAX=ZRMAX/CC
      ZGMIN=1.0/ZRMAX

      PRINT*,'XGGEO=', XGGEO
      PRINT*,'XGMAX=', XGMAX
      PRINT*,'XGMIN=', XGMIN
      PRINT*,'YGGEO=', YGGEO
      PRINT*,'YGMAX=', YGMAX
      PRINT*,'YGMIN=', YGMIN
      PRINT*,'ZGGEO=', ZGGEO
      PRINT*,'ZGMAX=', ZGMAX
      PRINT*,'ZGMIN=', ZGMIN
      PRINT*, '      '
      PRINT*, '&&&&&&&&&&&&&&&&&&&&&&&&&&&&&'
      PRINT*, '      '

C     INITIALISATIONS TO N-R PROCEDURE

C     INPUTS X, Y AND Z (GEOMETRIC MEANS OF RESPECTIVE INPUT DATA)
      C(1)=XGGEO
      C(2)=YGGEO
      C(3)=ZGGEO
      DO 10 K=1, NTRIAL
C     CALL USRFUN; A USER-WRITTEN SUBROUTINE THAT SUPPLIES FUNCTION
C     VALUES AT X IN FVEC AND JACOBIAN MATRIX IN FJAC
            CALL USRFUN(C, FVEC,FJAC, HH,II,JJ, CX, CY, CZ)
            ERRF=0.0
C     CHECK ERROR CONVERGENCE
            DO 20 I=1, 3
                  ERRF=ERRF + ABS(FVEC(I))
20          CONTINUE
      IF(ERRF .LE. TOLF)THEN
      PRINT*, '     '
      PRINT*, 'N-R HAS CONVERGED TO ROOT'
      GO TO 24
      END IF
            DO 30 I=1, 3
                  P(I)=-FVEC(I)
30          CONTINUE

C     SOLVE LINEAR EQUATIONS BY LU DECOMPOSTION USING THE SUBROUTINES
C     LUDCMP AND LUBKSB (PRESS ET AL., 1992)
      CALL  LUDCMP(FJAC,MA,MA,TUM,D)
      CALL  LUBKSB(FJAC,MA,MA,TUM,P)

C     CHECK ROOT CONVERGENCE
      ERRX=0.0
      DO 40 I=1, 3
C     UPDATE SOLUTION
            ERRX=ERRX+ABS(P(I))
```

```
            C(I)=C(I)+P(I)

40      CONTINUE

        GG(1)= REAL (C(1))
        GG(2)= REAL (C(2))
        GG(3)= REAL (C(3))

        PRINT*, '     '
        PRINT*, 'NUMBER OF ITERATIONS:',  K
        PRINT*, '     '

        IF (ERRX .LE. TOLX)THEN
        PRINT*, 'N-R HAS CONVERGED TO ROOT'
        GO TO 24
        ELSE
        PRINT*, ' OUTPUTS FOR SOLUTION VECTOR X1=',C(1)
        PRINT*, ' OUTPUTS FOR SOLUTION VECTOR X2=',C(2)
        PRINT*, ' OUTPUTS FOR SOLUTION VECTOR X3=',C(3)
        END IF
10      CONTINUE

        PRINT*, '      '
        PRINT*, '*******************************************'
        PRINT*, '*******************************************'
24      PRINT*, '      '
        PRINT*, 'FINAL OUTPUT FOR SOLUTION VECTOR X1=',C(1)
        PRINT*, 'FINAL OUTPUT FOR SOLUTION VECTOR X2=',C(2)
        PRINT*, 'FINAL OUTPUT FOR SOLUTION VECTOR X3=',C(3)
        PRINT*,  '              '
        PRINT*, '     END    '
        PRINT*, '    '

        END
C       ***************************************************************
C       END OF MAIN PROGRAM
C       ***************************************************************
C       SUBROUTINES ARE:
C       SUBROUTINE USRFUN(L,FVEC,FJAC, HH, II, JJ, CX, CY, CZ)
C                   FIRSTROW(L, HH, SUMXX, SUMXY, SUMXZ, FX, CX, LFUN)
C                   SECONDROW(L,II, SUMYX, SUMYY, SUMYZ, FY, CY, LFUN)
C                   THIRDROW(L, JJ, SUMZX, SUMYZ, SUMZZ, FZ, CZ, LFUN)
C       SUBROUTINE LUDCMP(A, N,NP,INDX,D)
C       SUBROUTINE LUBKSB(A,N,NP,INDX,B)
C       ***************************************************************
        SUBROUTINE USRFUN (L, FVEC, FJAC, HH, II, JJ, CX, CY, CZ)
        IMPLICIT NONE
        DOUBLE PRECISION L(3), FX, FY, FZ, FVEC, FJAC
        DOUBLE PRECISION CX, CY, CZ, LFUN
        INTEGER HH, II, JJ
        DOUBLE PRECISION SUMXX, SUMXY, SUMXZ
        DOUBLE PRECISION SUMYX, SUMYY, SUMYZ
        DOUBLE PRECISION SUMZX, SUMZY, SUMZZ
        DIMENSION CX(HH), CY(II), CZ(JJ), FVEC(3), FJAC(3,3)

        LFUN= (L(1)*L(2)+L(2)*L(3)+L(3)*L(1))

C       LOOP TO CALCULATE THE FUNCTION FVEC(1) AND DERIVATIVES WRT X,Y
C       AND Z, FJAC(1,1), FJAC(1,2) AND FJAC(1,3):
```

```
      CALL FIRSTROW(L, HH, SUMXX, SUMXY, SUMXZ, FX, CX, LFUN)

C     LOOP TO CALCULATE THE FUNCTION FVEC(2) AND DERIVATIVES WRT X,Y
C     AND Z, FJAC(2,1), FJAC(2,2) AND FJAC(2,3):
      CALL SECONDROW(L,II, SUMYX, SUMYY, SUMYZ, FY, CY, LFUN)

C     LOOP TO CALCULATE THE FUNCTION FVEC(3) AND DERIVATIVES WRT X,Y
C     AND Z, FJAC(3,1), FJAC(3,2) AND FJAC(3,3):
      CALL THIRDROW(L, JJ, SUMZX, SUMYZ, SUMZZ, FZ, CZ, LFUN)

      FVEC(1)=FX
      FVEC(2)=FY
      FVEC(3)=FZ

      FJAC(1,1)= SUMXX
      FJAC(1,2)= SUMXY
      FJAC(1,3)= SUMXZ
      FJAC(2,1)= SUMYX
      FJAC(2,2)= SUMYY
      FJAC(2,3)= SUMYZ
      FJAC(3,1)= SUMZX
      FJAC(3,2)= SUMZY
      FJAC(3,3)= SUMZZ
      RETURN

      END

      SUBROUTINE LUDCMP(A, N,NP,INDX,D)

      INTEGER N, NP, INDX(N), NMAX
      DOUBLEPRECISION D, A(NP,NP), TINY
      PARAMETER (NMAX=500, TINY=1.0E-20)
      INTEGER I, IMAX, J,K
      DOUBLEPRECISION AAMAX,DUM,SUM,VV(NMAX)

      D=1
      DO 12 I=1, N
        AAMAX=0
      DO 11 J=1, N
          IF (ABS (A(I,J)). GT. AAMAX) AAMAX=ABS(A(I,J))
11    CONTINUE
        IF (AAMAX. EQ. 0) PAUSE 'SINGULAR MATRIX IN LU
     +DECOMPOSITION SUBROUTINE'
        VV(I)=1/AAMAX
12    CONTINUE
      DO 19 J=1, N
        DO 14 I=1, J-1
          SUM=A(I,J)
            DO 13 K=1, I-1
              SUM=SUM-A(I,K)*A(K,J)
13          CONTINUE
              A(I,J)=SUM
14      CONTINUE
            AAMAX=0
              DO 16 I=J, N
                SUM=A(I,J)
                  DO 15 K=1, J-1
                    SUM=SUM-A(I,K)*A(K,J)
15                CONTINUE
```

```
                    A(I,J)=SUM
                    DUM=VV(I)*ABS(SUM)
                      IF (DUM. GE. AAMAX) THEN
                        IMAX=I
                        AAMAX=DUM
                      ENDIF
16              CONTINUE
                  IF (J. NE. IMAX) THEN
                    DO 17 K=1, N
                      DUM=A(IMAX, K)
                        A(IMAX,K)=A(J,K)
                        A(J,K)=DUM
17                  CONTINUE
      D=-D
      VV(IMAX)=VV(J)
                  ENDIF
      INDX(J)=IMAX
        IF(A(I,J). EQ. 0) A(I,J)=TINY
          IF(J. NE.N)THEN
            DUM=1/A(J,J)
              DO 18 I=J+1, N
                A(I,J)=A(I,J)*DUM
18              CONTINUE
          ENDIF
19    CONTINUE
      RETURN

      END

      SUBROUTINE LUBKSB(A,N,NP,INDX,B)

      INTEGER N, NP, INDX(3)
      INTEGER I, II, J,LL
      DOUBLEPRECISION TOTAL
      DOUBLEPRECISION B(3), A(3,3)

            II=0
         DO 45 I=1, N
             LL=INDX(I)
             TOTAL=B(LL)
             B(LL)=B(I)
             IF (II. NE. 0) THEN
                   DO 50 J=II, I-1
                TOTAL=TOTAL-A(I,J)*B(J)
50    CONTINUE
             ELSE IF (TOTAL. NE. 0) THEN
               II=1
             ENDIF
             B(I)=TOTAL
45    CONTINUE
       DO 55 I=N, 1,-1
             TOTAL=B(I)
               DO 60 J=I+1, N
                 TOTAL =TOTAL-A(I,J)*B(J)
60    CONTINUE
             B(I)=TOTAL/A(I,I)
55    CONTINUE
      RETURN
```

```
      END
C     ***************************************************************
      SUBROUTINE FIRSTROW(L, HH, SUMXX, SUMXY, SUMXZ, FX, CX, A)

      IMPLICIT NONE
C     ARGUMENT DECLARATIONS ONLY
      DOUBLE PRECISION L(3)
      INTEGER HH
      DOUBLE PRECISION SUMXX, SUMXY, SUMXZ, FX, A
C     REMAINING DECLARATIONS
      INTEGER H
      DOUBLE PRECISION CX(HH)
      DOUBLE PRECISION S1, ALPHA, BETA, ATANALD1, ATANBED1
      DOUBLE PRECISION SUBQUOTJ11, DS1WRTL1, ATANALD2, ATANBED2
      DOUBLE PRECISION DS1WRTL2, ATANALD3, ATANBED3, DS1WRTL3

C     FIRST CALCULATE THE BOND GREEN FUNCTION FOR THE X DIRECTION:
C     S1
C     S1 TAKES THE FORM:
      ALPHA= (A**0.5)/L(1)
      BETA= L(1)/(A**0.5)
      S1=L(1)*((ATAN(ALPHA))/(ATAN(BETA)))
C     WE MUST NOW PROCEED TO CALCULATE THE FIRST ROW OF DERIVATIVES
C     IN THE JACOBIAN MATRIX. IN ALL CASES THE DIFFERENTATION OF FX
C     WRT X, Y AND Z FOLLOWS THE  QUOTIENT RULE BEGIN BY CALCULATING
C     THE RESPECTIVE COMPONENTS OF THE QUOTIENT:

C     COMMENCE WITH THE FIRST ELEMENT OF THE JACOBIAN. DENOTE AS SUMXX

C     FIRST NEED THE DERIVATIVE OF ARCTANALPHA WRT L(1). DENOTE BY
C     ATANALD1
      ATANALD1=(1.0/(1.0+ALPHA**2.0))*((L(2)+L(3)-2.0*A)
     +/(L(1)*2.0*A**0.5))

C     NOW REQUIRE THE DERIVATIVE OF ARCTANBETA WRT L(1). DENOTE BY
C     TANBED1
      ATANBED1=(1.0/(1.0+BETA**2.0))*((2.0*A-L(1)*(L(2)+L(3)))
     +/(2*A**1.5))

C     THESE TWO DERIVATIVES FORM THE 'SUBQUOTIENT' WHICH IS THE
C     DERIVATIVE OF ARCTANALPHA/ARCTANBETA WRT L(1). DENOTE AS
C     SUBQUOTJ11
      SUBQUOTJ11=((ATAN(BETA)*ATANALD1 -ATAN(ALPHA)*ATANBED1)
     +/((ATAN(BETA))**2.0))

C     SUBQUOTJ11 FORMS THE DERIVATIVE OF S1 WHICH FORMS PART OF THE
C     MAIN QUOTIENT
C     LET US DENOTE THE DERIVATIVE OF S1 WRT L(1) AS  DS1WRTL1,
C     WHICH FOLLOWS THE PRODUCT RULE
      DS1WRTL1= L(1)*SUBQUOTJ11+((ATAN(ALPHA))/(ATAN(BETA)))

C     WE NOW TAKE THESE COMPONENTS AND FORM THE MAIN QUOTIENT, SUMXX
C     INSIDE LOOP 20
C***************************************************************
C     NOW COMPUTE THE SECOND ELEMENT OF THE FIRST ROW, SUMXY. AS
C     BEFORE, WE PROCEED BY COMPUTING THE DERIVATIVE OF ARCTANALPHA
C     WRTL(2). DENOTE BY ATANALD2:
     ATANALD2=(1.0/(1.0+ALPHA**2.0))*((L(1)+L(3))/(L(1)*2.0*A**0.5)
    +)
```

```
C      ... AND ALSO THE DERIVATIVE OF ARCTANBETA WRT L(2), DENOTE AS
C      TANBED2:
       ATANBED2=(1.0/(1.0+BETA**2.0))*(L(1)*(L(1)+L(3)))/(2.0*A**1.5)

C      THESE TWO DERIVATIVES  AGAIN FORM A 'SUBQUOTIENT' WHICH IS THE
C      DERIVATIVE OF ARCTANALPHA/ARCTANBETA WRT L(2). UNLIKE THE
C      DIAGONAL ELEMENTS OF THE JACOBIAN, THE OFF-DIAGONAL ELEMENTS
C      HAVE A SLIGHTLY SIMPLER FORM FOR THE DERIVATIVES OF THE BOND
C      GREEN FUNCTIONS, SO WE CAN WRITE DIRECTLY THE DERIVATIVE OF S1
C      WRT L(2) AS DS1WRTL2
       DS1WRTL2=L(1)*((ATAN(BETA)*ATANALD2 -ATAN(ALPHA)*ATANBED2)
     +/((ATAN(BETA))**2.0))

C      WITH DS1WRTL2, WE CAN FORM A MAIN QUOTIENT AND SUM INSIDE LOOP
C      20; THIS IS SUMXY
C*****************************************************************
C      FINALLY, WE COMPUTE THE THIRD ELEMENT OF THE FIRST ROW, SUMXZ.
C      AS BEFORE, WE PROCEED BY COMPUTING THE DERIVATIVE OF ARCTANALPHA
C      WRT L(3). DENOTE BY ATANALD3:
       ATANALD3=(1.0/(1.0+ALPHA**2.0))*((L(1)+L(2))/(L(1)*2.0*A**0.5)
     +)

C      SIMILARLY, THE DERIVATIVE OF ARCTANBETA WRT L(3) IS REQUIRED,
C      DENOTE AS ATANBED3
       ATANBED3=(1.0/(1.0+BETA**2.0))*(L(1)*(L(1)+L(2)))/(2.0*A**1.5)

C      AND SO NOW FORM THE DERIVATIVE OF S1 WRT L(3). DENOTE AS
C      DS1WRTL3
       DS1WRTL3=L(1)*((ATAN(BETA)*ATANALD3 -ATAN(ALPHA)*ATANBED3)
     +/((ATAN(BETA))**2.0))

C      WITH DS1WRTL3, WE CAN FORM A MAIN QUOTIENT AND SUM INSIDE LOOP
C      20; THIS IS SUMXZ

C      AND THAT CONCLUDES THE CALCULATION OF THE DERIVATIVES THAT
C      FORM THE ELEMENTS OF THE FIRST ROW OF THE JACOBIAN, BUT WE
C      ALSO REQUIRE THE PARENT FUNCTION FX AS WELL!!
C      USING THE FORMULA FOR S1 WE FORM THE SUM FX DIRECTLY INSIDE
C      LOOP 20
C*****************************************************************
C      INITALISE THE FOUR SUMMATIONS
       FX=0.0
       SUMXX = 0.0
       SUMXY = 0.0
       SUMXZ = 0.0
       DO 20 H=1, HH
C      WITH S1 NOW CONSTRUCT THE SUM FOR FX
          FX = FX +((L(1)-CX(H))/(CX(H)+S1))
          SUMXX=SUMXX+((CX(H)+S1)-(L(1)CX(H))*DS1WRTL1)/((CX(H)+S1**2.0)
          SUMXY=SUMXY+(-(L(1)-CX(H))*DS1WRTL2)/((CX(H)+S1)**2.0)
          SUMXZ=SUMXZ+(-(L(1)-CX(H))*DS1WRTL3)/((CX(H)+S1)**2.0)
20     CONTINUE
       RETURN

       END
C      ***************************************************************
C      ***************************************************************
       SUBROUTINE SECONDROW(L, II, SUMYX, SUMYY, SUMYZ, FY, CY, A)
```

```
      IMPLICIT NONE
C     ARGUMENT DECLARATIONS ONLY
      DOUBLE PRECISION L(3)
      INTEGER II
      DOUBLE PRECISION SUMYX, SUMYY, SUMYZ, FY, A
C     REMAINING DECLARATIONS
      INTEGER H
      DOUBLE PRECISION CY(II)
      DOUBLE PRECISION S2, GAMMA, DELTA, ATANGAM1, ATANDEL1,
      DOUBLE PRECISION SUBQUOTJ22,DS2WRTL1, ATANGAM2, ATANDEL2
      DOUBLE PRECISION DS2WRTL2,ATANGAM3, ATANDEL3, DS2WRTL3

C     FIRST CALCULATE THE BOND GREEN FUNCTION FOR THE Y DIRECTION:
C     S2
C     S2 TAKES THE FORM:
      GAMMA= (A**0.5)/L(2)
      DELTA= L(2)/(A**0.5)
      S2=L(2)*((ATAN(GAMMA))/(ATAN(DELTA)))

C     NOW COMPUTE THE FIRST ELEMENT OF THE SECOND ROW, SUMYX. AS
C     BEFORE, WE PROCEED BY COMPUTING THE DERIVATIVE OF ARCTANGAMMA
C     WRT L(1). DENOTE BY ATANGAM1
      ATANGAM1=(1.0/(1.0+GAMMA**2.0))*((L(3)+L(2))/(L(2)*2.0*A**0.5)+)

C     NOW REQUIRE THE DERIVATIVE OF ARCTANBETA WRT L(1). DENOTE BY
C     TANBED1
      ATANDEL1=(1.0/(1.0+DELTA**2.0))*(L(2)*(L(2)+L(3)))/(2.0*A**1.5+)

C     THESE TWO DERIVATIVES  AGAIN FORM A 'SUBQUOTIENT' WHICH IS THE
C     DERIVATIVE OF ARCTANALPHA/ARCTANBETA WRT L(2). UNLIKE THE
C     DIAGONAL ELEMENTS OF THE JACOBIAN, THE OFF-DIAGONAL ELEMENTS
C     HAVE A SLIGHTLY SIMPLER FORM FOR THE DERIVATIVES OF THE BOND
C     GREEN FUNCTIONS, SO WE CAN WRITE DIRECTLY THE DERIVATIVE OF S2
C     WRT L(1) AS DS2WRTL1
      DS2WRTL1=L(2)*((ATAN(DELTA)*ATANGAM1 -ATAN(GAMMA)*ATANDEL1)
     +/((ATAN(DELTA))**2.0))

C     WITH DS2WRTL1, WE CAN FORM A MAIN QUOTIENT AND SUM INSIDE LOOP
C     20; THIS IS SUMYX
C     ************************************************************
C     WE NOW REQUIRE THE SECOND ELEMENT OF THE SECOND ROW IN THE
C     JACOBIAN WHICH WE DENOTE AS SUMYX. AGAIN, THIS IS A DIAGONAL
C     ELEMENT AND REQUIRES A FEW MORE STEPS AS DID SUMXX. SO
C     FOLLOWING THE PROCEDURE FOR SUMXX: WE COMMENCE AS WITH THE
C     FIRST ELEMENT OF THE JACOBIAN. DENOTING THE FINAL SUM AS SUMYY

C     FIRST NEED THE DERIVATIVE OF ARCTANGAMMA WRT L(2). DENOTE BY
C     ATANGAM2
      ATANGAM2=(1.0/(1.0+GAMMA**2.0))*((L(1)+L(3)-2.0*A)
     +/(L(2)*2.0*A**0.5))

C     NOW REQUIRE THE DERIVATIVE OF ARCTANDELTA WRT L(2). DENOTE BY
C     TANDEL2
      ATANDEL2=(1.0/(1.0+DELTA**2.0))*((2.0*A-L(2)*(L(1)+L(3)))
     +/(2*A**1.5))

C     THESE TWO DERIVATIVES FORM THE 'SUBQUOTIENT' WHICH IS THE
C     DERIVATIVE OF ARCTANALPHA/ARCTANBETA WRT L(2). DENOTE AS
C     SUBQUOTJ22
```

```
      SUBQUOTJ22=((ATAN(DELTA)*ATANGAM2 -ATAN(GAMMA)*ATANDEL2)
     +/((ATAN(DELTA))**2.0))

C     SUBQUOTJ22 FORMS THE DERIVATIVE OF S2 WHICH FORMS PART OF THE
C     MAIN QUOTIENT.
C     LET US DENOTE THE DERIVATIVE OF S2 WRT L(2) AS  DS2WRTL2, WHICH
C     FOLLOWS THE PRODUCT RULE
      DS2WRTL2= L(2)*SUBQUOTJ22+((ATAN(GAMMA))/(ATAN(DELTA)))

C     WE NOW TAKE THESE COMPONENTS AN FORM THE MAIN QUOTIENT, SUMXX
C     INSIDE LOOP 20
C     ************************************************************
C     FINALLY, WE COMPUTE THE THIRD ELEMENT OF THE SECOND ROW,
C     SUMYZ. AS BEFORE, WE PROCEED BY COMPUTING THE DERIVATIVE OF
C     ARCTANGAMMA WRT L(3). DENOTE BY ATANGAM3:

      ATANGAM3=(1.0/(1.0+GAMMA**2.0))*((L(1)+L(2))/(L(2)*2.0*A**0.5))

C     SIMILARLY, THE DERIVATIVE OF ARCTANDELTA WRT L(3) IS REQUIRED.
C     DENOTE AS ATANDEL3

      ATANDEL3=(1.0/(1.0+DELTA**2.0))*(L(2)*(L(1)+L(2)))/(2.0*A**1.5)

C     AND SO NOW FORM THE DERIVATIVE OF S2 WRT L(3). DENOTE AS
C     DS2WRTL3

      DS2WRTL3=L(2)*((ATAN(DELTA)*ATANGAM3 -ATAN(GAMMA)*ATANDEL3)
     +/((ATAN(DELTA))**2.0))

C     WITH DS2WRTL3, WE CAN FORM A MAIN QUOTIENT AND SUM INSIDE LOOP
C     20; THIS IS SUMYZ

C     AND THAT CONCLUDES THE CALCULATION OF THE DERIVATIVES THAT
C     FORM THE ELEMENTS OF THE SECOND ROW OF THE JACOBIAN, BUT WE
C     ALSO REQUIRE THE PARENT FUNCTION FY AS WELL!!
C     USING THE FORMULA FOR S2 WE FORM THE SUM FY INSIDE LOOP 20
C     ************************************************************
C     WITH S2 NOW CONSTRUCT THE SUM FOR FX

C     INITALISE THE FOUR SUMMATIONS
      FY=0.0
      SUMYX = 0.0
      SUMYY = 0.0
      SUMYZ = 0.0
      DO 20 H=1, II
C     WITH S2 NOW CONSTRUCT THE SUM FOR FX
        FY = FY +((L(2)-CY(H))/(CY(H)+S2))
        SUMYX=SUMYX+(-(L(2)-CY(H))*DS2WRTL1)/((CY(H)+S2)**2.0)
        SUMYY=SUMYY+((CY(H)+S2)(L(2)CY(H))*DS2WRTL2)/((CY(H)+S2)**2.0)
        SUMYZ=SUMYZ+(-(L(2)-CY(H))*DS2WRTL3)/((CY(H)+S2)**2.0)
20    CONTINUE
      RETURN

      END
C     ************************************************************
C     ************************************************************
      SUBROUTINE THIRDROW(L, JJ, SUMZX, SUMZY, SUMZZ, FZ, CZ, A)

      IMPLICIT NONE
```

```
C     ARGUMENT DECLARATIONS ONLY
      DOUBLE PRECISION L(3)
      INTEGER JJ
      DOUBLE PRECISION SUMZX, SUMZY, SUMZZ, FZ, A
C     REMAINING DECLARATIONS
      INTEGER H
      DOUBLE PRECISION CZ(JJ)
      DOUBLE PRECISION S3, EPSILON, ZETA, ATANEPS1, ATANZET1,
      DOUBLE PRECISION SUBQUOTJ33, DS3WRTL1, ATANEPS2, ATANZET2
      DOUBLE PRECISION DS3WRTL2, ATANEPS3, ATANZET3, DS3WRTL3

C     FIRST CALCULATE THE BOND GREEN FUNCTION FOR THE Z DIRECTION:
C     S3
C     S3 TAKES THE FORM:
      EPSILON= (A**0.5)/L(3)
      ZETA= L(3)/(A**0.5)
      S3=L(3)*((ATAN(EPSILON))/(ATAN(ZETA)))

C     NOW COMPUTE THE FIRST ELEMENT OF THE THIRD ROW, SUMZX. AS BEFORE,
C     WE PROCEED BY COMPUTING THE DERIVATIVE OF ARCTANEPSILON WRT L(1).
C     DENOTE BY ATANEPS1
      ATANEPS1=(1.0/(1.0+EPSILON**2.0))*((L(3)+L(2))/(L(3)*2.0*A**0.
     +5))

C     NOW REQUIRE THE DERIVATIVE OF ARCTANZETA WRT L(1). DENOTE BY
C     ATANZET1
      ATANZET1=(1.0/(1.0+ZETA**2.0))*(L(3)*(L(2)+L(3)))/(2.0*A**1.5)

C     THESE TWO DERIVATIVES  AGAIN FORM A 'SUBQUOTIENT' WHICH IS THE
C     DERIVATIVE OF ARCTANEPSILON/ARCTANZETA WRT L(1). UNLIKE THE
C     DIAGONAL ELEMENTS OF THE JACOBIAN, THE OFF-DIAGONAL ELEMENTS
C     HAVE A SLIGHTLY SIMPLER FORM FOR THE DERIVATIVES OF THE BOND
C     GREEN FUNCTIONS, SO WE CAN WRITE DIRECTLY THE DERIVATIVE OF S3
C     WRT L(1) AS DS3WRTL1
      DS3WRTL1=L(3)*((ATAN(ZETA)*ATANEPS1 -ATAN(EPSILON)*ATANZET1)
     +/((ATAN(ZETA))**2.0))

C     WITH DS2WRTL1, WE CAN FORM A MAIN QUOTIENT AND SUM INSIDE LOOP
C     20; THIS IS SUMZX
C     ************************************************************
C     NOW COMPUTE THE SECOND ELEMENT OF THE THIRD ROW, SUMZY. AS
C     BEFORE, WE PROCEED BY COMPUTING THE DERIVATIVE OF ARCTANEPSILON
C     WRTL(2). DENOTE BY ATANEPS2:
      ATANEPS2=(1.0/(1.0+EPSILON**2.0))*((L(1)+L(3))/(L(3)*2.0*A**0.5))

C     ... AND ALSO THE DERIVATIVE OF ARCTANZETA WRT L(2), DENOTE AS
C     TANZET2:
      ATANZET2=(1.0/(1.0+ZETA**2.0))*(-L(3)*(L(1)+L(3)))/(2.0*A**1.5)

C     THESE TWO DERIVATIVES  AGAIN FORM A 'SUBQUOTIENT' WHICH IS THE
C     DERIVATIVE OF ARCTANEPSILON/ARCTANZETA WRT L(2). UNLIKE THE
C     DIAGONAL ELEMENTS OF THE JACOBIAN, THE OFF-DIAGONAL ELEMENTS
C     HAVE A SLIGHTLY SIMPLER FORM FOR THE C    DERIVATIVES OF THE
C     BOND GREEN FUNCTIONS, SO WE CAN WRITE DIRECTLY THE DERIVATIVE
C     OF S3 WRT L(2)AS DS3WRTL2
      DS3WRTL2=L(3)*((ATAN(ZETA)*ATANEPS2 -ATAN(EPSILON)*ATANZET2)
     +/((ATAN(ZETA))**2.0))

C     WITH DS3WRTL2, WE CAN FORM A MAIN QUOTIENT AND SUM INSIDE LOOP
```

```
C      20; THIS IS SUMZY
C      ************************************************************
C      FINALLY, WE COMPUTE THE THIRD ELEMENT OF THE SECOND ROW ROW,
C      SUMZZ. AS BEFORE, WE PROCEED BY COMPUTING THE DERIVATIVE OF
C      ARCTANEPSILON WRT L(3). DENOTE BY ATANEPS3:
       ATANEPS3=(1.0/(1.0+EPSILON**2.0))*((L(1)+L(2)-2.0*A)
      +/(L(3)*2.0*A**0.5))

C      NOW REQUIRE THE DERIVATIVE OF ARCTANZETA WRT L(3). DENOTE BY
C      TANZET3

       ATANZET3=(1.0/(1.0+ZETA**2.0))*((2.0*A-L(3)*(L(1)+L(2)))
      +/(2*A**1.5))

C      THESE TWO DERIVATIVES FORM THE 'SUBQUOTIENT' WHICH IS THE
C      DERIVATIVE OF ARCEPSILON/ARCTANZETA WRT L(3). DENOTE AS
C      SUBQUOTJ33
       SUBQUOTJ33=((ATAN(ZETA)*ATANEPS3 -ATAN(EPSILON)*ATANZET3)
      +/((ATAN(ZETA))**2.0))

C      SUBQUOTJ33 FORMS THE DERIVATIVE OF S3 WHICH FORMS PART OF THE
C      MAIN QUOTIENT. LET US DENOTE THE DERIVATIVE OF S3 WRT L(3) AS
C      DS3WRTL3, WHICH FOLLOWS THE PRODUCT RULE

       DS3WRTL3= L(3)*SUBQUOTJ33+((ATAN(EPSILON))/(ATAN(ZETA)))

C      WE NOW TAKE THESE COMPONENTS AN FORM THE MAIN QUOTIENT, SUMZZ
C      INSIDE LOOP 20

C      AND THAT CONCLUDES THE CALCULATION OF THE DERIVATIVES THAT
C      FORM THE ELEMENTS OF THE THIRD ROW OF THE JACOBIAN, BUT WE
C      ALSO REQUIRE THE PARENT FUNCTION FZ AS WELL!!
C      USING THE FORMULA FOR S3 WE FORM THE SUM FZ INSIDE LOOP 20
C      ************************************************************
C      INITALISE THE FOUR SUMMATIONS
       FZ=0.0
       SUMZX = 0.0
       SUMZY = 0.0
       SUMZZ = 0.0
       DO 20 H=1, JJ
C      WITH S3 NOW CONSTRUCT THE SUM FOR FY
       FZ = FZ +((L(3)-CZ(H))/(CZ(H)+S3))
       SUMZX=SUMZX+(-(L(3)-CZ(H))*DS3WRTL1)/((CZ(H)+S3)**2.0)
       SUMZY=SUMZY+(-(L(3)-CZ(H))*DS3WRTL2)/((CZ(H)+S3)**2.0)
       SUMZZ=SUMZZ+((CZ(H)+S3)-(L(3)-CZ(H))*DS3WRTL3)/((CZ(H)+S3)**2.0)
20     CONTINUE
       RETURN

       END
```

D Program for Increasing the Size of Inputfiles for the NETSIM programs

```
      PROGRAM EXPAND

C     PROGRAM TO EXPAND DATA

      IMPLICIT NONE
      INTEGER I, K, J, L
      REAL CX(1000000)

C     SPECIFY NUMBER OF PORES

      L= 3495

C     SPECIFY LAMBDA FACTOR

      K= 24

      OPEN(UNIT=8, FILE='1XEXPANDED.txt', STATUS='NEW')
      DO 10 J=1, K
            OPEN(UNIT=6, FILE='RANDOMISED.txt', STATUS='OLD')
            REWIND(6)
            DO 20 I=1, L
                  READ (6,*) CX(I)
                  WRITE(8,*) CX(I)
20          CONTINUE
10    CONTINUE

      END
```

E Program for Random Pore Selection

```
      PROGRAM PORESELECTION

C     RANDOMISES A SET OF NUMBERS UNIFORMLY FROM AN INPUT FILE
C     WITHOUT SELECTING THE SAME NUMBER MORE THAN ONCE

C     USES THE MODULE RANVAL FROM THE DIGITAL VISUAL FORTRAN Va
C     LIBRARY

      IMPLICIT NONE
      REAL RANVAL, RAA(1000000), CX(1000000), GX(1000000)
      INTEGER I, J
      INTEGER K, IRAND
      CHARACTER *16 FILENAME

C     SPECIFY NUMBER OF PORES TO BE RANDOMISED
C     ENTER INITIAL NUMBER OF PORES
      K=3495
C     OR, ENTER INITIAL NUMBER OF PORE EXPANDED BY 'LAMBDA FACTOR'
C     K=3495*24

      FILENAME= '1XRAND19.txt'
C     OPEN EXTERNAL DATAFILE
      OPEN(UNIT = 5, FILE=FILENAME, STATUS='OLD')
      REWIND(5)
C     PREPARE OUTFILE
      OPEN(UNIT =6, FILE='1XRAND20.txt', STATUS='NEW')
      REWIND(6)
C     READ IN THE CONDUCTIVITIES, CX
      DO 100 I=1, K
        READ(5,*) CX(I)
100   CONTINUE
C     INITIALISE LOOP FOR RANDOMISING INPUT CONDUCTANCES
      I=0
1000  CONTINUE

C     THIS BLOCK PREVENTS THE SAME CONDUCTANCE BEEN SELECTED MORE
C     THAN ONCE
      IF (I .LT. K) THEN
      I=I+1
      CALL RANDOM(RANVAL)
      RAA(I)=RANVAL
      IRAND=(INT(K*RAA(I)))
      IF (CX(IRAND) .GT. 0.0) THEN
            GX(I)=CX(IRAND)
            CX(IRAND)=-1.0
      WRITE(6, *) GX(I)
      ELSE
      I = I-1
      END IF
      END IF
        IF (I .EQ. K) THEN
            GOTO 2000
        END IF
      GO TO 1000
2000  CONTINUE

      END
```

F Program for the Random Generation of Lognormal Deviates

```
      PROGRAM LOGNORMAL DEVIATES

C     GENERATES A LIST OF RANDOM NUMBERS FROM A LOGNORMAL
C     DISTRIBUTION THAT IS DERIVED FROM EXPONENTIATION OF A NORMAL
C     DISTRIBUTION. ADJUSTABLE MEAN AND STANDARD DEVIATION CAN BE
C     INPUT OR SET TO ZERO AND 1.0 RESPECTIVELY

C     THE CODE USES THE FUNCTION SUBMODULES GASDEV(IDUM) WITH
C     RAN1(IDUM) AS FOUND IN NUMERICAL RECIPES, W. H. PRESS ET AL.
C     2ND EDITON 1992, pp. 280

C     THE STANDARD DEVIATION AND MEAN OF THE LOGNORMAL DISTRIBUTION
C     ARE NOT CALCULATED IN THIS PROGRAM; THESE VALUES ARE OBTAINED
C     BY EXPORTING THE OUTPUT DEVIATES TO AN *.XLS FILE AND APPLYING
C     TILL'S EQUATIONS (1974).

      IMPLICIT NONE

      REAL GASDEV,Y, Z, LNZ
      INTEGER J, IDUM, COUNT
      REAL MEAN, SD, DENOM
      PARAMETER (MEAN= 1.0, SD= 3.0)
      PARAMETER(COUNT=10000)
      DENOM=REAL(COUNT)

C     WRITE LOGNORMAL DEVIATES TO AN OUTPUT FILE
      OPEN(UNIT=6, FILE='NORMDIST SD= 3.0.txt', STATUS='NEW')
      REWIND(6)
      SUM=0.0
      DO 10 J=1, COUNT
            Y=GASDEV(IDUM)
            Z= MEAN + SD*Y
            LNZ=EXP(Z)
            WRITE(6,*), Z
10    CONTINUE

      END
C     ****************************************************************
C                                END OF MAIN PROGRAM
C     ****************************************************************
      FUNCTION GASDEV(IDUM)
C     RETURNS A NORMALLY DISTRIBUTED DEVIATE WITH ZERO MEAN AND UNIT
C     VARIANCE,USING RAN1(IDUM) AS THE SOURCE OF UNIFORM DEVIATES

      INTEGER IDUM
      REAL GASDEV, RANVAL
      INTEGER ISET
      REAL FAC, GSET, RSQ, V1, V2

      SAVE ISET, GSET
      DATA ISET/0/
1     CONTINUE
      IF(ISET .EQ. 0) THEN
      V1=2.*RAN1(IDUM)-1.
      V2=2.*RAN1(IDUM)-1.
      RSQ=V1**2+V2**2
      IF(RSQ .GE. 1. .OR. RSQ .EQ. 0)GOTO 1
```

```
      FAC=SQRT(-2.*LOG(RSQ)/RSQ)
      GSET=V1*FAC
      GASDEV=V2*FAC
      ISET=1

      ELSE
      GASDEV=GSET
      ISET=0
      ENDIF

      END

      FUNCTION RAN1(IDUM)

      INTEGER IDUM, IA, IM, IQ, IR, NTAB,NDIV
      REAL RAN1, AM, EPS, RNMAX
      PARAMETER(IA=16807,IM=2147483647,AM=1./IM, IQ=127773, IR=2836,
     + NTAB=32, NDIV=1+(IM-1)/NTAB,EPS=1.2E-7, RNMX=1.-EPS)
      INTEGER J,K,IV(NTAB), IY

      SAVE IV, IY
      DATA IV /NTAB*0/, IY/0/
      IF(IDUM .LE. 0 .OR. IY .EQ. 0)THEN
      IDUM=MAX(-IDUM, 1)

      DO 10 J=NTAB+8, 1, -1
            K=IDUM/IQ
            IDUM=IA*(IDUM-K*IQ)-IR*K
            IF (IDUM .LT. 0) IDUM=IDUM+IM
            IF (J .LE. NTAB) IV(J)=IDUM
10    CONTINUE

      IY=IV(1)
      END IF
      K=IDUM/IQ
      IDUM=IA*(IDUM-K*IQ)-IR*K
      IF (IDUM .LT. 0) IDUM=IDUM+IM
      J=1+IY/NDIV
      IY=IV(J)
      IV(J)=IDUM
      RAN1=MIN(AM*IY, RNMX)
      RETURN

      END
```

G ISOTROPIC NETSIM, adapted from *Jing* (1990)

```
      PROGRAM ISONETSIM

C     THIS PROGRAM PERFORMS AN EXACT NETWORK CALCULATION FOR THE
C     CONDUCTANCE IN THREE DIMENSIONS BY SOLVING THE NETWORK PROBLEM
C     ON AN ISOTROPIC CUBIC LATTICE

C     THE ORIGINAL PROGRAM NETSIM (JING, 1990) WAS INITIALLY
C     MODIFIED ON 23rd FEBRUARY 2000 BY SOURITH SISAVATH SO THAT
C     SIMULATIONS ONLY REQUIRE THE MAIN BLOCK TO SPECIFY THE CUBIC
C     LATTICE, IMPOSE THE BOUNDARY CONDITIONS AND CALCULATE THE
C     TOTAL CONDUCTANCE AND FLOWRATE

C     THE EXISTING MODIFICATIONS ARE THAT A LIST OF CONDUCTANCES MAY
C     BE READ FROM AN EXTERNAL INPUT FILE THAT DECORATE THE NETWORK
C     IN EACH OF THE LATTICE DIRECTIONS. ALSO, AN EFFECTIVE CONDUCTANCE
C     IS CALCULATED BY DIVIDING THE TOTAL CONDUCTANCE BY THE NUMBER OF
C     NODES IN THE NETWORK (DAVID ET AL., 1990)

      IMPLICIT NONE
      INTEGER I,J,K,NUM,MARK,NX,NY,NZ,N2,NMAX
      PARAMETER (NMAX=32770,N2=100)
C     INTRODUCED FOR SOLVING USING OVER-RELAXATION TECHNIQUE
      REAL HCONDU(N2,N2,N2),TOTALQ,POTEN(N2,N2,N2),UP2,DOWN2,XPOTEN
      REAL COMPARE,RATE,PERM,ERR1,OUTCON, G1, GEFF

C     SPECIFY TOLERANCE FOR OVERRELAXATION CALCULATION
      ERR1=0.00001

C     SPECIFY LATTICE SIZE BY SPECIFYING THE NUMBER OF INTERNAL
C     NODES
      NX=30
      NY=NX
      NZ=NX

C     SPECIFY A CUBIC NETWORK AND DECORATE WITH CONDUCTANCES FROM A
C     SINGLE INPUT FILE

      OPEN (UNIT=18, FILE='1YRAND20.txt', STATUS='OLD')
      REWIND(18)
      DO 1114 K = 1, 2 * NZ + 1, 2
        DO 1114 I = 2, 2 * NX, 2
           DO 1114 J = 2, 2 * NY, 2
           READ(18,*)     HCONDU(I,J,K)
1114  CONTINUE

      DO 1115 I = 1, 2 * NX + 1, 2
        DO 1115 J = 2, 2 * NY, 2
          DO 1115 K=2,2*NZ,2
          READ(18, *)     HCONDU(I,J,K)
1115  CONTINUE

      DO 1116 J = 1, 2 * NY + 1, 2
        DO 1116 I = 2, 2 * NX, 2
          DO 1116 K=2,2*NZ,2
          READ(18,*)     HCONDU(I,J,K)
1116  CONTINUE
      CLOSE(18)
```

```
C     BOUNDARY CONDITIONS

150    NUM = 0
       MARK = 0
       TOTALQ    = 0.0
C     SPECIFY PRESSURE AT INFLOW SIDE (INPUT FACE)
       DO 155 J = 2, 2 * NY, 2
          DO  160 K = 2, 2 * NZ, 2
             POTEN(0,J,K) = 10.0
160          CONTINUE
155    CONTINUE
C     SPECIFY PRESSURE AT OUTFLOW SIDE (OUTPUT FACE)
       DO 170 J = 2, 2 * NY, 2
          DO 180 K = 2, 2 * NZ, 2
             POTEN(2 * NX + 2,J,K) = 0.0
180       CONTINUE
170     CONTINUE
C     SPECIFY PRESSURE DROP AT EACH NODE ALONG THE FLOW DIRECTION
       DO 188  I  =  2, 2 * NX, 2
         DO 190 J = 2, 2 * NY, 2
           DO 200 K = 2, 2 * NZ, 2
              POTEN(I,J,K) = 10.0 -(I - 1) * 10 / (2 * NX)
200          CONTINUE
190        CONTINUE
188      CONTINUE
C     SPECIFY PRESSURE AT EACH NODE PERPENDICULAR TO THE FLOW DIRECTION
245       TOTALQ = 0.0
       DO 250 I = 2, 2 * NX, 2
          DO 260 K = 2, 2 * NZ, 2
             POTEN(I,0,K) = POTEN(I,2,K)
             POTEN(I,2 * NY + 2,K) = POTEN(I,2 * NY,K)
260       CONTINUE
250    CONTINUE
       DO 270 I = 2, 2 * NX, 2
          DO 280 J = 2, 2 * NY, 2
             POTEN(I,J,0) = POTEN(I,J,2)
             POTEN(I,J,2 * NZ + 2) = POTEN(I,J,2 * NZ)
280       CONTINUE
270    CONTINUE

      PRINT *,'ITERATION=',NUM
CIC
CIC=================================================================
CIC//
CIC//              MAIN ITERATION STARTS HERE
CIC//
CIC// CALCULATION OF NEW POTENTIALS USING CONSERVATION OF MASS FOR
CIC// HYDRAULIC CONDUCTANCE, I.E., SUMMATION OF CURRENT FLOWS TO A
CIC// NODE IS ZERO
CIC//
CIC=================================================================
CIC
       NUM = NUM + 1
       DO 300 I = 2, 2 * NX, 2
          DO 310 J = 2, 2 * NY, 2
             DO 320 K = 2, 2 * NZ, 2
       UP2 = POTEN(I,J-2,K) * HCONDU(I,J-1,K)
     ++ POTEN(I-2,J,K) * HCONDU(I-1,J,K) + POTEN(I+2,J,K)
     +* HCONDU(I+1,J,K) + POTEN(I,J+2,K) * HCONDU(I,J+1,K)
```

```
     ++ POTEN(I,J,K-2) * HCONDU(I,J,K-1)
     ++ POTEN(I,J,K+2) * HCONDU(I,J,K+1)
        DOWN2 = HCONDU(I,J-1,K) +  HCONDU(I-1,J,K)
     ++ HCONDU(I+1,J,K) + HCONDU(I,J+1,K)
     ++ HCONDU(I,J,K-1) + HCONDU(I,J,K+1)
        IF (DOWN2 .GT. 0.0001) THEN
          XPOTEN = UP2 / DOWN2
          COMPARE = (XPOTEN - POTEN(I,J,K)) / XPOTEN
          IF (ABS(COMPARE) .GT. ERR1) THEN
           MARK = 1
          ENDIF
          POTEN(I,J,K) = POTEN(I,J,K) + 1.86 * (XPOTEN - POTEN(I,J,K))
        ELSE
          POTEN(I,J,K) = 0.
        ENDIF
320         CONTINUE
310       CONTINUE
300     CONTINUE
CIC-------------------------------------------------------------------
CIC// CALCULATING THE TOTAL CONDUCTANCE AND THE FLOW RATE
CIC-------------------------------------------------------------------
        DO 350 J = 2, 2 * NY, 2
           DO 400 K = 2, 2 * NZ, 2
              RATE = POTEN(2 * NX,J,K)*HCONDU(2*NX+1,J,K)
              TOTALQ = TOTALQ + RATE
400        CONTINUE
350     CONTINUE
CIC-------------------------------------------------------------------
CIC//  TESTING CONVERGENCE
CIC-------------------------------------------------------------------
        IF (MARK .EQ. 1) THEN
           MARK = 0
           GO TO 245
        ENDIF

C     PROCEDURE TO COMPUTE THE EMT PARAMETERS AS PER DAVID ET AL.,
C     (1990) TO ALLOW A DIRECT COMPARISON TO USING KIRKPATRICK'S
C     EQUATION

C     PERFORM THE CALCULATION CH= TOTALQ/GRADP, WHERE GRADP IS
C     ASSIGNED A VALUE OF 10
      OUTCON=TOTALQ/10.0

C     CALCULATE THE TOTAL CONDUCTANCE OF THE NETWORK WHEN EACH PORE
C     IS ASSIGNED A CONDUCTANCE OF 1.0
      G1=(NX**2.0)/(NX+1.0)

C     CALCULATE AN EFFECTIVE CONDUCTANCE BY DIVIDING THE TOTAL
C     CONDUCTANCE BY G[1] (DAVID ET AL., 1990)
      GEFF=OUTCON/G1

      PRINT*, 'OUTCON', OUTCON, 'IN UNITS OF INPUT CONDUCTANCES'
      PRINT*, 'G1', G1
      PRINT*, 'NUMBER OF NODES IN 1D:', NX
      PRINT*, 'GEFF', GEFF

      END
```

H ANISOTROPIC NETSIM, adapted from *Jing* (1990)

```
      PROGRAM ANISONETSIM

C     THIS PROGRAM PERFORMS AN EXACT NETWORK CALCULATION FOR THE
C     CONDUCTANCE IN THREE DIMENSIONS BY SOLVING THE NETWORK PROBLEM
C     ON AN ANISOTROPIC CUBIC LATTICE

C     THE ORIGINAL PROGRAM NETSIM (JING, 1990) WAS INITIALLY
C     MODIFIED ON 23rd FEBRUARY 2000 BY SOURITH SISAVATH SO THAT
C     SIMULATIONS ONLY REQUIRE THE MAIN BLOCK TO SPECIFY THE CUBIC
C     LATTICE, IMPOSE THE BOUNDARY CONDITIONS AND CALCULATE THE TOTAL
C     CONDUCTANCE AND FLOWRATE

C     AS WITH ISONETSIM AN EFFECTIVE CONDUCTANCE IS CALCULATED BY
C     DIVIDING THE TOTAL CONDUCTANCE BY THE NUMBER OF NODES IN THE
C     NETWORK (DAVID ET AL., 1990)

C     THE MAIN FEATURE THAT DISTINGUISHES THIS PROGRAM FROM
C     ISONETSIM IS THAT THREE SETS OF EXTERNAL CONDUCTANCES ARE USED
C     AS INPUT, EACH DECORATING THE LATTICE IN ONE SPECIFIC DIRECTION
C     ONLY; THIS ALLOWS FLOW SIMULATIONS TO BE PERFORMED ON AN
C     ANISOTROPIC CUBIC LATTICE

C     PERMUTING THE ORDER IN WHICH THE THREE EXTERNAL SETS OF DATA
C     ARE FED INTO THE LATTICE ALLOWS THE INTERCHANGE OF THE FLOW
C     DIRECTIONS SO THAT THE POTENTIAL CAN BE APPLIED CONSECUTIVELY
C     ALONG EACH LATTICE DIRECTION

      IMPLICIT NONE
      INTEGER I,J,K,NUM,MARK,NX,NY,NZ,N2, NMAX
      PARAMETER (NMAX=32770,N2=100)
C     INTRODUCED FOR SOLVING USING OVER-RELAXATION TECHNIQUE
      REAL HCONDU(N2,N2,N2),TOTALQ,POTEN(N2,N2,N2),UP2,DOWN2,XPOTEN
      REAL COMPARE,RATE,PERM,ERR1,OUTCON, G1, GEFF

C     SPECIFY TOLERANCE FOR OVERRELAXATION CALCULATION
      ERR1=0.00001

C     SPECIFY LATTICE SIZE BY SPECIFYING THE NUMBER OF INTERNAL
C     NODES
      NX=30
      NY=NX
      NZ=NX

C     SPECIFY A CUBIC NETWORK AND DECORATE WITH CONDUCTANCES FROM
C     THREE SEPARATE INPUT FILES

      OPEN (UNIT=18, FILE='3XRAND20.txt', STATUS='OLD')
      REWIND(18)
      DO 1114 K = 1, 2 * NZ + 1, 2
        DO 1114 I = 2, 2 * NX, 2
           DO 1114 J = 2, 2 * NY, 2
      READ(18,*)    HCONDU(I,J,K)
1114  CONTINUE

      OPEN (UNIT=19, FILE='3YRAND20.txt', STATUS='OLD')
      REWIND(19)
      DO 1115 I = 1, 2 * NX + 1, 2
```

```
        DO 1115 J = 2, 2 * NY, 2
          DO 1115 K=2,2*NZ,2
      READ(19, *)     HCONDU(I,J,K)
1115  CONTINUE

      OPEN (UNIT=20, FILE='1YRAND20.txt', STATUS='OLD')
      REWIND(20)
      DO 1116 J = 1, 2 * NY + 1, 2
        DO 1116 I = 2, 2 * NX, 2
          DO 1116 K=2,2*NZ,2
      READ(20,*)     HCONDU(I,J,K)
1116  CONTINUE
      CLOSE(18)
      CLOSE(19)
      CLOSE(20)

C     BOUNDARY CONDITIONS

150    NUM = 0
        MARK = 0
        TOTALQ     = 0.0
C     SPECIFY PRESSURE AT INFLOW SIDE (INPUT FACE)
        DO 155 J = 2, 2 * NY, 2
           DO  160 K = 2, 2 * NZ, 2
              POTEN(0,J,K) = 10.0
161          CONTINUE
156    CONTINUE
C     SPECIFY PRESSURE AT OUTFLOW SIDE (OUTPUT FACE)
      DO 170 J = 2, 2 * NY, 2
           DO 180 K = 2, 2 * NZ, 2
              POTEN(2 * NX + 2,J,K) = 0.0
181        CONTINUE
171      CONTINUE
C     SPECIFY PRESSURE DROP AT EACH NODE ALONG THE FLOW DIRECTION
        DO 188  I  =  2, 2 * NX, 2
          DO 190 J = 2, 2 * NY, 2
            DO 200 K = 2, 2 * NZ, 2
               POTEN(I,J,K) = 10.0 -(I - 1) * 10 / (2 * NX)
201          CONTINUE
191         CONTINUE
188       CONTINUE
C     SPECIFY PRESSURE AT EACH NODE PERPENDICULAR TO THE FLOW DIRECTION
246       TOTALQ = 0.0
        DO 250 I = 2, 2 * NX, 2
           DO 260 K = 2, 2 * NZ, 2
              POTEN(I,0,K) = POTEN(I,2,K)
              POTEN(I,2 * NY + 2,K) = POTEN(I,2 * NY,K)
260          CONTINUE
251       CONTINUE
        DO 270 I = 2, 2 * NX, 2
           DO 280 J = 2, 2 * NY, 2
              POTEN(I,J,0) = POTEN(I,J,2)
              POTEN(I,J,2 * NZ + 2) = POTEN(I,J,2 * NZ)
280          CONTINUE
271       CONTINUE

      PRINT *,'ITERATION=',NUM

CIC
```

```
CIC=================================================================
CIC//              MAIN ITERATION STARTS HERE
CIC//
CIC// CALCULATION OF NEW POTENTIALS USING CONSERVATION OF MASS FOR
CIC// HYDRAULIC CONDUCTANCE, I.E., SUMMATION OF CURRENT FLOWS TO A
CIC// NODE IS ZERO
CIC//
CIC=================================================================
CIC
        NUM = NUM + 1
        DO 300 I = 2, 2 * NX, 2
           DO 310 J = 2, 2 * NY, 2
              DO 320 K = 2, 2 * NZ, 2
        UP2 = POTEN(I,J-2,K) * HCONDU(I,J-1,K)
     ++ POTEN(I-2,J,K) * HCONDU(I-1,J,K) + POTEN(I+2,J,K)
     +* HCONDU(I+1,J,K) + POTEN(I,J+2,K) * HCONDU(I,J+1,K)
     ++ POTEN(I,J,K-2) * HCONDU(I,J,K-1)
     ++ POTEN(I,J,K+2) * HCONDU(I,J,K+1)
        DOWN2 = HCONDU(I,J-1,K) +  HCONDU(I-1,J,K)
     ++ HCONDU(I+1,J,K) + HCONDU(I,J+1,K)
     ++ HCONDU(I,J,K-1) + HCONDU(I,J,K+1)
        IF (DOWN2 .GT. 0.0001) THEN
          XPOTEN = UP2 / DOWN2
          COMPARE = (XPOTEN - POTEN(I,J,K)) / XPOTEN
          IF (ABS(COMPARE) .GT. ERR1) THEN
           MARK = 1
          ENDIF
          POTEN(I,J,K) = POTEN(I,J,K) + 1.86 * (XPOTEN - POTEN(I,J,K))
        ELSE
          POTEN(I,J,K) = 0.
        ENDIF
320          CONTINUE
310        CONTINUE
300     CONTINUE
CIC
CIC-----------------------------------------------------------------
CIC// CALCULATING THE TOTAL CONDUCTANCE AND THE FLOW RATE
CIC-----------------------------------------------------------------
CIC
        DO 350 J = 2, 2 * NY, 2
           DO 400 K = 2, 2 * NZ, 2
              RATE = POTEN(2 * NX,J,K)*HCONDU(2*NX+1,J,K)
              TOTALQ = TOTALQ + RATE
400        CONTINUE
350     CONTINUE
CIC-----------------------------------------------------------------
CIC//  TESTING CONVERGENCE
CIC-----------------------------------------------------------------
        IF (MARK .EQ. 1) THEN
           MARK = 0
           GO TO 245
        ENDIF

C     PROCEDURE TO COMPUTE THE EMT PARAMETERS AS PER DAVID ET AL.,
C     (1990) TO ALLOW A DIRECT COMPARISON TO USING KIRKPATRICK'S
C     EQUATION

C     PERFORM THE CALCULATION CH= TOTALQ/GRADP, WHERE GRADP IS
C     ASSIGNED A VALUE OF 10
```

```
      OUTCON=TOTALQ/10.0

C     CALCULATE THE TOTAL CONDUCTANCE OF THE NETWORK WHEN EACH PORE
C     IS ASSIGNED A CONDUCTANCE OF 1.0
      G1=(NX**2.0)/(NX+1.0)

C     CALCULATE AN EFFECTIVE CONDUCTANCE BY DIVIDING THE TOTAL
C     CONDUCTANCE BY G[1] (DAVID ET AL., 1990)
      GEFF=OUTCON/G1

      PRINT*, 'OUTCON', OUTCON, 'IN UNITS OF INPUT CONDUCTANCES'
      PRINT*, 'G1', G1
      PRINT*, 'NUMBER OF NODES IN 1D:', NX
      PRINT*, 'GEFF', GEFF

      END
```